

University of Groningen

Nanomaterials-Based Bioinspired Next Generation Wearable Sensors: A State-of-the-Art Review

Sengupta, Debarun; Kottapalli, Ajay Giri Prakash

Published in:
Advanced electronic materials

DOI:
[10.1002/aelm.202300436](https://doi.org/10.1002/aelm.202300436)

IMPORTANT NOTE: You are advised to consult the publisher's version (publisher's PDF) if you wish to cite from it. Please check the document version below.

Document Version
Publisher's PDF, also known as Version of record

Publication date:
2024

[Link to publication in University of Groningen/UMCG research database](#)

Citation for published version (APA):

Sengupta, D., & Kottapalli, A. G. P. (2024). Nanomaterials-Based Bioinspired Next Generation Wearable Sensors: A State-of-the-Art Review. *Advanced electronic materials*, 10(1), Article 2300436. <https://doi.org/10.1002/aelm.202300436>

Copyright

Other than for strictly personal use, it is not permitted to download or to forward/distribute the text or part of it without the consent of the author(s) and/or copyright holder(s), unless the work is under an open content license (like Creative Commons).

The publication may also be distributed here under the terms of Article 25fa of the Dutch Copyright Act, indicated by the "Taverne" license. More information can be found on the University of Groningen website: <https://www.rug.nl/library/open-access/self-archiving-pure/taverne-amendment>.

Take-down policy

If you believe that this document breaches copyright please contact us providing details, and we will remove access to the work immediately and investigate your claim.

Downloaded from the University of Groningen/UMCG research database (Pure): <http://www.rug.nl/research/portal>. For technical reasons the number of authors shown on this cover page is limited to 10 maximum.

Nanomaterials-Based Bioinspired Next Generation Wearable Sensors: A State-of-the-Art Review

Debarun Sengupta and Ajay Giri Prakash Kottapalli*

With a constantly growing percentage of the population having access to high-quality healthcare facilities, preventable pathogenic illnesses have been nearly eradicated in the developed parts of the world, which has led to a significant rise in the average human life expectancy over the last few decades. In such a highly developed world, age-related illnesses will lead to an immense burden on healthcare providers. Remote health monitoring enabled by wearable sensors will play a significant role in the growth and evolution of Health 3.0 by providing intimate and valuable information to healthcare providers regarding the progression of disease in patients with critical life-altering conditions. Especially, in the case of people suffering from neurodegenerative disorders, inexpensive and user-friendly wearable sensors can enable physiotherapists monitor real-time physiological parameters to design patient-specific treatment plans. This review provides a comprehensive overview of the recent advances and emerging trends at the convergence of biomimicry and nanomaterial sensors, with a specific focus on wearable skin-inspired mechanical sensors for applications in IoT-enabled human physiological parameters monitoring. Skin-inspired wearable mechanical sensors with relevance to the most common types of sensing mechanisms including piezoresistive, piezocapacitive, and triboelectric sensing are discussed along with their current challenges and possible future opportunities.

derive inspiration from the morphology, sensing mechanisms, and functionality of natural sensors have been gaining popularity in modern research for the past few decades. For any micro/nanoelectromechanical systems (MEMS/NEMS) development, efficient design is the key to enhancing the performance of the device. For example, while designing a flow sensor, a key concern is to have a design that enables a high dynamic range without compromising on the signal-to-noise ratio. There are many other examples of sensors and sensing systems that we already use in daily life, such as accelerometers, gyroscopes, strain and pressure sensors, etc. where design might be of utmost importance. Living creatures have evolved over the ages through the process of natural selection to adapt to their surrounding environment. Taking inspiration from living beings to solve engineering problems is often the best design approach as it saves a substantial amount of time in design optimization. In the last two decades a significant amount of research effort has been dedicated towards

1. Introduction

Biomimetic and nature-inspired design philosophies for the creation of state-of-the-art sensors and sensing systems that


developing high-performance bioinspired nanoengineered structures and materials for next-generation sensors, devices, and smart wearables (Figure 1).^[1–7]

The sensory perceptions in living creatures have evolved over millions of years to carry out some of the most complex sensing tasks like vision, auditory, touch, olfactory, and gustatory perception. Among all the sensing abilities, although hearing seems to be a simple sensing task that mammals perform involuntarily, the inner ear's mechanism of sensing sound is an example of a highly sophisticated sensor developed to achieve the best acoustic sensing performance. The inner ear consists of various sensors such as acoustic sensors, linear acceleration sensors, gyroscopes, tactile sensors, and flow sensors. Despite the high diversity of the parameters that are sensed, the fundamental sensing elements in all these sensors are mechanosensory hair cells. Mechanosensory hair cells are not limited to humans. For instance, fish have an array of hair-like structures on their lateral line systems, which enable them to sense flow and current.

There is a myriad of impressive and interesting sensory organs found in various creatures that can potentially inspire

D. Sengupta, A. G. P. Kottapalli
Department of Bioinspired MEMS and Biomedical Devices
Engineering and Technology Institute Groningen (ENTEG)
University of Groningen
Groningen 9747 AG, The Netherlands
E-mail: a.g.p.kottapalli@rug.nl

A. G. P. Kottapalli
MIT Sea Grant College program
Massachusetts Institute of Technology (MIT)
77 Massachusetts Avenue, NW98-151, Cambridge 02139, USA

 The ORCID identification number(s) for the author(s) of this article can be found under <https://doi.org/10.1002/aelm.202300436>

© 2023 The Authors. Advanced Electronic Materials published by Wiley-VCH GmbH. This is an open access article under the terms of the Creative Commons Attribution License, which permits use, distribution and reproduction in any medium, provided the original work is properly cited.

DOI: 10.1002/aelm.202300436

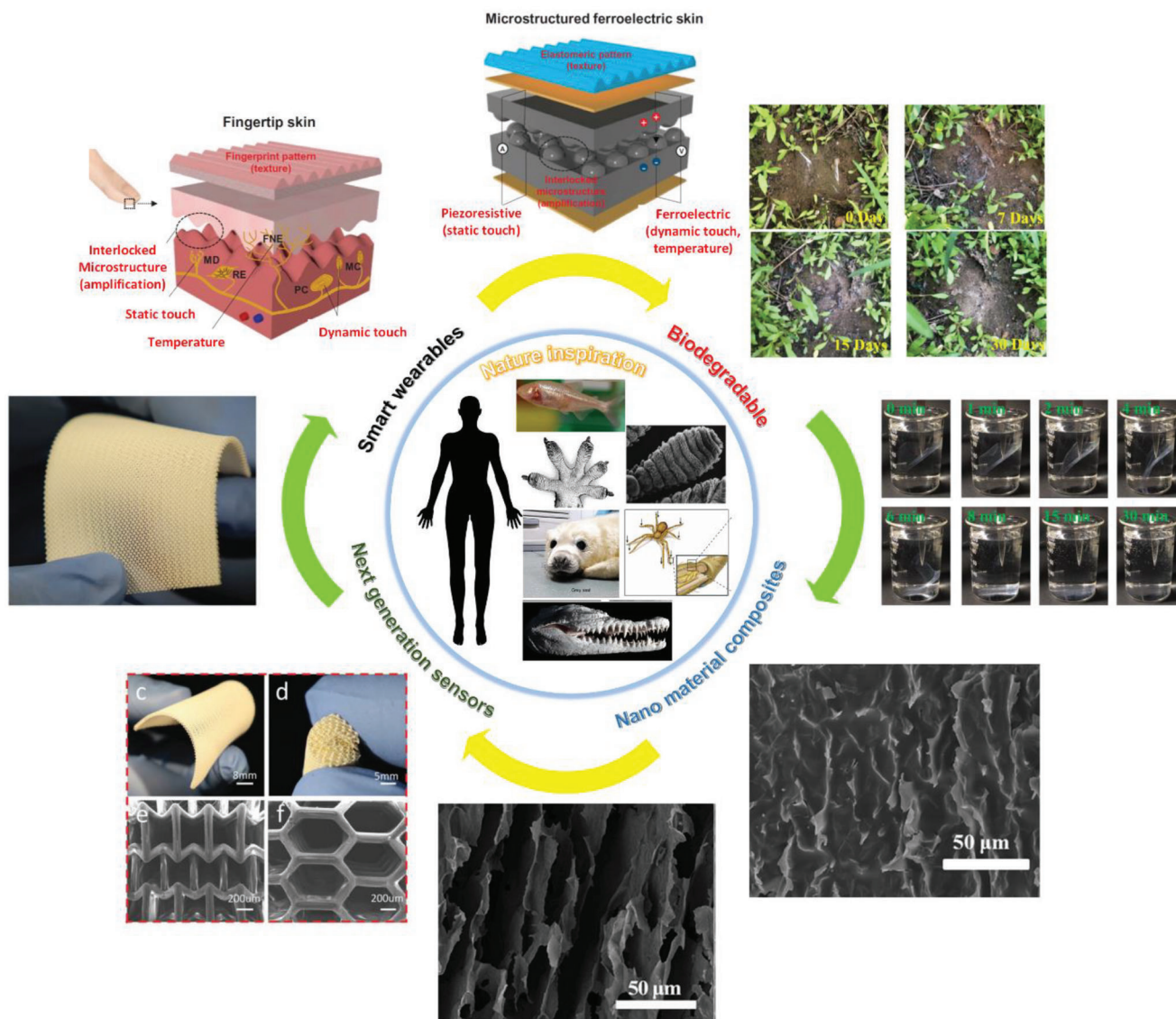


Figure 1. Synergy: biomimetics and nanoengineering for next-generation wearables. Reproduced with permission.^[1] Copyright 2015, American Association for the Advancement of Science. Reproduced with permission.^[2] Copyright 2020, Elsevier B.V. Reproduced with permission.^[3] Copyright 2022, Elsevier B.V. Reproduced with permission.^[4] Copyright 2007, Taylor & Francis. Reproduced with permission.^[5] Copyright 2007, Wiley-VCH GmbH & Co. Reproduced under the terms of the Creative Commons CC BY license.^[6] Copyright 2016, the Authors, published by Springer Nature. Reproduced under the terms of the Creative Commons CC BY license.^[7] Copyright 2022, the Authors, published by Wiley VCH. Reproduced with permission.^[8] Copyright 2012, The Company of Biologists Ltd. Reproduced with permission.^[9] Copyright 2014, Macmillan Publishers Limited.

engineers. For instance, crocodilians have a combination of slowly and rapidly adapting dome-shaped pressure receptors collectively referred to as integumentary sensory organs (ISO).^[8] These ISOs impart them with mechanical sensitivity enabling them to sense water movement and tactile feedback on items held in the jaw.^[8] Spiders have crack-shaped slit organs near their leg joints to detect minute vibrations, which have inspired researchers to design crack-based microstructure for piezoresistive sensing.^[9,10] In another inspirational example, researchers were inspired by hierarchical structures that enabled reversible adhesion in the gecko's feet to engineer a synthetic analogue to the gecko adhesion system.^[11] More recently, a considerable amount of research effort has been dedicated to understanding the skin

and its underlying mechanoreceptors, which form the backbone of our somatosensory perception.

The never-ending demand for a better quality of life postindustrial revolution has led to exponential growth in the consumer goods industry focusing on comfort and convenience. With the growth of semiconductor processing in the last century, personal high-performance electronics gadgets have become easily accessible to the masses. In particular, with the rise of flexible materials processing in the last two decades, consumer electronics are slowly inching toward the realms of science fiction. Today, a variety of health data entailing heart rate, step count, cadence, VO₂ max, blood oxygen saturation, etc. can be accessed on our smartphones using standard commercial fitness trackers. Many

of such devices rely on MEMS-based inertial sensors. Though wearables have progressed a lot in the last 20 years, the current state of MEMS and the recent upsurge of research conducted in flexible electronics-based wearables leaves a lot more possibilities to be explored. For instance, most of the wearables in the market are not very reliable and their fragile nature together with associated complex data processing and IoT integration prohibits their use in skin-mountable applications involving human physiological parameters and human electrophysiological signal monitoring.

The next generation of wearables would require highly desirable features like skin conformality, biocompatibility, degradability, and self-healability. Furthermore, such sensors need to be cost-effective, reliable, and robust for consumer use. Fortunately, nature can offer invaluable design cues for the development of next-generation wearables. For instance, skin, because of its ultrasensitivity toward innocuous and noxious stimuli and self-healability can be our inspiration for developing the next generation of wearable sensors. The need of the hour is to achieve a synergy between biomimetics and nanomaterials engineering to develop functional materials for next-generation wearables.

This article mainly explores the state of the art existing in the field of skin-inspired sensors encompassing nanomaterials engineering and biomimicry (Figure 1). Section 2 briefly describes the anatomy of the skin and its underlying mechanoreceptors. Section 3 provides a comprehensive review of skin-inspired mechanical sensors. Section 3 is subdivided into subsections where the history of piezoresistive, capacitive, and piezocapacitive sensing is introduced. With the concepts of piezoresistive and capacitive sensing established, this article dives into the inner world of wearable mechanical sensors entailing, fibrous structure-based sensors, nanomaterial–polymer composites-based planar sensors, and 3D porous structure-based sensors. In addition to piezoresistive and piezocapacitive sensing, a dedicated section discussing and summarizing the origin and recent advances in the field of triboelectric effect-based self-powered wearable sensors is included for the sake of completeness. Finally, the paper concludes by summarizing the developments in the field of bioinspired wearable electronics along with future trends and challenges to overcome.

2. Anatomy of Skin and Its Relevance to Flexible Electronics

Years of evolution have bestowed human beings with well-developed somatosensory perception. The somatosensory system has two distinct functions, namely, exteroceptive/interoceptive (perception and reaction to external or internal stimuli) and proprioceptive (also referred to as kinaesthesia—perception and control related to the position of the body). Much of the human somatosensory perception is enabled by skin which is the largest organ of the body. Underlying the skin are mechanoreceptors or mechanosensitive sensory neurons, which enable the skin to sense both innocuous and noxious stimuli (Figure 2a).^[12] The mechanoreceptors that are relevant for tactile perception can be further subcategorized into low-threshold mechanoreceptors (LTMRs—responsible for detecting innocuous stimuli) and high-threshold mechanoreceptors (responsible for detecting noxious stimuli). The fast-conducting myelinated afferent neurons (type

$A\beta$ —nerve endings of β -type A fibers are heavily myelinated and large with a conduction velocity in the range of 16–100 m⁻¹ s), which conduct signals from the LTMRs present in certain areas of the body (like glabrous skins of hand or foot sole) to the brain are grouped as tactile afferents. Proprioceptive afferents responsible for the information on the orientation of joints and muscle states are also fast-conducting myelinated afferent neurons. Even the simplest of tasks such as grabbing a glass of water or holding a pen require complex coordination between the tactile and proprioceptive afferents without which day-to-day tasks become challenging.^[14] For instance, when we grasp an object with our fingers, both the tactile and proprioceptive afferents work in tandem to relay information to the brain regarding object texture, required grasping force, and friction.^[14] The schematic in Figure 2b shows the end organs innervating the glabrous skin of the human hand/foot sole. The four types of mechanoreceptors shown in the schematic are responsible for the mediation of innocuous touch.^[13] As seen in Figure 2b, a single $A\beta$ fiber branches into enlarged nerve terminals finally terminating with a cluster of Merkel cells forming the Merkel cell–neurite complex at the basal region of the epidermis, which enables us to resolve complex spatial images of tactile stimuli.^[13] The sense of movement across the skin is enabled by Meissner corpuscles and their characteristics RAI-LTMR responses. Ruffini endings, which lie in the deep dermis, are associated with SAI-LTMR and are responsible for the sensation of skin stretch. Finally, the sense of vibration is enabled by the onion-like organelles called Pacinian corpuscles encapsulating the ending of $A\beta$.^[13]

Touch perception is essentially a team effort between cutaneous LTMR endings and central nervous system circuits, which convert a physical stimulus on the skin into neural codes that are subsequently interpreted by the brain (parietal lobe region). As such, LTMRs are of particular interest to the flexible sensors community as they form the fundamental backbone of tactile perception.

Skin which is arguably one of the most important constituents of the somatosensory system can be considered a highly sophisticated large-area pressure, strain, temperature, and vibration sensor. Skin performs a multitude of sensing tasks while being extremely robust, self-healing, and reliable at the same time. All these excellent properties of skin make it an ideal candidate for biomimicry and subsequent development of next-generation smart e-skins and wearable devices. The following sections further discuss the existing state-of-the-art skin-inspired mechanical sensors entailing mechanical, temperature, and humidity sensors.

3. Skin-Inspired Mechanical Sensors: Most Common Sensing Mechanisms

One of the primary functions of the skin is to enable the sense of touch. Different somatosensory neurons innervating the skin enable the sensation of tactile stimuli. For instance, light innocuous touch is enabled by $A\beta$ afferents, which have a low threshold.^[12] Due to its exceptional ability to discriminate between innocuous touch and noxious stimuli, the skin is considered an extraordinary mechanical sensor and has inspired researchers to develop biomimetic sensors for soft

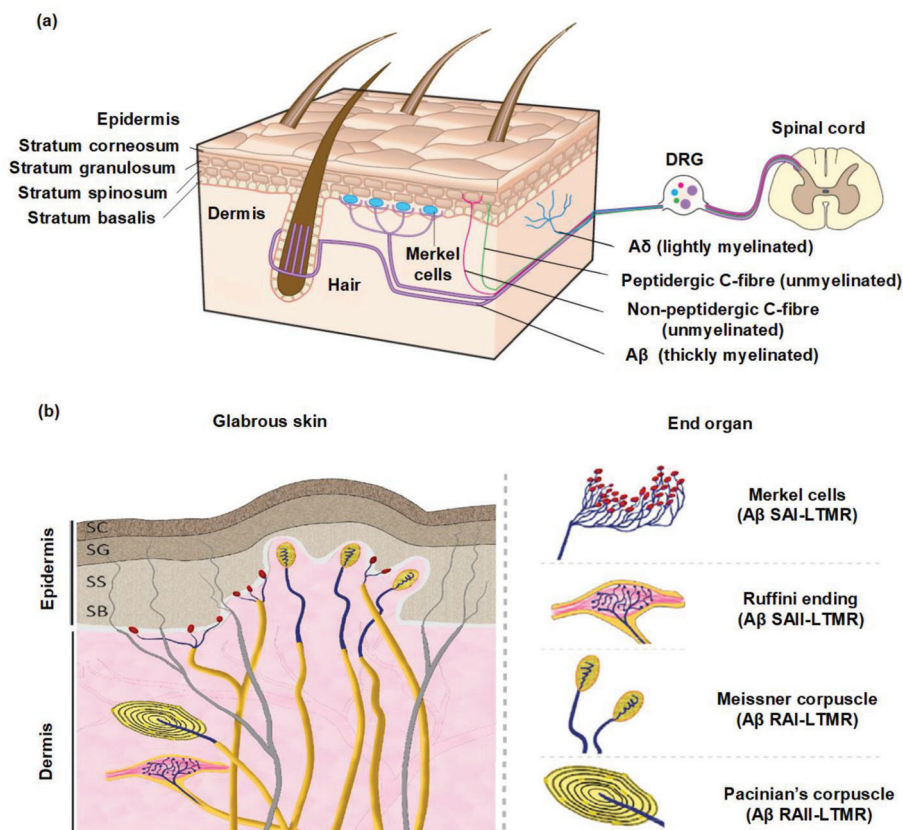


Figure 2. Skin and its underlying mechanoreceptors. a) Schematic showing the mechanoreceptors innervating the skin. Reproduced with permission.^[12] Copyright 2007, Nature Publishing Group. b) Schematic showing the mechanoreceptors innervating the glabrous skin commonly found in the human hand or foot sole. Reproduced with permission.^[13] Copyright 2013, Cell Press.

robotics and smart wearables.^[15–17] Mechanical sensors typically convert mechanical stimuli such as strain/deformation, pressure, and vibration to an interpretable electrical signal.

Traditional mechanical sensors have been around since the time of the Industrial Revolution. Some classic mechanical sensors like the pressure gauge predate the Industrial Revolution. Torricelli's famous experiment with the mercury barometer was the first documented pressure gauge. Since then, pressure sensors have evolved to become highly sensitive and miniaturized. Similarly, strain gauges have been around for a while since their initial introduction in 1938. However, with rapid progress in the field of semiconductor processing and polymer-based flexible electronics in the last few decades, there has been renewed interest in developing next-generation flexible mechanical sensors, which is nothing short of a modern renaissance. Recently, flexible mechanical sensors have been applied for a multitude of human physiological monitoring applications and soft robotics.^[18–21] In particular, wearable mechanical sensors reported lately can track a multitude of vital human physiological parameters including pulse rate,^[19] gait,^[22,23] respiration rate,^[24] and various joint movements.^[18,25,26]

In general, based on their underlying sensing mechanism, mechanical sensors can be categorized into piezoelectric,^[27–31] capacitive,^[32–35] piezoresistive,^[25,26,36–40] and others (such as

triboelectric,^[41,42] optical,^[43,44] and transistor,^[45–47] based). Of all the major sensing mechanisms, capacitive and piezoresistive sensing mechanisms remain the most popular and widely used because of their simple implementation, excellent resolution, and superior static and dynamic sensing performance.^[48] More recently, triboelectric self-powered sensing has gained traction fueled by the rise in demand for ultralow/self-powered energy-efficient wearable devices.^[49–53] In the following subsections, recent developments in skin-inspired resistive and capacitive-type mechanical sensors along with their underlying sensing mechanisms are discussed. Toward the end, a dedicated section summarizing the progress in the field of triboelectric nanogenerator (TENG)-based wearable sensors for human physiological parameters monitoring is included for the sake of completeness.

3.1. Piezoresistivity: A Brief Historical Background

Fundamentally, any resistive type of mechanical sensor is based on the principle of external physical stimuli-induced resistance change. The resistance of an object is expressed as $R = \rho \frac{l}{A}$, here ρ represents the resistivity of the material, l represents the length, and A the cross-sectional area. Any resistive type of device relies on either of the following mechanisms.

- Geometric change: As seen from the resistance expression, any geometric deformation of a material leading to a change in its length and cross-sectional area while keeping the resistivity “ ρ ” constant leads to a resistance change.
- Intrinsic piezoresistivity: In many materials the resistivity “ ρ ” changes as a result of external stimulus. For instance, semiconductors like silicon (Si), germanium (Ge), carbon nanotubes (CNTs), and graphene demonstrate intrinsic piezoresistive behavior owing to changes in their electronic band structure, interatomic spacing or change in barrier height upon stress.^[48]
- Piezoresistivity in nanomaterial–polymer composites: This is a class of piezoresistivity typically observed in nanomaterial–polymer composites where the nanomaterial fillers form a percolation network. Recently, a significant amount of research has been conducted to develop devices harnessing the piezoresistive effect observed in polymer nanomaterial composites.^[48] The strain/stress-induced resistance change can be explained by invoking the conductive domain discontinuity mechanism^[18,20,54–56] or Simmon’s tunneling resistance theory.^[57,58]

From its initial inception, strain gauges have undergone a series of modifications with the advent of microfabrication technology. With the advent of semiconductor technology, semiconductor strain gauges started replacing metallic strain gauges owing to their superior sensing performance with gauge factors often reaching two orders of magnitudes higher than the conventional metallic ones.^[59]

The effect of dimensional changes in semiconductor strain gauges is negligible compared to the change in intrinsic material resistivity upon the application of stress. The piezoresistive effect in silicon and germanium was first reported by Smith in 1953. The results were expressed in terms of a pressure resistance coefficient and two shear coefficients. One of the shear coefficients was exceptionally large and could not be explained by the mobility effect and the volume energy gap effect.^[60] Smith invoked Herring’s “many-valley” model^[61] to explain the large shear constant observed in his experiments.^[60] The population of the valleys changes because of changes in energies arising from the application of an anisotropic stress.^[62]

The miniaturization drive starting with the development of integrated circuit technology in the latter half of the 20th century led to device dimensions reaching nanoscale. Implementation of traditional sensing mechanisms like piezoresistive, optical, and capacitive sensing proved to be challenging at the nanoscale owing to their physical limitations such as wavelength limitation of optical sensing and surface area limitation of capacitive sensing. In particular, diffused semiconductor piezoresistors were rendered unsuitable for sensing applications owing to significantly increased resistance and associated resistance noise at the nanoscale.^[63,64] The discovery of CNTs^[65] in 1991 and graphene^[66] in 2004, opened up new possibilities where nanostructured materials with excellent mechanical and electrical properties could potentially be utilized for piezoresistive sensing applications at the nanoscale.

In one of the earliest demonstrations of piezoresistivity in an isolated suspended single-walled carbon nanotube (SWCNT), Tomblor et al. showed that the conductance of a suspended SWCNT changes by two orders of magnitude when depressed/deflected with an atomic force microscope (AFM) tip thus straining it in the process.^[67] As shown in the schematic in Figure 3a (top inset), an isolated SWCNT was placed between two metal electrodes on SiO₂/Si substrate with a narrow trench lying midway between the electrodes on the SiO₂ thus suspending a part of the SWCNT. The middle image of Figure 3a shows the AFM image of the suspended part of the SWCNT with a suspension length of 605 nm. For the resistance measurement experiments, the AFM probe tip was placed at the center of the suspended section of SWCNT, and the sample stage was moved upward to cause a deflection in the SWCNT followed by a retraction step to relax. This push–retract cycle was repeated multiple times and resistance data was logged as a function of time. The conductance of the SWCNT as a function of strain and bending angles is shown by the plots in Figure 3b (left). The authors observe that the change in conductance is relatively slow for small bending angles ($\theta \leq \approx 5^\circ$). There is a drastic change for angles exceeding 5° as shown in Figure 3b (left inset). To understand and explain the underlying mechanism behind this strain-induced conductance change phenomenon, the authors conducted an “order-N-orthogonal tight-binding molecular dynamics simulation” involving an AFM tip deflecting a (5,5) SWCNT at 300 K.^[67] The plot in Figure 3b (right) shows the evolution of conductance with band energy for progressive deformation (strains 0, 0.7%, 1.8%, and 3.4%). As observed from the plot, the conductance (units of $G_0 = 2e^2/h$) at the Fermi level was found to decrease from $2 G_0$ at 0% strain to $1 G_0$ at 0.7% strain ($\theta = 7^\circ$). For larger strain/deflection, the change was observed to be more dramatic ($G = 0.01 G_0$ at 3.4% strain). The authors attributed the dramatic change in conductance to the local bond deformation caused by the AFM tip. The simulations led to the conclusion that at higher strains, the bonds near the tip change from sp² to sp³ hybridization state, which is subsequently reflected by the decreased conductivity. The simulated atomic configurations shown in Figure 3c represent the SWCNT configurations at $\theta = 7^\circ$ and 15° . As seen in the simulated configuration, for a relatively larger deflection of 15° , the atoms near the tip (not shown) marked in red are sp³ bonded.

Stampfer et al. built up on the fundamental findings of Tomblor et al. and applied them to develop a nanoelectromechanical system based on an isolated SWCNT.^[63] The schematics in Figure 3d show the concept behind the displacement sensing employing suspended SWCNT. The suspended CNT of length L_{NT} is placed between two conductive electrodes marked “S” and “D”. The nanotube is also physically connected to the object that is being displaced, which is a cantilever in this case as shown by the bottom schematic in Figure 3d. The SEM image in Figure 3e (top) shows the fabricated device with the SWCNT (length ≈ 600 nm and diameter 1.2 nm) placed beneath a released 200 nm wide and 1.5 μm long Au cantilever. The SWCNT is displaced by contacting the Au cantilever with an AFM tip at point “P” and applying a force “F” as shown by the AFM image in Figure 3e (bottom) thereby deflecting the SWCNT by a distance Z . The plot in Figure 3f shows the resistance R of the SWCNT as a function of deflection for three cycles. The remarkable recovery

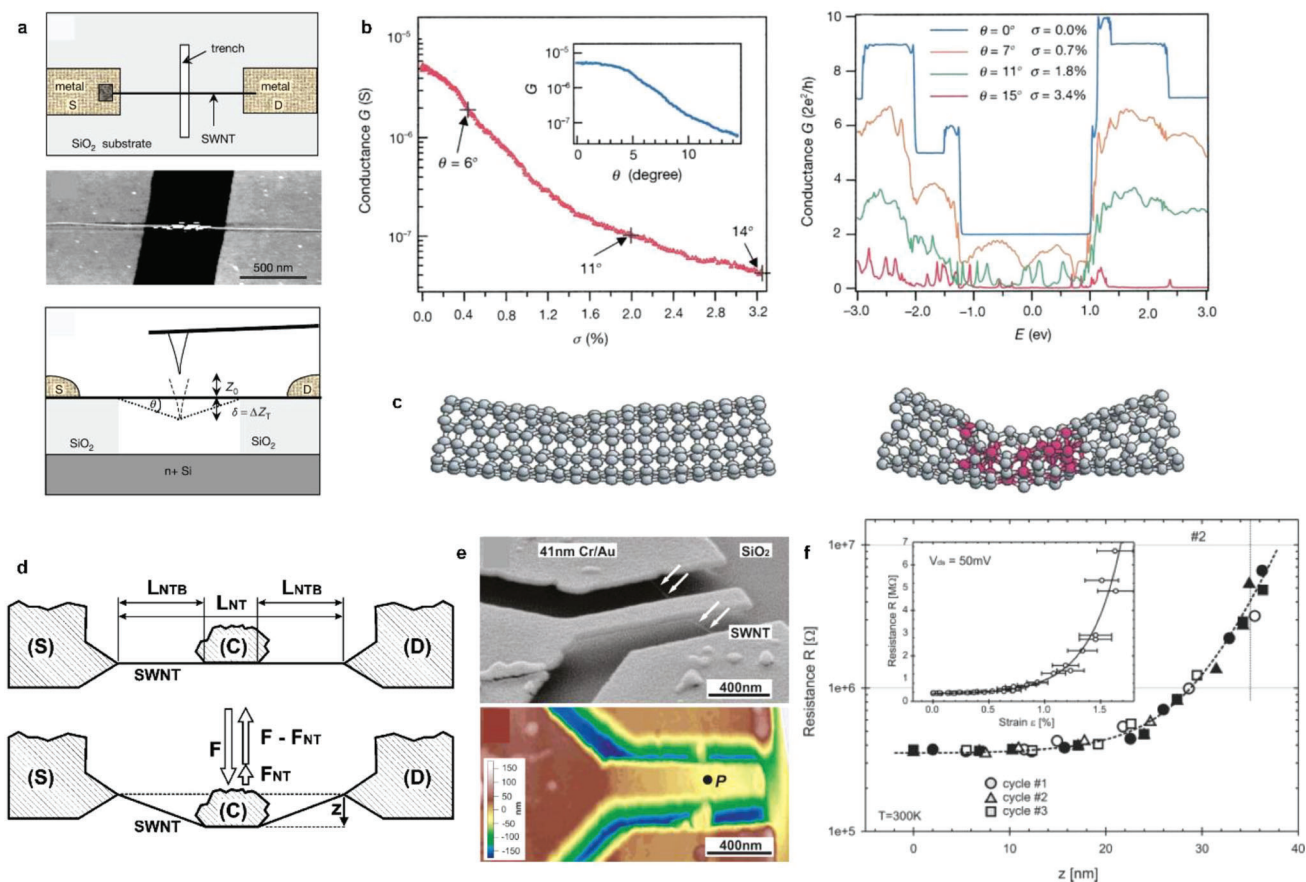


Figure 3. CNT-based piezoresistive sensing. a) Schematic representation of the experimental setup for assessing the conductance change of SWCNT with strain. AFM image of the suspended SWCNT over trench. Schematic representation showing side view of the experiment with AFM tip. b) Plot showing the conductance change as a function of strain (σ) and the inset showing conductance as a function of bending angle θ . c) Showing the simulated atomic structures of the SWCNT when deflected with an AFM tip for bending angles $\theta = 7^\circ$ and 15° . The atoms marked in red are sp^3 bonded.^[67] Reproduced with permission.^[67] Copyright 2000, Macmillan Magazines Ltd. d) Schematic representation of the experimental setup for the demonstration of SWCNT-based displacement sensor; the bottom schematic shows the center of the SWCNT being deflected with the gold cantilever aligned on top. e) SEM image of the real device with SWCNT below the gold cantilever. The bottom AFM image shows the tapping mode image of the device. f) Plot showing the resistance change versus cantilever displacement “z”. The top inset shows the resistance as a function of strain.^[63] Reproduced with permission.^[63] Copyright 2006, American Chemical Society.

characteristics of the resistance change curve suggested that the SWCNT worked in a linear elastic regime. Unlike in the case of Tomblor’s work,^[67] the authors attribute the nonlinear behavior of the resistance change versus displacement characteristic to changes in the bandgap of CNT. However, the authors did suggest that the effect of local sp^2 to sp^3 transition at the point where AFM tip contacts the CNT (Kinking effect in short) could also possibly influence the measurements and contribute to the observed nonlinear behavior. The upper inset in Figure 3f shows the resistance plotted as a function of strain in the nanotube. Gauge factors were extracted for two separate samples and were reported to be in the range of 2900. The high gauge factor figure coupled with the nanometer dimensions of the nanotube posed an alternate attractive proposition to silicon-based strain gauges with significantly less gauge factors.

The discovery of piezoresistive behavior in carbonaceous materials like CNT opened up a new paradigm in the field of micro-fabrication. Furthermore, with the discovery of the wonder ma-

terial graphene,^[66] which is essentially the fundamental building block (or rather sheet) of all sp^2 carbon structures, 2D nanomechanical systems with nanoscale diaphragm-like structures became a reality. The discovery of graphene raised immense interest in material science research across the globe which led to several research labs studying its mechanical^[70] and electrical properties.^[68,71] Lee et al. for the first time measured the intrinsic breaking strength and elastic modulus of monolayer graphene employing the nanoindentation method^[70] and confirmed graphene to be the strongest material to be ever measured. Geim and Novoselov have commented on the various desirable characteristics of graphene (crystalline quality, resilience to high current density, and high carrier mobility), which qualifies it as the “rapidly rising star on the horizon of material science and condensed-matter physics.”^[72]

Pereira et al. theoretically explored the effect of tensional strain on the electronic structure of graphene.^[71] Piezoresistivity in monolayer graphene has been exploited by Smith et al.

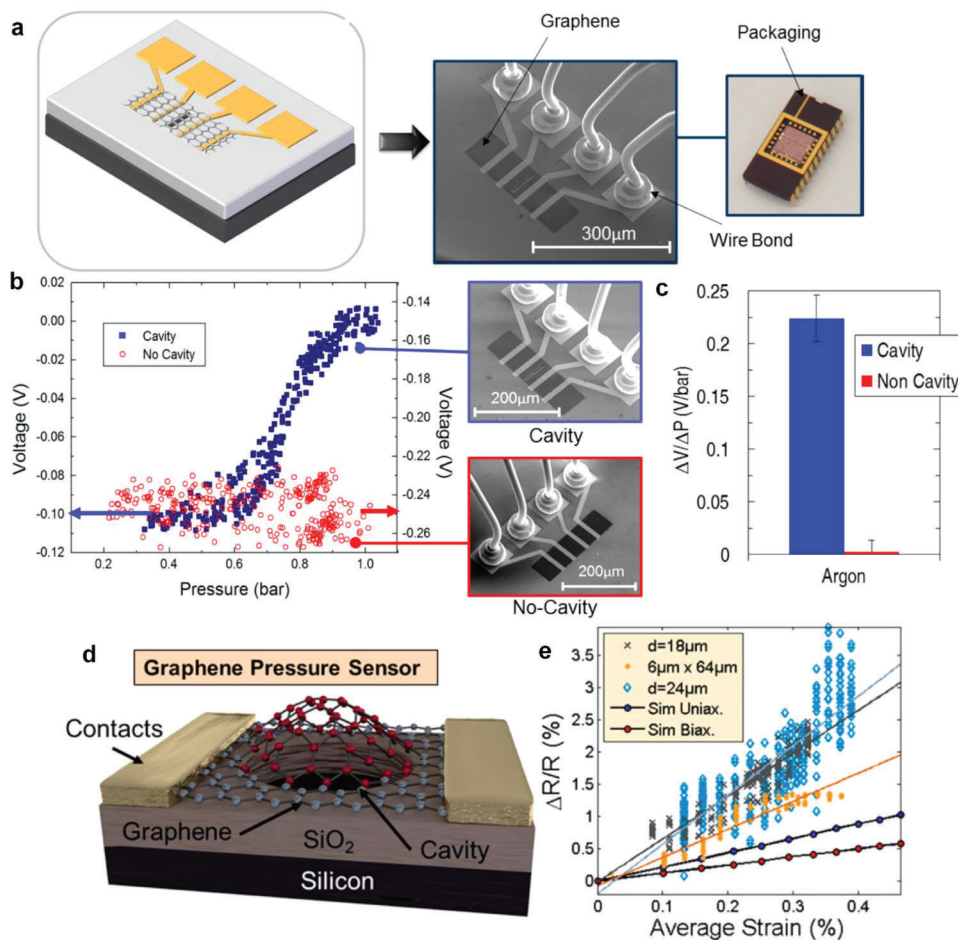


Figure 4. Suspended monolayer graphene-based piezoresistive sensing. a) Schematic representation of the device entailing suspended graphene on trench etched on SiO₂ film on Si substrate. SEM image of the actual device with wire bonding. Photograph of the packaged sensor. b) Plot showing the amplified voltage signal as a function of pressure for two devices (with and without cavity). c) Bar plot comparing the average change of voltage per unit pressure for the devices with and without cavity.^[68] Reproduced with permission.^[68] Copyright 2013, American Chemical Society (further permission related to the material excerpted should be directed to the ACS). d) Schematic representation of the device for biaxial strain sensing employing suspended graphene. e) Plots comparing the experimental and simulation results of percentage resistance change versus strain for three devices comprising two devices for biaxial sensing and one device for uniaxial sensing configuration. Reproduced with permission.^[69] Copyright 2006, American Chemical Society.

to demonstrate an NEMS pressure sensor.^[68] The fabricated device entailed chemical vapor-deposited graphene membranes suspended on etched trenches in SiO₂ film on a Si substrate. The schematic in **Figure 4a** shows the graphene membrane suspended over the SiO₂ trench with the electrodes for electrical contacts. The SEM image and the photograph in **Figure 4a** show the wire-bonded fabricated device and the device after being packaged. The device works based on the pressure differential between the inside and outside of the cavity, which leads to the graphene membrane being deflected causing a change in its resistance, which is measured with an external Wheatstone bridge circuit. To confirm the mechanical bending as the cause behind resistance change, identical devices without cavities were tested alongside the suspended graphene devices. The plot in **Figure 4b** shows the voltage signal (amplification factor 870) from the two devices in response to pressure. It is observed that the voltage output correlates strongly with the pressure condition in the case of the device with cavities thus confirming the piezoresistive effect

in suspended graphene. The bar plot in **Figure 4c** compares the average change in voltage per unit pressure for three devices with and without cavity. The authors conducted a multiphysics-based simulation to estimate the suspended diaphragm deflection, calculate the strain, and compare it with the resistance change for the suspended part of the graphene diaphragm to extract the gauge factor. The gauge factor was found to depend on pressure range with a maximum gauge factor of 4.33 with an average value of 2.92.

Smith et al. extended upon their previous work (described above) and reported experimental and theoretical data on both uni/biaxial piezoresistive properties in suspended graphene membranes.^[69] The authors explored the effect of uniaxial and radial strain on piezoresistive properties of graphene employing different sensor geometries comprising of rectangular trench (as seen previously in **Figure 4a**) and circular cavity and subsequently transport calculations were performed using linearized Boltzmann transport equation. The schematic in **Figure 4d** shows the

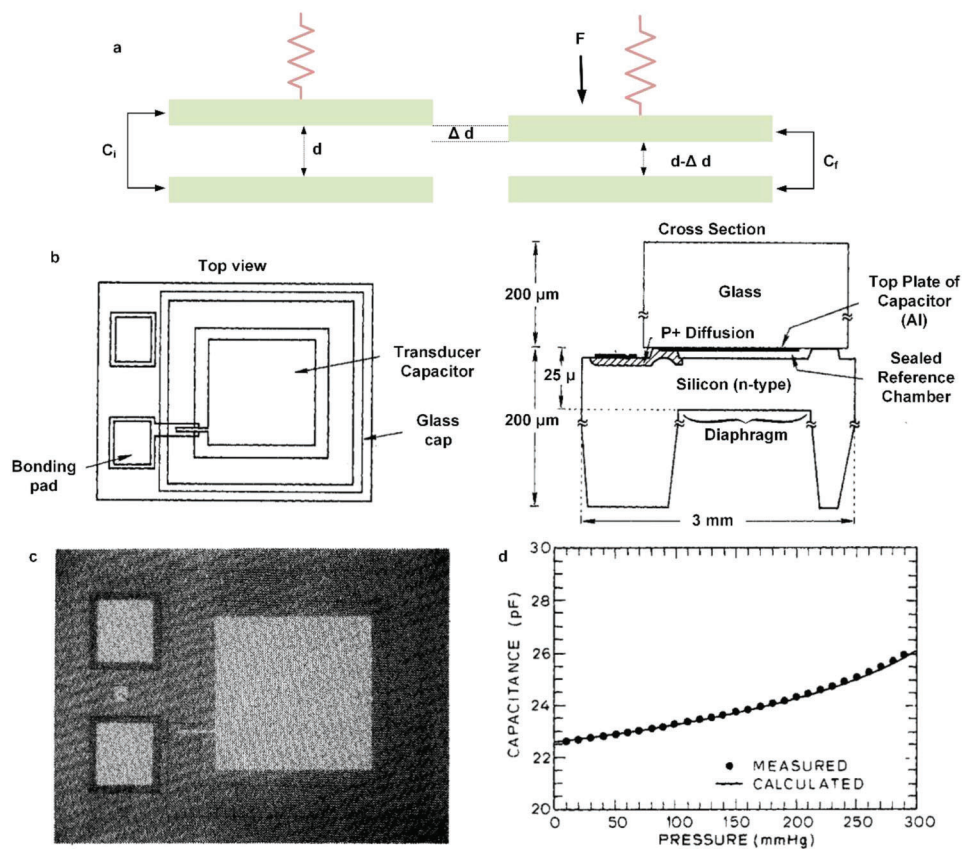


Figure 5. Parallel plate capacitive sensor. a) Schematic explaining the working principle of parallel plate capacitive sensor with a single movable electrode. b) Structure of a silicon-based monolithic capacitive pressure sensor. c) Image of the actual device. d) Plot showing the experimental and calculated pressure capacitance change response of the sensor. Reproduced with permission.^[77] Copyright 1980, IEEE.

device utilized for the investigation of biaxial/radial strain. The plot in Figure 4e compares the percentage change in resistance of active/suspended area for three sensor geometries in response to strain. The experimental results are also compared with the simulation results for both the cases of uniaxial and biaxial strains. Based on the findings the authors concluded that strain direction plays a role in the piezoresistive property of graphene. Furthermore, the gauge factor was found to be independent of the crystallographic orientation and the doping concentration.

Though Si, Ge, graphene, and CNTs demonstrate intrinsic piezoresistivity and associated large gauge factors, their physical form and mechanical properties like stiffness and rigidity render them unusable for applications requiring wearability, flexibility, and robustness. Fortunately, for the last two decades, the sensor community has moved beyond the boundaries of intrinsic piezoresistivity observed in semiconductors and carbonaceous materials like graphene and CNTs. Some of the earliest proponents of nanomaterial-polymer composites-based flexible sensors demonstrated, that, by dispersing nanomaterial fillers in flexible polymeric substrates/bases near the percolation threshold, high piezoresistive gauge factor/sensitivity can be achieved.^[73–75] Later in the article, we discuss the advances and recent progress in the field of wearable/flexible piezoresistive sensors employing various 0D, 1D, and 2D nanomaterial fillers.

3.2. Capacitive and Piezocapacitive Sensing

Although resistive sensors have dominated the sensing landscape for more than a century, problems associated with temperature drift and high-power budget have always motivated designers and researchers to explore more robust and power-efficient alternate techniques for strain and pressure sensing applications. In contrast to resistive type sensors, capacitive (and more recently piezocapacitive) sensors offer an attractive alternative as they operate on a significantly lesser power budget because of the lack of flow of direct current. In addition, capacitive sensors demonstrate high sensitivity, faster response time, and are less prone to temperature drift and hysteresis.

Traditional parallel plate capacitor entails two conducting electrodes separated by a dielectric medium. If the fringe effects are neglected, the capacitance of a capacitor can be expressed as $C = \frac{\epsilon_0 \epsilon_r A}{d}$ where ϵ_0 represents the absolute permittivity of the vacuum, ϵ_r represents the dielectric constant of the dielectric medium separating the electrodes of the capacitor, “A” represents the area of the electrodes, and “d” represents the gap between the electrodes. The schematic in Figure 5a represents a parallel plate capacitive sensor with air as the dielectric medium. The top plate is suspended with a spring/cantilever whereas the bottom plate is fixed. When a force F is applied to the top plate, the spring

extends thereby allowing the gap between the electrodes to change by a small displacement Δd . The change in capacitance is given by

$$\Delta C = C_f - C_i = \epsilon_0 \epsilon_r A \left(\frac{1}{d} - \frac{1}{d - \Delta d} \right) \quad (1)$$

This change in capacitance can be resolved with matched measurement circuitry. Furthermore, the force sensitivity can be resolved by considering the spring equation and relating it to the capacitance equation. It follows that traditional capacitive-type sensors rely on the displacement of electrodes and can be considered displacement sensors as opposed to piezo-sensors, which rely on stress development in the pressure-sensing membrane. Marx and Bell introduced one of the earliest capacitive pressure sensors for automotive applications.^[76] The design comprised a moving electrode capacitor with measurement circuitry that resulted in a voltage output proportional to the input pressure stimuli.

With the growth of silicon micromachining technology in the 1980s there was a keen interest among microsystem designers to exploit the existing state-of-the-art for developing on-chip silicon-based capacitive pressure sensors. In one of the earliest demonstrations of silicon micromachining based capacitive sensors, Sander and Knutti reported a microminiature monolithic parallel plate capacitive pressure sensor with a pressure sensitivity 20 times more than a piezoresistive strain gauge-based pressure sensor.^[77] The sensor could be batch manufactured through existing integrated circuit fabrication technology and could operate at one percent of the power budget of a piezoresistive pressure sensor. The device comprised a top metalized glass plate and a silicon diaphragm separated by a gap of 2 μm (refer to schematic in Figure 5b). On application of pressure, the diaphragm moves closer to the fixed glass plate and there is an overall change in capacitance. Figure 5c shows the image of the pressure sensor. Theoretical and experimental capacitance pressure calibration is shown by the plot in Figure 5d. To isolate the capacitor from stray lead capacitances, the authors fabricated a second sensor that incorporates on-chip bipolar circuitry.

From the discussion on the simple sensing mechanism employed by traditional parallel plate capacitive sensors, it follows that the structural property of the dielectric layer has a profound impact on the sensing performance. Though traditional capacitive pressure sensors rely on the changing distance “ d ” between the electrodes, more recently, methods are being investigated to achieve pressure-induced dielectric constant “ ϵ_r ” change to achieve enhanced pressure sensitivity. Furthermore, it is desirable that the dielectric layer has low compressive modulus, which will further contribute toward enhancing the pressure sensitivity. In the past, elastomeric materials with microstructured air voids have been employed to enhance the sensing performance of capacitive sensors.^[78–80] In contrast to traditional capacitive sensors which are essentially displacement-based sensors, piezo-capacitive sensors rely on stress buildup on the membrane material, which leads to dielectric constant change thereby leading to capacitance change in addition to the regular electrode displacement.^[81]

In one of the earlier works, Metzger and Fleisch demonstrated an indirect method of utilizing polyolefin foam for developing ca-

pacitive pressure sensor arrays for inexpensive object detection applications.^[80] The work featured polyolefin foams (thickness of 250 μm and dielectric constant of 1.7) with surface-mounted pressure sensor arrays arranged in 12×8 matrix form within an area footprint of $30 \times 20 \text{ cm}^2$. The image in Figure 6a shows a cross-section of the foam with large anisotropically shaped voids throughout the thickness. The sensor was tested for force sensitivity by loading a 1 cm^2 sensor area with various fixed weight loads and the load versus capacitance change is plotted as shown in Figure 6b. The authors report a load resolution of 10 g cm^{-2} . The plot in Figure 6c shows capacitance change for 10 g cm^{-2} load (per unit area).

In a pioneering work, Mannsfeld et al. from Bao’s group demonstrated a microstructured polydimethylsiloxane (PDMS)-based large area flexible capacitive sensor array with fast response.^[78] The microstructured PDMS film was fabricated by a soft lithography approach entailing the pouring of PDMS prepolymer to a silicon wafer mould (with inverted pyramidal cavities), subsequent curing, followed by deposition of indium titanium oxide polyethylene terephthalate (ITO–PET) electrodes to form the sensor (shown schematically in Figure 6d). Three different sensors involving unstructured PDMS film, line-structured film, and film with micropylamids were compared. The pyramid structure film showed the highest sensitivity of $\approx 0.55 \text{ kPa}^{-1}$ followed by the linear structured film sensor (0.1 kPa^{-1}). The unstructured film showed the least sensitivity figure of 0.02 kPa^{-1} . The plot in Figure 6e compares the pressure–capacitance change response of the unstructured film with the two microstructured films. The authors attribute the high sensitivity figures to the microstructures, which enable the films to reversibly store and release energy and thereby reduce the negative effects associated with the viscoelastic behavior of the PDMS bulk polymer.^[78]

4. Wearable Mechanical Sensors

4.1. Fibrous Structure-Based Sensors

1D structures such as CNTs^[63] and CNFs^[82] often demonstrate intrinsic piezoresistivity coupled with the advantages of flexibility, conformability, and durability making them suitable for flexible sensor applications. Furthermore, depending on the method of fabrication or synthesis, it is relatively easier to achieve large-area conformal and highly flexible nanofibrous membranes. More recently, nanofibrous membranes have been exploited extensively for developing flexible and stretchable piezoresistive and piezocapacitive sensors.

In the past, several methods including electrospinning, melt electrowriting, solution blowing, hot drawing, self-assembly, etc. have been explored to fabricate fibrous structures.^[83–87] Amongst all the aforementioned methods, electrospinning stands out owing to its inexpensive nature, versatility in processing a large variety of polymers, ability to control fiber morphology by parameter optimization, and capability to fabricate large-area membranes.^[83,88,89] Also, the 1D nanostructure of the electrospun nanofibers allows for high porosity, excellent surface area-to-volume ratio, and superior mechanical performance.^[88]

Wang’s group reported a zinc oxide nanowire (ZnO)/polystyrene nanofiber (PSNF) based piezoresistive strain sensor with PDMS as the substrate material.^[90] The

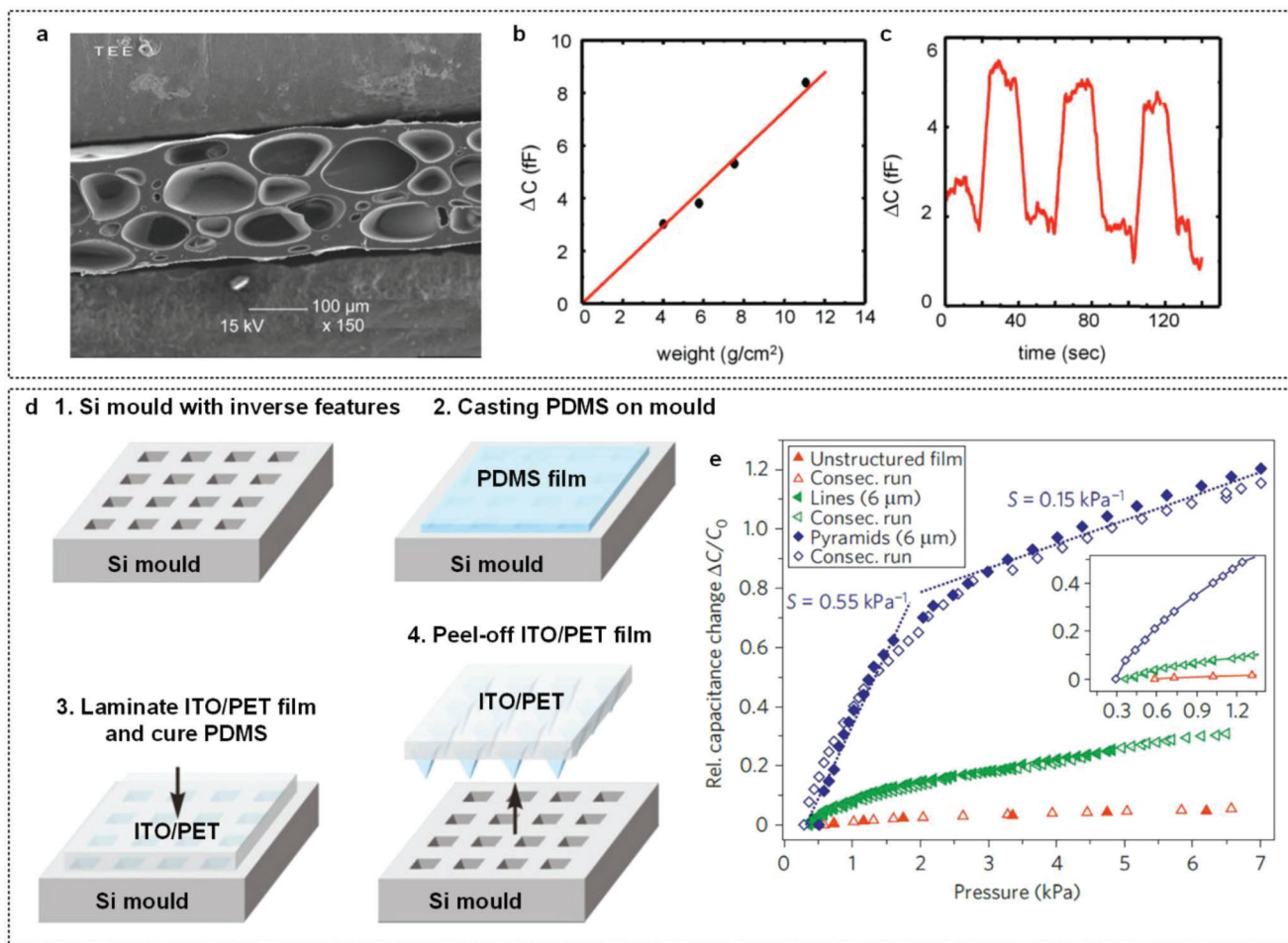


Figure 6. Air void structures and micropatterned polymers for capacitive sensing. a) SEM image of polyolefin foam for capacitive sensor mount. b) Plot showing load (per unit area) versus capacitance change in the sensor. c) Plot showing the sensor response to periodic load (per unit area) $\approx 10 \text{ g cm}^{-2}$.^[80] Reproduced with permission.^[80] Copyright 2008, American Institute of Physics. d) Schematic representation of the process steps involved in soft lithography of the micropatterned PDMS film. e) Plot comparing the pressure versus normalized capacitance change response of the unstructured PDMS to the two microstructured PDMS film-based sensors. Reproduced with permission.^[78] Copyright 2010, Macmillan Publishers Ltd.

sensor featured electrospun polystyrene nanofibers deposited on PDMS film with hydrothermally grown ZnO nanowires along the nanofibers' axes (shown schematically in Figure 7a). The SEM image in Figure 7b shows the morphology of the ZnO/PSNF hybrid structure and the inset shows the structure of ZnO nanowires on a single polystyrene fiber. The nanofibrous structure of the sensor allowed for a relatively higher working strain range ($\approx 50\%$) where the curved nanofibers in the nanofibrous web could release a part of strain by straightening under tension.^[90] The sensor demonstrated a linear strain–resistance change response as observed from the plot in Figure 7c and the gauge factor was reported to be ≈ 116 .

Cai et al. were one of the earliest to investigate intrinsic piezoresistivity in isolated electrospun carbon nanofibers utilizing a MEMS platform.^[82] By studying the microstructures of the fibers, the authors developed a 1D model involving electron tunneling between sp^2 and sp^3 hybridized carbon domains to explain the piezoresistive phenomenon. Furthermore, the role of graphitization and elastic mismatch between the differently hybridized carbon domains on the piezoresistive performance of CNFs

was investigated. Though isolated CNFs were shown to demonstrate piezoresistive behavior with a gauge factor in the range of ≈ 1.96 – 2.55 , their structure and stiffness placed constraints on their applications in the fabrication of flexible and wearable sensors. By contrast, carbon nanofiber bundles or webs offer the added convenience of large surface area, flexibility, and superior strain-bearing capability owing to curvy nanofibers in the web, which help release a part of the strain when subjected to external stress. Ding et al. were among the first to employ a web of electrospun CNFs for achieving flexible strain sensors.^[91] Their sensor featured a freestanding CNF mat sandwiched between two layers of polyurethane as the substrate as shown schematically in Figure 7d. Owing to the randomly oriented nanofibers in the web and the highly elastic thermoplastic polyurethane, the strain sensor demonstrated a high strain bearing ability with a break strain of 480% (stress 20 MPa). The sensor reported a break-in phenomenon for the first few cycles where the baseline resistance changed till the first 10 cycles of uniaxial strain loading. The authors attributed the break-in phenomenon to the irreversible breaking of the CNFs into smaller sections. The plot in Figure 7e

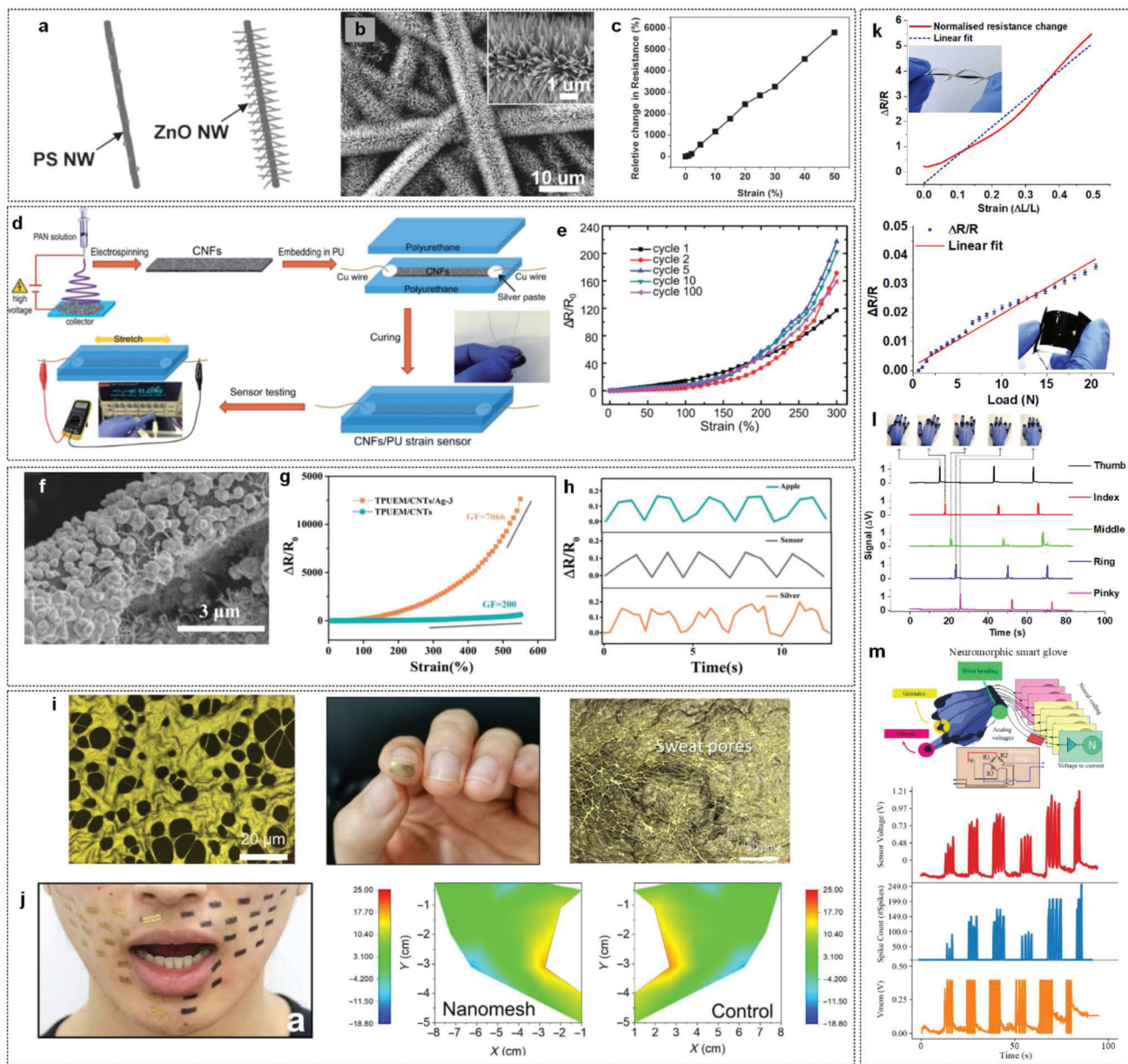


Figure 7. Nanofibrous structures based piezoresistive wearable sensors. a,b) Schematic representation and SEM image of ZnO NW coated polystyrene nanofiber. c) Plot showing strain versus normalized resistance change response of the sensor.^[90] Reproduced with permission.^[90] Copyright 2011, Wiley-VCH GmbH & Co. d) Schematic representation of the process flow in the fabrication of PU-CNF strain sensor. e) Plot showing five distinct cycles of strain versus normalized resistance change response of the CNF-based sensor.^[91] Reproduced with permission.^[91] Copyright 2016, Royal Society of Chemistry. f) SEM image of AgNPs-CNTs decorated TPU nanofiber. g) Plot comparing the strain versus normalized resistance change responses of the CNT decorated and CNT AgNPs decorated TPU nanofiber-based sensors. h) Plots showing the resistance change response of the sensor to phonation sensing experiments.^[92] Reproduced with permission.^[92] Copyright 2019, Wiley-VCH GmbH & Co. i) Left SEM image of the Au/PU-PDMS nanomesh. Center photograph showing the transferred sensor on fingertip. Right image showing the distinguishable sweat pores on the sensor. j) Showing the facial microexpression-related strain mapping employing the sensor.^[93] Reproduced with permission.^[93] Copyright 2020, AAAS. k) Plots showing the strain versus normalized resistance change and force versus normalized resistance response of the CNF-PDMS strain and force sensors.^[37,39] l) Plots showing the response of the CNF-PDMS strain sensors-based smart glove system to a series of individual finger flicks.^[39] Reproduced under the terms of the Creative Commons CC BY license.^[37,39] Copyright 2020, 2021, the Authors, published by Springer Nature. m) Showing the conceptual schematic of the neuromorphic smart glove with the tactile and proprioceptive sensors. Plot (red) showing the voltage signal from an individual tactile sensor in response to tapping. Plot (blue) shows the voltage signal converted into spiking activity LIF neuron model. Plot (orange) shows the membrane potential of the neuron model.^[94] Reproduced with permission.^[94] Copyright 2022, the Authors, Published by ACS.

shows the strain versus relative resistance change response of the sensor for five distinct stretch–release cycles. The largest gauge factor was reported as ≈ 72 for the fifth cycle of stretch–release. The work also demonstrated the applicability of the sensor in human motion monitoring tasks by conducting a series of experiments involving finger, wrist, and elbow joint movements.

Though thermoplastic polyurethane was used as a substrate material in the work by Ding et al. described previously, the excellent mechanical properties of thermoplastic polyurethane (TPU) make them a suitable candidate for electrospinning to form highly stretchable and strong nanofiber webs. Wang et al. reported a fiber-based TPU/MWCNT composite piezoresistive sensor developed by employing the wet-spun method.^[95] As TPU is an insulating material, various methods involving incorporating nanomaterial fillers like graphene and CNTs in the nanofibrous yarns to fabricate piezoresistive sensors have been proposed in the past.^[96,97] Huang et al. reported electrospun TPU nanofibers decorated with CNT and silver nanoparticles (AgNPs) for human physiological parameter monitoring applications.^[92] The work entailed electrospun TPU nanofibers as the structural backbone with subsequent dip coating in CNT dispersion followed by Ag precursor absorption and reduction to form CNT-bridged AgNPs on the nanofibers. The SEM image in Figure 7f shows the surface morphology of a single AgNPs decorated TPU nanofiber with CNTs forming bridging structures between the nanoparticles. The effect of AgNPs on the sensitivity of the strain sensor was assessed by cross-comparing the strain sensing performances of the TPU/CNTs and TPU/CNTs/AgNPs composites as shown by the plot in Figure 7g. The TPU/CNTs/AgNPs-based sensor showed a significantly higher gauge factor of 7066 (strain 550%) in comparison to TPU/CNTs (gauge factor ≈ 200). The practical application of the sensors in human physiological parameters monitoring was demonstrated by conducting a series of experiments involving various joint movement detection, phonation, and gait monitoring.^[92] The plot in Figure 7h shows the distinct phonation map of a subject pronouncing three different words five times each. The ability of the sensor to distinguish between various knee movement patterns while walking, jogging, and running was demonstrated by affixing the sensor to the knee region and acquiring the normalized resistance change signals for the various movement patterns.

Skin interfaceable devices must fulfill various criteria of softness, flexibility, stretchability, thickness of less than 2 μm , and most importantly the ability to achieve conformability of the naturally porous and curvilinear surface of the skin.^[47,93] As observed in the previously described works, most of the sensors featuring porous nanofiber membranes are significantly thick and must be supported by additional polymeric substrates to make them robust.^[90,91] Wang et al. addressed the thickness constraints with nanofibrous membrane-based sensors which can naturally track human skin strain without causing any mechanical disturbance.^[93] The device comprised an electrospun PU nanofiber (diameter 198 ± 52 nm) membrane coated with PDMS elastomer for extra reinforcement. The membrane was coated with 100 nm gold deposition on both sides to complete the device. The device demonstrated excellent robustness and long-term stability with a 3% baseline resistance change for a series of 5000 stretch/release cycles at 60% strain. The SEM image in Figure 7i (leftmost) shows the microstructure of the Au-coated PU–PDMS

nanomesh. To transfer the device to the skin, the authors employed a polyvinyl alcohol (PVA) film as a sacrificial layer. The PVA allows for easy transfer of the nanomesh on the skin owing to its water solubility. The middle photograph in Figure 7i shows the transferred nanomesh sensor on a fingertip and the image on the right shows the distinct sweat pore features of human skin. The skin conformability and easy skin transfer allowed for convenient attachment of the nanomesh sensor on facial skin for facial strain mapping during speech as shown in Figure 7j. The sensor was capable of distinguishing between various facial microexpressions.^[93]

Though carbon nanofibers can be considered an attractive alternative to other nanofibrous structure-based piezoresistive sensors owing to their intrinsic piezoresistive property, high pyrolyzation temperatures required to synthesize carbon nanofibers can potentially restrict their applications for developing affordable wearable sensors. In a series of works, Sengupta et al. demonstrated the application of relatively low temperature (950 $^{\circ}\text{C}$ in contrast to 1200 $^{\circ}\text{C}$ reported by Ding et al.^[91]) carbonized CNF-based stretchable and wearable sensor for tactile sensing, gesture tracking, steady state, and oscillatory flow sensing and skin-inspired neuromorphic sensing applications.^[37,39,94,98] In contrast to the work of Ding et al.,^[91] Sengupta et al. utilized relatively low temperature (950 $^{\circ}\text{C}$ in comparison to commercial CNFs carbonized at 1300–2000 $^{\circ}\text{C}$) pyrolyzed CNF bundles sandwiched between two layers of PDMS elastomeric layers to fabricate piezoresistive strain sensors.^[39] The CNF-PDMS strain sensor demonstrated a linear resistance change response in the 0–50% tensile strain range with a gauge factor of 11.14 as shown by the top plot in Figure 7k. A touch emulation experiment was conducted on the CNF-PDMS tactile sensor and the sensor demonstrated a linear resistance change response in the normal tactile force range 0–20 N with a sensitivity value of 1.82 kN^{-1} as shown by the bottom plot in Figure 7k.^[37] The figure insets in the plots in Figure 7k show the structure of the CNF-PDMS strain and tactile sensors, respectively. The sensor was also capable of responding to oscillatory tactile stimuli in the frequency range of ≈ 10 –610 Hz, which is similar to the sensing range of human glabrous skin.^[37] The applicability of the CNF-PDMS sensor in human physiological parameters monitoring was demonstrated by conducting a series of experiments involving joint movement detection, breathing patterns, and gait monitoring. The proprioceptive ability of the sensors was demonstrated by developing a gesture-tracking smart glove entailing five CNF-PDMS strain sensors secured on a nitrile glove. The plot in Figure 7l shows the response of the system to a sequence of individual finger flicking repeated thrice in a periodic fashion. Furthermore, the gesture-tracking smart glove system was demonstrated to identify 14 unique finger gestures.

To develop true skin-like sensors that mimic the morphology and function of human skin and recreate neural firing, a holistic synergy between flexible sensors and interface neuromorphic circuits is required. For robots to have the ability to seamlessly interact with human beings, they must be endowed with skin-like sensors working in tandem with neuromorphic circuits capable of providing both cutaneous tactile information and haptic proprioception. In follow-up work, Sengupta et al. coupled their previously described CNF-PDMS tactile and strain sensors^[37] with neuromorphic spiking neural networks to achieve skin-inspired

sensing and proprioception.^[94] The work conceptually proposed a smart glove system entailing CNF-PDMS-based piezoresistive pressure and strain sensors coupled with Wheatstone bridge circuits for tactile sensing and proprioceptive perception. The voltage signals from the Wheatstone bridge circuits were converted to current signals and fed subsequently to models inspired by biological neurons (leaky integrate-and-fire simulated artificial neurons), which further encoded the signals into spikes. The schematic diagram in Figure 7m (top) shows the conceptual architecture of the gesture-sensing neuromorphic smart glove. The plots in Figure 7m show the voltage signal (plot in red) from the tactile sensor in response to the periodic tapping pattern and its subsequent conversion to spiking activity (plot in blue) along with the membrane potential of the neuron (plot in orange).

As discussed previously, in contrast to piezoresistive sensing mechanism-based wearable sensors, capacitive and piezocapacitive wearable sensors demonstrate incredibly low power budget, high sensitivity, faster response time, and are less prone to temperature drift and hysteresis. As such, they offer an attractive alternative to resistive type sensors for human physiological parameter monitoring. The use of polymeric dielectric materials with micro air voids has been explored recently by a significant number of research groups to increase pressure sensitivity.^[79,78,80] More recently, there has been a growing interest among researchers in exploiting the air void structures of nanofibrous membranes for the fabrication of skin conformal and wearable piezocapacitive sensors.^[19,81,99–101] As discussed previously the effective dielectric constant of air void structures increases under the application of pressure leading to enhanced sensitivity. In one of the earliest works, Kim et al. demonstrated the utilization of electrospun polyvinylidene fluoride-co-tetrafluoroethylene (PVDF-TrFE) nanofibrous membranes for the fabrication of ultrasensitive piezocapacitive sensors.^[81] The sensor demonstrated a high sensitivity figure of 2.81 KPa^{-1} (pressure < 0.12 KPa) with a fast response time of 42 ms.

One of the critical requirements for wearable sensors targeted for human physiological parameter monitoring is user comfort. Along with flexibility, skin conformality, and stretchability, breathability is another important feature that is highly desirable for skin-like sensors. However, most of the sensors in the literature are based on airtight films which are not breathable and hence might cause discomfort and skin inflammation in long-term use.^[99,103] Owing to their highly porous structures, nanofiber membranes offer an attractive proposition for the development of skin-conformal, stretchable, and wearable sensors for human physiological parameter monitoring. Yang et al. reported a breathable skin-printed piezocapacitive sensor featuring a TPU nanofibrous membrane dielectric layer sandwiched between two layers of PVDF AgNW membranes as shown by the schematic in Figure 8a.^[99] The SEM images in Figure 8b show the surface morphologies of the PVDF nanofiber membrane electrode with screen-printed interlaced AgNWs on the surface (left image) and the nanofibrous TPU dielectric layer (right image). The PVDF nanofiber membranes ensure good hydrophobicity with a contact angle of 110.25° . The porous nature of the electrodes and the dielectric layers allows for easy passage of air molecules rendering the sensor breathable with a Gurley value of $17.3 \text{ s}/100 \text{ mL}$. Three different sensors with TPU nanofibrous membranes (TPUNM) electrospun for 6, 4.5,

and 3 h (demarcated TPUNM1, TPUNM2, and TPUNM3, respectively) were cross-compared for pressure sensitivity. The plot in Figure 8c, shows the pressure versus relative capacitance change response of the three pressure sensors. The thinnest pressure sensor (TPUNM3) showed the highest sensitivity of 4.2 KPa^{-1} for low-pressure ($0\text{--}400 \text{ Pa}$) and 0.071 KPa^{-1} for high-pressure ($4\text{--}30 \text{ KPa}$) regimes, respectively. The authors attribute the higher sensitivity among the thinner sensor to lower density, resulting in higher relative distance change during pressure application. Accelerated lifetime assessment test for 10 000 cycles at 1.43 Hz frequency under 15 kPa pressure demonstrated the robustness and reliability of the sensor. The authors conducted human physiological parameters monitoring experiments involving respiratory and heart rate monitoring to demonstrate the applicability of the sensors. The sensor was attached to the left side of the chest (Figure 8d left) and the data from the sensor was acquired at rest and postexercise. The plot (right) of Figure 8d compares the sensor response for rest and postworkout heart rate regime demonstrating the ability of such sensors for comfortable and reliable human physiological parameters in real-time.

One of the critical drawbacks of polymeric membrane-based piezocapacitive sensors is the low dielectric constant of the dielectric layers. In the past, several researchers have explored the idea of nanomaterial filler dispersion inside polymeric dielectric materials to increase their dielectric permittivity.^[104–107] In the case of conductive nanomaterial filler–polymer composites, the dielectric constant “ ϵ ” of the nanomaterial–polymer composites follows the relation: $\epsilon \propto \epsilon_p |f - f_c|^{-s}$, where ϵ_p represents the dielectric constant of the insulating polymer matrix, s represents an exponent with value ≈ 1 , f represents the fractional volume of the nanofiller in the polymer matrix, and f_c represents the critical fractional volume at percolation threshold.^[104] Several mechanisms have been proposed to explain the phenomenon of dielectric constant enhancement in nanomaterial filler-loaded dielectrics^[105,107,108].

- Microscopic dipole formation in conductive nanomaterial–polymer composites has been explored by various researchers in the past to explain the observed dielectric constant enhancement phenomenon.^[109,110] In this case, the application of an external electric field to the nanomaterial–polymer composite leads to charge accumulation at the interface between the nanomaterial fillers and the polymer matrix subsequently leading to interfacial polarization (Maxwell–Wagner–Sillars polarization). For a piezocapacitive sensor employing a nanomaterial–polymer composite-based dielectric layer, under the application of external pressure, the existing field strength between the two electrodes increases, which leads to the intensification of interfacial polarization thereby leading to further enhancement in dielectric permittivity.^[111]
- For nanomaterial filler near the percolation threshold in a nanomaterial–polymer composite, the microcapacitor network formation theory has been invoked by several researchers to explain the giant enhancement of dielectric constant near the percolation threshold.^[19,104,108,112] When the nanofillers’ volume fraction approaches the percolation threshold (below the critical volume fraction), several microcapacitors are formed by neighboring conductive nanofillers separated by very thin layers of the polymer insulator. Each of these

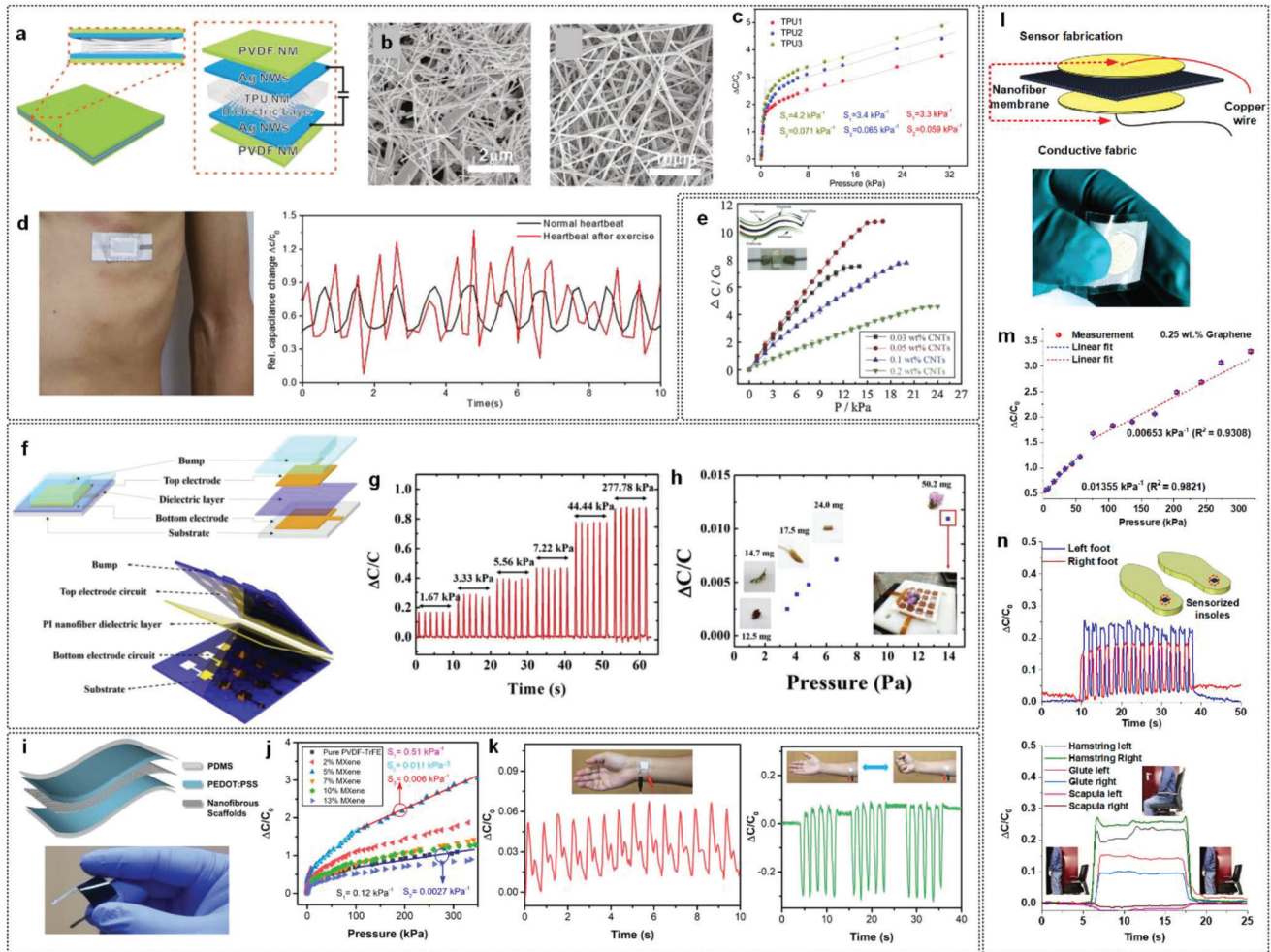


Figure 8. Nanofibrous structures based piezocapacitive wearable sensors. a) Schematic representation of the TPUNM-based breathable sensor with PVDF–AgNW electrodes. b) SEM image of interlaced AgNWs on PVDF nanofibers. SEM image of TPU nanofibrous membrane. c) Plot showing pressure versus relative capacitance change response of the three sensors. d) Photograph of the breathable sensor attached to the chest for heart rate monitoring. Plot showing sensor signals in repose to normal and postworkout heart rate.^[99] Reproduced with permission.^[99] Copyright 2018, Wiley-VCH GmbH & Co. e) Plot comparing the relative capacitance change responses of the various wt% CNT loaded PVDF-based piezocapacitive sensors. Plot in inset showing the structure and photograph of the sensor.^[111] Reproduced with permission.^[111] Copyright 2019, Elsevier B.V. f) Schematics showing the structure of PI nanofibers based piezocapacitive pressure sensor and the multisensor array. g) Plot showing dynamic pressure versus normalized capacitance change response of the electrospun polyimide nanofibrous membrane-based piezocapacitive sensor. h) Plot showing the response of the sensor under pressure from different small objects loading.^[100] Reproduced with permission.^[100] Copyright 2020, Elsevier B.V. i) Schematic representation of the process flow involved in the fabrication of the MXene–PVDF–TrFE nanofiber-based flexible piezocapacitive sensor. j) Plot comparing the relative capacitance change responses of the various wt% MXene loaded PVDF–TrFE nanofibrous membrane-based piezocapacitive sensors. k) Plot (right) showing real-time radial artery pulse wave monitoring. Plot (left) showing sensor response to left ventral muscle movement.^[19] Reproduced with permission.^[19] Copyright 2020, American Chemical Society. l) Schematic representation of the process steps involved in the fabrication of the 0.25 wt% graphene–PVAc nanofiber-based piezocapacitive sensor; Photograph of the 0.25 wt% graphene–PVAc nanofiber-based sensor. m) Plot showing the pressure versus relative capacitance change response of the 0.25 wt% graphene–PVAc nanofiber-based sensor. n) Plot showing the sensor responses from the heel regions of a healthy subject while walking with a normal gait. Plot showing the sensor responses from the bilateral hamstring, scapula, and gluteal muscle region of a test subject while being seated upright.^[102] Reproduced under the terms of the Creative Commons CC BY 4.0 license.^[102] Copyright 2023, the Authors, published by ACS.

individual microcapacitors demonstrates a very high capacitance figure and subsequently contributes to the overall enhancement of the dielectric constant of the composite.^[104,108]

Yang et al. harnessed the interfacial polarization phenomenon by employing CNT-loaded PVDF nanofibers for fabricating highly sensitive piezocapacitive pressure sensors.^[33] The pres-

sure sensor featured an electrospun CNT-PVDF nanofibrous membrane sandwiched between two layers of ITO–PET films. The addition of CNTs in the polymer not only raises the dielectric constant but also helps lower the compressive modulus thus enhancing the overall sensitivity of the resulting pressure sensors.^[19,111] Pressure sensitivity assessment experiments conducted on the sensors revealed a sensitivity figure of 0.99 kPa^{-1}

with a fast response time of 29 ms. The plot in Figure 8e cross-compares the four different pressure sensors with 0.03, 0.05, 0.1, and 0.2 wt% CNTs loading in PVDF. The sensor with 0.05 wt% CNT dispersion and 20.1 μm membrane thickness were found to have the optimal sensing performance.

One of the critical drawbacks with most of the piezocapacitive sensors is their low dynamic range. Zhu et al. employed electrospun polyimide nanofibrous membranes as the dielectric layer for the fabrication of a highly sensitive piezocapacitive pressure sensor with a wide dynamic range.^[100] The sensor demonstrated a high sensitivity of 2.204 kPa^{-1} at 3.5–4.1 Pa and a wide dynamic range (0–1.388 MPa). Furthermore, the sensor demonstrated an excellent lower detection threshold of 3.5 Pa. The plot in Figure 8g shows the dynamic pressure versus relative capacitive change response of the sensor for six distinct dynamic pressure loading (1.67, 3.33, 5.56, 7.22, 44.44, and 277.78 kPa). The lower detection threshold of the sensor was demonstrated by loading the sensor with various lightweight objects like wooden twigs, dried flower buds, etc. (plot in Figure 8h). The lower detection threshold was found to be 3.5 Pa. Furthermore, the sensor demonstrated a good linear characteristic with a sensitivity of 2.204 kPa^{-1} in the pressure range of 3.5–4.1 Pa and 0.721 kPa^{-1} in the pressure range of 4.1–13.9 Pa.

Though 1D materials like CNTs^[111] have been used for enhancing the dielectric performance of polymeric materials, their low surface area combined with the propensity to form agglomerates degrades their mechanical performance and hence negatively affects their prospects for capacitive sensing. By contrast, 2D materials like graphene (and more recently MXene) offer larger surface area, which leads to better dispersion and adhesion inside the embedding polymer matrix. MXene ($\text{Ti}_3\text{C}_2\text{T}_x$), which is a newly discovered class of 2D material comprising metal carbonitrides and carbides have drawn the interest of the materials research community owing to their excellent mechanical properties, high specific capacitance, and thermal stability. Recently, Sharma et al. reported an MXene ($\text{Ti}_3\text{C}_2\text{T}_x$)/PVDF-TrFE nanofibrous membrane-based piezocapacitive sensor for human physiological monitoring applications.^[19] The sensor featured an MXene/PVDF-TrFE nanofibrous dielectric membrane sandwiched between two layers of poly-(3,4-ethylenedioxythiophene) polystyrene sulfonate PDMS electrodes. Comparison of PVDF-TrFE nanofibrous membranes with various wt% (2, 5, 7, 10, and 13%) MXene filler dispersion demonstrated a dielectric constant enhancement in the range of 10–40. A similar trend was observed in the case of the dielectric loss tangent. The pristine PVDF-TrFE-based sensor was compared with various wt% MXene dispersed PVDF-TrFE based sensors. The plot in Figure 8j shows the pressure versus relative capacitance change response of the sensors with various nanofibrous membranes. The sensor with 5% MXene dispersion showed the maximum sensitivity figures of 0.51 kPa^{-1} for the low-pressure regime (0–1 kPa), 0.01 kPa^{-1} for medium pressure regime (10–150 kPa), and 0.006 kPa^{-1} for high-pressure regime (150–400 kPa). Furthermore, the sensor demonstrated an excellent lower detection threshold of 1.5 Pa and reliable sensing performance of 10 000 cycles of dynamic pressure loading at 167 kPa. To demonstrate the applicability of the sensor in reliable human physiological monitoring a series of tests involving heart rate detection, respiration monitoring, finger tremor detection, muscle movement, and phonation analy-

ses were conducted. The plot in Figure 8k (left) shows the pulse rate (relative capacitance change response of the sensor) acquired from the ventral side of the wrist's dermal area in response to the normal pulse rate. The zoomed-in plot (not shown here) was used to discern between the characteristics of peaks D-wave, T-wave, and P-wave of a pulse waveform. The sensitivity of the sensor allowed for easy discrimination between the characteristics peaks, which could potentially be useful for identifying arterial stiffness and abnormalities in the heartbeat rhythm. The plot in Figure 8k (right) shows the responses of the sensor to left ventral arm muscle movement.

Recently, Yu et al. reported a thin ($\approx 36\text{ }\mu\text{m}$) all-fabric piezocapacitive pressure sensor featuring a micropatterned TPU nanofiber dielectric layer sandwiched between two layers of AgNW-based electrodes.^[101] The structure of the sensor leads to a very high sensitivity of $\approx 8.31\text{ kPa}^{-1}$ for pressure $< 1\text{ kPa}$ with an excellent lower detection threshold of 0.5 Pa. Furthermore, the sensor demonstrated a wide sensing range (0.5 Pa–80 kPa) and robustness was demonstrated through cyclic loading tests involving 10 000 cycles of pressure loading at 1 kPa.

With the rapid growth in affordable consumer electronics in the last few decades coupled with the current trend of incremental yearly updates by manufacturers, outdated gadgets and devices are being disposed of every year by tech-savvy consumers leading to a pile-up of toxic electronic wastes. To circumvent the detrimental impact of non-recyclable electronics on the environment and public health, there is a pressing need for the research and development of transient electronics, which is going to play a major role in the field of wearable electronics for the foreseeable future. Recently, Sengupta et al. reported graphene–polyvinyl acetate (PVAc) nanofiber-based degradable piezocapacitive sensors for human physiological parameters monitoring.^[102,113] Similar to the work of Sharma et al.,^[19] this work fundamentally investigated the effect of 2D nanomaterial filler (graphene) addition on the dielectric constant of PVAc polymer. The sensor reported in the work featured a nanofibrous membrane sandwiched between two layers of circular silver-plated nylon fabric electrodes and optically clear adhesive plate seals for complete encapsulation as shown schematically in Figure 8l. The 0.25 wt% graphene-loaded PVAc nanofiber-based sensor showed the highest sensitivity figures of 0.014 kPa^{-1} for the low-pressure regime (2.7–44 kPa) and 0.006 kPa^{-1} for the high-pressure regime (56–319 kPa). The plot in Figure 8m shows the pressure versus relative capacitance change response of the aforementioned sensor. The sensor assembly was subjected to a series of cyclic compressive loading and the hysteresis values were found to be $\approx 4.31\%$, 4.93% , 3.62% , 3.62% , and 2.85% for $\approx 5\%$, 10% , 20% , 30% , and 40% compressive strains, respectively. Furthermore, to demonstrate the robustness and reliability of the sensor, a series of accelerated lifetime assessment tests entailing a total of 3000 cycles of tactile force loadings (at 2.7, 10, and 20 N) were presented. The applicability of the sensor for human physiological parameter monitoring was demonstrated by a series of experiments involving muscle movement detection, finger tremor, and respiratory rate monitoring. In particular, the suitability of the sensor for IoT-enabled activity monitoring was underscored by demonstrating a sensorized shoe insole capable of gait detection. The plot in Figure 8n (top) shows the responses acquired from the heel regions of two sensorized insoles while a person walked in a

straight line. Secondary data such as cadence and walking speed were shown to be derived from the primary gait data. Finally, an ergonomic smart chair comprising of an office chair affixed with six pressure sensors on the bilateral scapula, hamstrings, and gluteal muscle regions was demonstrated. The plot in Figure 8n (bottom) shows the change in responses of the sensors while a standing subject sat down upright before rising again.

4.2. Nanofiller–Polymer Composite-Based Planar Sensors

4.2.1. 1D Nanomaterials–Polymer Composite-Based Planar Sensors

Other than intrinsically conductive polymers like poly(pyrrrole) (PPY), poly(3,4-ethylenedioxythiophene), polyanilines, etc., most polymers are insulators. Elastomeric materials like PDMS, PI, and PU are electrically nonconductive. However, elastomers and thermoplastics have been exploited by the sensors community for the past few decades due to their excellent mechanical properties, responsiveness to torsion, and elasticity. Nonconducting polymers can be made conductive to charge carriers by dispersing conductive nanomaterial fillers. In the past, a variety of nanomaterials like metallic nanoparticles, AgNWs, SW/MWCNTs, graphene, and more recently MXene has been dispersed in polymer matrix to form conducting composites.^[38,55,114–117]

For conductive nanomaterial fillers dispersed in a polymer matrix, near the percolation threshold, the charge carriers (electrons) can travel through overlapping nanomaterials percolation network.^[48] Particularly in the case of conductive nanomaterial elastomer composites, stretching/stress causes disconnection between the adjacent conductive fillers, which can be attributed to material slippage caused by stiffness mismatch between the filler and polymer matrix. Furthermore, any external stress/pressure causes a change in the overlap area between two adjacent conductive fillers leading to a change in conduction path/resistance. Additionally, this piezoresistive behavior in the elastic regime can also be explained by Simmon's tunneling theory.^[57] Recently, the conductive domain disconnection mechanism has been exploited extensively to develop flexible, stretchable, and wearable piezoresistive strain/pressure sensors.^[48] For instance, though CNTs demonstrate intrinsic piezoresistivity, in the case of CNT–elastomer composites, under any external stress/pressure the conductive domain disconnection mechanism dominates more than the intrinsic piezoresistivity of CNTs.^[118] Employing the concept of conductive domain disconnection mechanism or nanoscale crack junctions, several flexible sensors have achieved exceptionally high sensitivity/piezoresistive gauge factors.^[9]

In one of the earlier works, Wichmann et al. cross-compared the piezoresistive effect in carbon black (0D material) and CNTs (1D material) epoxy composite for sensing in elastic and inelastic regimes.^[119] A matrix system of Araldite LY556 epoxy, Aradur 917 anhydride hardener, and D070 accelerator was dispersed separately with 0.5 wt% of CB and 0.1, 0.3 wt% of MWCNTs, respectively. Electrical field versus conductivity analysis tests revealed a quasi-ohmic behavior at low field strength and a weak deviation (from ohmic behavior) for higher field strength, which was attributed to non-ohmic behavior found in such composites near percolation threshold.^[119] From the electromechanical

and piezoresistive behavior assessment experiments, the authors concluded that the piezoresistive behavior was dependent both on the type of filler and the content. A linear strain versus resistance change response was observed for the CNTs-based composites in the elastic regime whereas the CB-based composites demonstrated an exponential behavior. While both the fillers behave similarly for lower strain regimes, particle geometry might play a significant role for higher strain regimes which can be attributed to the effects of inelastic matrix deformation, which influence the conductive network. The authors concluded that the CNTs-based composites provided superior sensing characteristics in terms of linearity.^[119]

Though the dispersion of nanomaterial fillers in a polymer matrix improves electrical conductance, not much focus is placed on the alignment of the nanomaterials inside a polymer matrix. In the past, Lanticse et al. reported that at lower concentrations of CNT fillers in a polymer matrix, preferential alignment of the nanotubes led to significantly higher conductivity (up to 10^6 times) in the direction of alignment compared to that of the composite with randomly oriented ones.^[122] Oliva-Avile's et al. reported alignment of MWCNTs (varying weight percentages of 0.1, 0.3, 0.5, and 0.75 wt%) in polysulfone (a thermoplastic polymer) matrix employing alternating field with field strength lying in the range of 6.0–7.3 kV m⁻¹.^[123] Strain versus normalized resistance change response assessments of the different samples demonstrated linear resistance change response in the field-aligned samples for the elastic regime (strain < 1.5%). The 0.5 wt% MWCNT-loaded field aligned sample showed the highest gauge factor of 2.78. The authors explained the gauge factor enhancement in the field-aligned samples drawing conclusions from Theodosio and Saravanos' work involving multiscale modeling.^[124] Theodosio and Saravanos predicted a strong correlation between the piezoresistive sensitivity and the CNTs alignment with the largest sensitivity observed along the axis of CNTs alignment.^[124] Rizvi et al. explored the piezoresistive behavior of CNT PDMS and CNT polyethylene (PE) composites near the percolation threshold.^[125] Different wt% of MWCNTs (1, 2, 3, 4, and 6 wt%) were dispersed in PDMS and PE and composites were prepared by direct mixing and melt compounding for PDMS and PE, respectively. Dielectric spectroscopy assessments revealed MWCNTs percolation threshold of 3% (volume fraction ≈ 0.0154) and 2.2% (volume fraction ≈ 0.0103) for PDMS and PE, respectively. The conductivity of MWCNTs–PDMS composites was found to be higher than its PE counterpart. However, the authors observed that PE composites demonstrated higher piezoresistive sensitivity in comparison to PDMS-based composites. Furthermore, PDMS-based composites demonstrated higher sensitivity with increasing filler content whereas the PE-based composites demonstrated lower sensitivity with increasing filler volume. The author attributed this discrepancy in sensitivity to nanofiller dispersion in the polymer matrices. The MWCNTs formed aggregates in PDMS matrices whereas the PE-based composites were found to be mostly free of large aggregates which reduces the interparticle distance between the MWCNT fillers.^[125]

Though CNTs as 1D materials have dominated 1D nanomaterial–polymer composite-based flexible sensors, AgNW offers an attractive alternative to CNTs owing to their excellent conductivity and mechanical properties. AgNWs have found applications in transparent electrodes, thin film technology, and

solar cells. Amjadi et al. reported AgNWs PDMS composite-based stretchable and flexible sensors for wearable electronics applications.^[18] The sensor featured an AgNWs percolation network film sandwiched between two layers of PDMS. The encapsulation step with PDMS causes the PDMS prepolymer to infiltrate the porous structure of the AgNWs percolation network leading to a 3D network of AgNWs embedded in the PDMS elastomer matrix as shown by the SEM image in **Figure 9a** (left). The SEM image in **Figure 9a** (right) shows the cross-sectional view of the AgNWs–PDMS sandwich structure. The high stiffness mismatch between AgNWs and PDMS leads to nanowire sliding leading to overall resistive path change, which is reflected in the observed strain-induced resistance change behavior. The sandwich composite structure enables the AgNWs to track back their original path when released from a strained position thus leading to excellent recoverability and low hysteresis.^[18] The plot in **Figure 9b** (left) shows the I – V characteristics of the sensor for 0%, 20%, 40%, and 60% strains. The sensors demonstrated an ohmic behavior as observed from the plot. As explained previously, in the case of conductive nanomaterial–polymer composites disconnection of nanomaterial fillers for higher strain levels causes increased resistance. The plot in **Figure 9b** (right) shows the strain versus relative resistance change response of sensors with different concentrations of AgNWs. It was concluded that the gauge factor and initial resistance of the sensor could be “tuned” by controlling the concentration of AgNWs dispersion during the deposition step. The sensors demonstrated a tunable piezoresistive behavior with gauge factor lying in the range of 2–14 with strains up to 70%. The authors concluded that the sensors with high initial resistance are suitable for low-strain applications requiring high sensitivity whereas the sensors with low initial resistances are better suited to applications demanding high strain levels with an acceptable sensitivity.^[18] The authors demonstrated the application of the sensor in a smart glove for finger movement monitoring.

Though most of the nanomaterial–polymer composite-based piezoresistive sensors are able to respond to normal and uniaxial stress, multidirectional and shear force sensing are two critical requirements for true skin-inspired sensors. There are several examples of hierarchical structures in nature which include Gecko’s feet, the lizard’s tail, etc. For instance, epidermal–dermal ridge structures in human skin (**Figure 9c** top-left) are known to enhance tactile perception. The ridge structures facilitate better adhesion between the dermal and epidermal layers and are also responsible for the magnification and transduction of tactile stimuli from the skin surface to mechanoreceptors lying in the dermal region. Taking inspiration from dermal–epidermal interlocked structures of human skin, Park et al. developed an MWCNT–PDMS composite-based piezoresistive sensor featuring two layers of interlocking hexagonal microdomes on PDMS surface (**Figure 9c** top-right).^[120] The interlocking structures enabled directional sensitivity and demonstrated different sensory output patterns for normal loading, stretching, bending, and shear force.

Ha et al. built up on their previous work on the piezoresistive interlocking domes and developed a hybrid piezoelectric and piezoresistive ultrasensitive and fast response sensor featuring interlocking PDMS micropillars decorated with ZnO nanowire arrays.^[121] The schematic in **Figure 9d** (top) shows the sensor fea-

turing two interlocking layers of PDMS with ZnO NW decorated micropillars. Under the application of external pressure, the contact areas between the interlocked NWs change thereby leading to the change in resistance. The SEM image in **Figure 9e** shows the interlocking geometry of the ZnO NW arrays on the top and bottom micropillars. The sensitivity of the sensor could be tuned by controlling the pitch size of the ZnO NW arrays. The plot in **Figure 9e** compares the pressure versus normalized resistance change responses of the planar NW arrays (without hierarchical structures) with the hierarchical NW arrays with varying pitch sizes. Resistance values decreased rapidly with increasing normal pressure up to 2 kPa followed by a slower decrease post 2 kPa regime. The sensor with a 20 μm pitch size showed a pressure sensitivity of -6.8 kPa^{-1} which is 3.7 times more sensitive than the planar sensor for pressures less than 0.3 kPa. Furthermore, the sensor overcame the viscoelastic behavior related slow response time observed in most polymer-based sensors due to the rigid crystalline ZnO NWs, which do not demonstrate viscoelastic deformation. The sensors demonstrated fast response times of 5 and 0.2 ms for the ones with hierarchical structures and planar ones, respectively. The dynamic pressure sensing capability of the skin enabled by the Pacinian corpuscles was mimicked by the sensor using piezoelectric sensing mode. The hexagonal ZnO NW arrays show spontaneous polarization along the C -axis crystal direction. For piezoelectric sensing mode, the top layer of ZnO NW arrays was coated with a 300 nm thick layer of Ni, which enables the formation of a Schottky barrier between the metal-coated ZnO NWs and the bare semiconducting NW arrays.^[121] Like in the case of piezoresistive sensing mode, the hierarchical structures show an enhanced power output of 5.9 mW m^{-2} , which is 11 times higher than the planar counterpart. The sensors were able to detect dynamic pressure stimuli up to 250 Hz.

Kang et al. derived inspiration from the crack-shaped slit organs (near leg joints) found in spiders which help them detect the minutest of vibrations (shown schematically in **Figure 9g**).^[9] The authors reported a highly sensitive biomimetic sensor featuring a 20 nm thick platinum layer on top of a viscoelastic polyurethane acrylate (PUA) sponge with slits/cracks generated in a controlled fashion by mechanically bending the Pt-deposited sponges at various radii of curvatures (1, 2, and 3 mm). **Figure 9h** shows an optical photograph of the cracked Pt on PUA with a lateral dimension of 5 mm \times 10 mm. The zoomed-in SEM image in **Figure 9h** (middle) shows the cracks formed in the transverse direction in response to 1 mm bending curvature. **Figure 9i** shows the finite element method simulation of stretching-induced widening of a 50 nm deep crack. The strain resistance change response characteristic was obtained by bending the sensor at a radius of curvature of 1 mm ($\approx 2\%$ strain) and unloading back to 0% strain at a sweeping speed of 1 mm min^{-1} . The mechanism of strain sensing was explained by a jump of resistance from a finite value when the crack edges touch/overlap to almost zero conductance when the edges lose contact.^[9] The sensor demonstrated an impressive gauge factor value of ≈ 2000 in the strain range of 0–2%. The sensor was applied for several human physiological monitoring experiments involving phonation analysis and pulse rate monitoring.

Most of the nanomaterial–polymer composites discussed so far relied on thermoplastic or elastomeric polymer substrates, which pose serious challenges for recyclability and

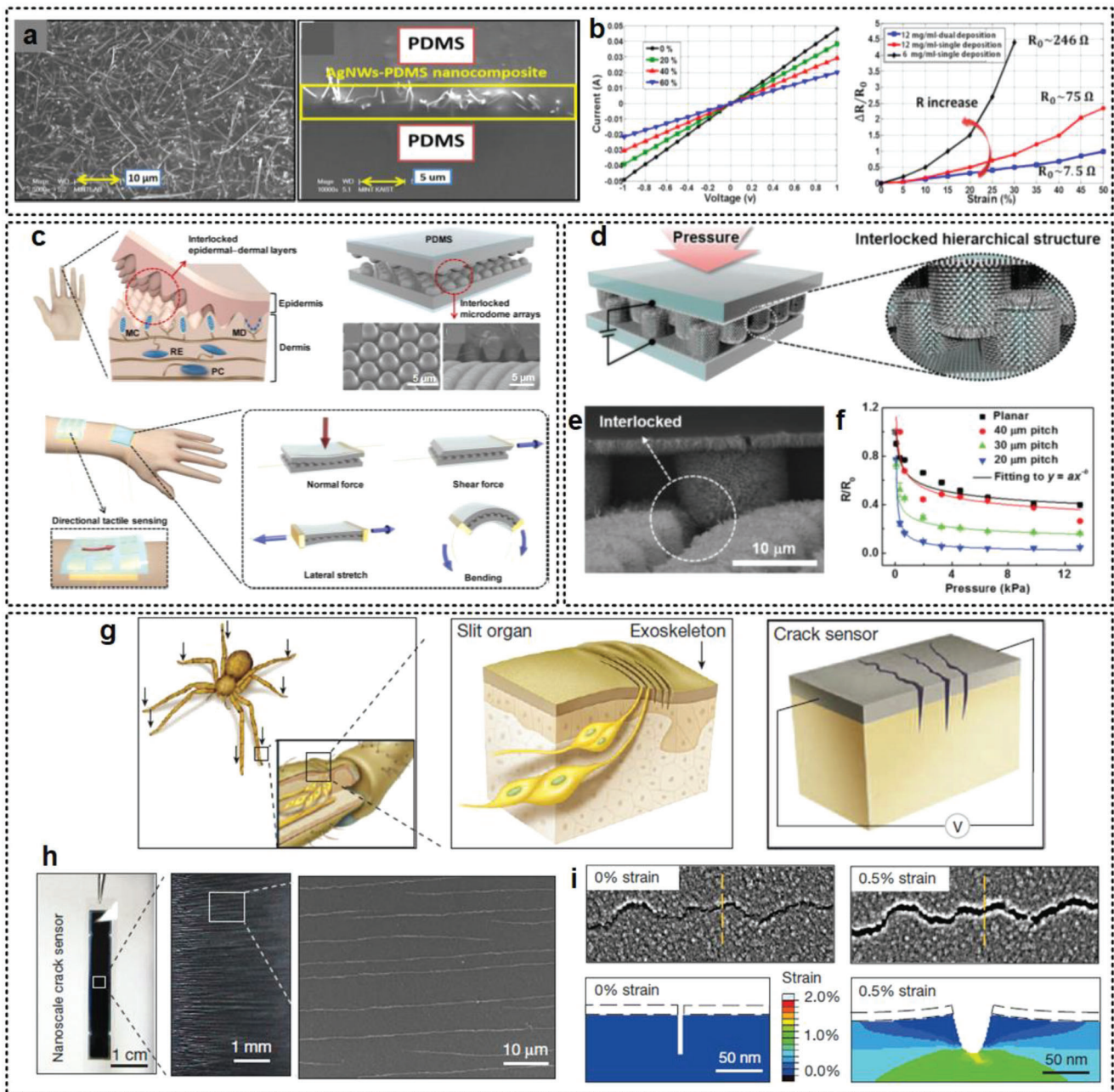


Figure 9. 1D materials–polymer composite based bioinspired flexible sensors. a) SEM image of interlaced AgNWs percolation network embedded in PDMS matrix. SEM image of the cross-section of AgNW layer sandwiched between two layers of PDMS. b) *IV* characteristics of the AgNW PDMS sensor for different strains. Strain versus relative resistance change response of the sensor.^[18] Reproduced with permission.^[18] Copyright 2014, American Chemical Society. c) Epidermal–dermal ridge-inspired interlocked microstructures-based piezoresistive sensor.^[120] Reproduced with permission.^[120] Copyright 2014, American Chemical Society. d) Schematic representation of interlocking hierarchical ZnO NW array-based piezoresistive sensor. e) SEM image of ZnO NW array on PDMS micropillars. f) Plot comparing normal pressure versus normalized resistance change response of the sensors with different pitch sizes.^[121] Reproduced with permission.^[121] Copyright 2015, Wiley-VCH GmbH & Co. g) Schematic showing sensory slit organs found in spider's leg joints, zoomed-in schematic showing anatomy of the slit organ, and schematic showing crack-based sensor. h) Image of the spider sensory crack-inspired sensor. Enlarged image of the cracks on the sensor surface. SEM image of the boxed region shown in the enlarged optical image. i) SEM images and corresponding finite element method simulation plots of the nano crack junctions at 0 and 0.5% strains, respectively.^[9] Reproduced with permission.^[9] Copyright 2014, Macmillan Publishers Limited.

biodegradability. As the manufacturing processes and consumer goods industry accelerate toward a circular economy, alternative biodegradable and greener substrate options must be explored on an urgent basis. Due to its versatility, cost-effectiveness, and biodegradability, paper is fast emerging as an interesting choice as a passive substrate material. Li et al. reported a superhydrophobic self-cleaning paper-based strain sensor for human motion monitoring applications.^[114] The sensing element featured a printing paper dip-coated with carbon black (CB)/CNT/methyl cellulose (MC) suspension. The hybrid nature of the dispersion entailing CB and CNT with MC dispersant helps in improving dispersibility and subsequently reducing the percolation threshold.^[114] The two critical problems with paper-based sensors, namely, hygroexpansion and subsequent degradation post water absorption were addressed by coating the sensing element with hydrophobic fumed silica (Hf-SiO_2), which improves the water contact angle to 154° leading to superhydrophobic properties. The stiffness and thermal expansion coefficient mismatch caused several microcracks on the surface of the CB/CNT coating. The crack propagation under external strain causes an overall change in resistance as seen previously in the case of the spider slit organ-inspired sensor reported by Kang et al.^[9] The compressive and tensile gauge factors were determined as 2.6 and 7.5, respectively, in the strain range of 0–0.7% strain. The sensor demonstrated a lower detection threshold of 0.1%. A myriad of human physiological parameters monitoring experiments involving pulse rate detection and joint movement monitoring were conducted to demonstrate the applicability of the sensor.

4.2.2. Graphene–Polymer Composite-Based Planar Sensors

Since its discovery in 2004, graphene has been one of the most sought-after and highly researched materials. Highly desirable characteristics of graphene such as crystalline quality, resilience to high current density, and high carrier mobility) qualifies it as the wonder material of the 21st century.^[72] Though monolayer graphene has been shown to demonstrate intrinsic piezoresistive properties, its stiffness coupled with the constraints related to handling and limited strain handling ability make monolayer graphene sheets unsuitable for stretchable and flexible electronics applications demanding strain levels often exceeding 100%. Like in the case of 0D and 1D materials (such as carbon black, CNTs, AgNWs, etc.) which must be embedded in polymeric substrates to render them usable for practical real-life applications involving human physiological parameters monitoring or soft robotics, graphene also needs to be embedded in suitable elastomer or thermoplastic material for their practical real-life applications. Since the demonstration of intrinsic piezoresistivity in graphene in the late 2000s,^[71] several research pertaining to using the percolation network of graphene in polymer matrices have been reported for wearable and soft electronics.^[55,126–131]

Weak interlayer adhesion of graphene sheets allows for their easy isolation, which can be exploited to deposit atomically thin films using inexpensive deposition techniques such as spray deposition. In their pioneering work, Hempel et al. reported a 2D graphene percolation network thin film-based strain gauge for the first time.^[55] The strain gauge entailed an ultrathin layer of spray-coated graphene dispersion (in 1-methylpyrrolidone) on

top of a flexible plastic substrate (PET film) with a thickness of $\approx 160 \mu\text{m}$ (fabrication schematically shown in **Figure 10a**). The initial starting resistance could be tuned by controlling the deposition volume and the authors noted an inverse power law dependence between the starting resistance and spray solution volume, which agreed with the existing understanding of percolation systems.^[55,132] To understand the effect of starting resistance on sensitivity, several sensors with different starting resistances were assessed for strain versus normalized resistance behavior and gauge factors were extracted from the slopes of the plots. The plot (right) in **Figure 10a** shows the log–log plot of initial resistance versus the extracted gauge factors, which points toward a power law dependence between the starting resistance and the corresponding gauge factor.^[55] As discussed previously, the conductive domain disconnection mechanism observed in conductive percolation networks was invoked to explain the strain-induced resistance change mechanism. The authors conducted a percolation network simulation involving a distribution of overlapping graphene nanoflakes to understand the strain-induced overlap area change leading to the overall change in resistance. The resistance of the percolation network was calculated by using Kirchhoff equations for a large network of resistors comprising flake resistance and interflake contact resistance. The color plot in **Figure 10b** shows the voltage drops across the simulated percolation network for different strains at a fixed current. The authors concluded that gauge factors could be effectively tuned by controlling the initial deposition parameters (spray volume in this case) and thus allow for a healthy compromise between sensitivity and noise to produce accurate low-noise sensors.^[55]

Yan et al. demonstrated an innovative method of fabricating a stretchable graphene–nanocellulose nanopaper for human motion monitoring applications.^[126] The work featured the synthesis of flexible nanopapers from nanocellulose and crumpled graphene (weight ratio 1:1) and subsequent infiltration with PDMS elastomer leading to stretchable nanopapers. **Figure 10c** shows a schematic representation of the process steps involved in the fabrication of the stretchable graphene nanopapers. The flexible graphene nanopaper without PDMS infiltration (light blue symbols in **Figure 10d** left) can only be stretched up to 6% and breaks upon further straining. The nanoporous structure of the nanopaper facilitates its successful embedment in PDMS elastomer, which allows it to bear strains up to 100% without mechanical failure.^[126] For comparison, AgNW- and CNT-based sensors were also fabricated and assessed for strain-sensing performances. As observed from the plot in **Figure 10d** (left), the stretchable graphene nanopaper shows significantly larger strain versus normalized resistance change behavior in comparison to CNT- and AgNW-based sensors. The plot in **Figure 10d** (right) shows the gauge factor of the four types of sensors (flexible nanopaper, stretchable nanopaper, AgNW, and CNT) as a function of strain. The gauge factor of the stretchable graphene paper lies in the range of 1.6–7.1 (strain range ≈ 10 –100%). Five identical stretchable sensors were assembled on a feather glove to demonstrate the application of the sensors for practical human motion monitoring. Each of the five fingers was bent (strain ≈ 35 –45%) at a frequency of 1 Hz and the sensor responses were registered as shown by the plot in **Figure 10e**.

To develop a highly stretchable and sensitive sensor capable of bearing giant strains ($\epsilon > 800\%$) Boland et al. proposed a facile

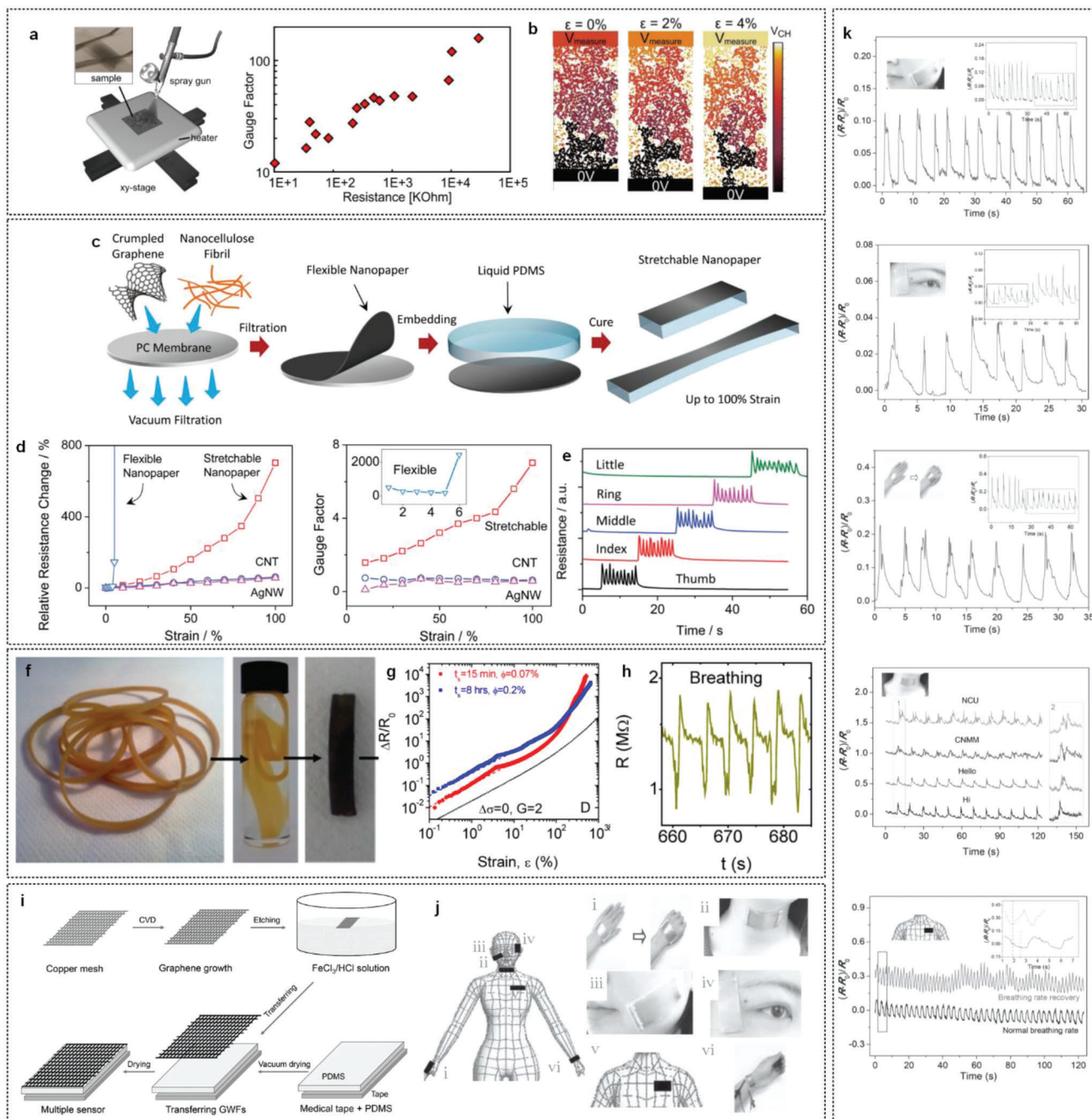


Figure 10. Graphene–polymer composite-based flexible sensors for human physiological parameters monitoring. a) Schematic representation of the spray deposition approach to fabricate the graphene percolation network thin film-based strain gauge. Plot showing the dependence of extracted gauge factor on initial resistance. b) Simulation showing the voltage drop across the graphene 2D percolation network for different levels of strains.^[55] Reproduced with permission.^[55] Copyright 2012, American Chemical Society. c) Schematic representation of process steps involved in the fabrication of stretchable graphene nanpaper. d) Plots showing the strain versus relative resistance change and strain versus extracted gauge factors for the different sensors, respectively. e) Plot showing the responses of the sensors to periodic finger movement at 1 Hz frequency.^[126] Reproduced with permission.^[126] Copyright 2013, Wiley-VCH GmbH & Co. f) Photographs showing the elastic bands, subsequent soaking in toluene and final graphene rubber composite after soaking (in NMP:water:graphene mixture) and drying. g) Plot comparing strain versus normalized resistance change response of a strain sensor relying solely on geometrical change. The dashed line showing the strain-normalized resistance change response of a strain sensor relying solely on geometrical change. h) Response of the sensor to slow breathing.^[127] Reproduced with permission.^[127] Copyright 2014, American Chemical Society. i) Schematic representation of the process steps in the fabrication of GWFs-PDMS-tape sensor. j) Representing various positions where the GWFs-PDMS-tape sensor could be used for physiological parameters monitoring. k) Responses acquired from the sensors during facial expression changes, ocular muscle movement, fist kinesthetics, phonation, and respiratory rate monitoring, respectively.^[128] Reproduced with permission.^[128] Copyright 2014, Wiley-VCH GmbH & Co.

method of developing a graphene–natural rubber composite-based strain sensor capable of fast sensing, working well at vibrational frequencies exceeding 160 Hz.^[127] The work featured a novel two-step process entailing the swelling of store-bought rubber bands in toluene solution followed by submerging of the swollen bands in graphene dispersion in *N*-methyl-pyrrolidone (NMP) for varying duration in the range ≈ 15 min–48 h. The photographs in Figure 10f show the rubber bands at different stages during the fabrication process. The volume fraction of graphene (in rubber) was calculated for the different soak times with a volume fraction of 0.55% achieved after 48 h of submergence. The composite bands were tested for mechanical failure and the bands were found to bear strains in the range of 500–1100%. The plot in Figure 10g compares the strain versus normalized resistance change response of the two different bands (soak times of 15 min and 8 h). The plot also compares the sensor response with a hypothetical strain gauge with strain-independent conductivity relying solely on geometry-induced resistance to change with a gauge factor of 2 (dashed line). The authors reported that the gauge factor of the strain sensors decreased with increasing volume fraction with a maximum gauge factor of 35 observed in the case of graphene–rubber band composite with 0.2% volume fraction of graphene, which was closer to the bulk percolation threshold of 0.12%.^[127] The composite strain sensors were utilized for kinesthetic sensing, phonation analysis, and other physiological parameters (namely, pulse and respiratory rate) detection to demonstrate their applicability in real-life human motion monitoring. The plot in Figure 10h shows the resistance change response of the sensor to a slow breathing pattern.

As one of the chief motivations behind materials innovation for flexible electronics lies in their potential applications in human physiological parameters monitoring, work focusing on applications of such sensors for a myriad of vital physiological parameters is desirable. Wang et al. reported an inexpensive graphene woven fabrics (GWFs) based wearable sensor tailored for physiological parameter monitoring.^[128] The process steps for fabrication of the GWFs entailed atmospheric pressure chemical vapor deposition grown graphene on copper meshes and subsequent etching of the meshes in FeCl_3/HCl solution followed by transfer of the graphene meshes on pretreated PDMS-Medical tape substrate (schematically represented in Figure 10i). The strain-induced resistance mechanism was explained by the formation of several cracks in the GWFs network upon application of any stress leading to overall resistance change.^[128] The authors reported gauge factors of $\approx 10^3$ in the strain range of 2–6% and 10^6 for strains exceeding 7%. The sensors were sensitive enough to detect low strains under 0.2% with a gauge factor of 35. The schematic in Figure 10j shows the potential applications of the sensors for physiological parameter monitoring. A series of comprehensive tests to demonstrate the performance of the sensors in human physiological parameters monitoring were conducted. Tests involving fist kinesthetics, phonation detection, facial movement during microexpressions, ocular muscle movement during blinking, and respiratory and pulse rate monitoring were demonstrated. The plots in Figure 10h shows the acquired responses of the sensors from facial expression changes, ocular muscle movement, fist kinesthetics, phonation, and respiratory rate monitoring, respectively.

Niu et al. reported a graphene–PDMS planar sensor based on a two-step mechanical mixing process.^[129] Four different concentrations (2, 3.5, 5, and 8 wt%) of graphene in PDMS were fabricated and assessed for strain and pressure sensitivities. Strain versus normalized resistance change characteristics revealed the 5 wt% (graphene in PDMS) sensor to be the most sensitive, which could be explained in light of the existing percolation network theory. Similar behavior was observed in the case of force sensitivity.

Thermoplastic elastomers combine the desirable mechanical properties of rubber-like materials with the facile processability and chemical stability of high-performance thermoplastics.^[133] Though most of the work reported in literature makes use of materials like PDMS/ecoflex, TPU, and PI, styrene–butadiene–styrene, and its more biocompatible copolymer polystyrene–ethylene–butylene–styrene (SEBS) are a class of high deformation thermoplastic elastomers and can potentially serve as attractive alternatives due their highly desirable properties like chemical and thermal stability, facile processability, and UV radiation resistance.^[130] Costa et al. reported SEBS graphene nanostructure composites for fabricating high-performance piezoresistive sensors for wearables applications.^[130] Different kinds of graphene fillers such as graphene oxide (GO), reduced graphene oxide (rGO), and graphene nanoplatelets were utilized for developing graphene–reinforced SEBS composites. Low percolation thresholds of 2% were observed in the case of the GO and rGO-based composites with a maximum strain-bearing capability of 800% uniaxial strain. Piezoresistive gauge factors in the range of 15–120 ($\epsilon < 10\%$) were observed for rGO/GO–SEBS composites. Four identical rGO/SEBS-based strain sensors were secured on a hand glove and demonstrated for finger kinesthetics underscoring the applicability of the sensors for wearables applications.

4.2.3. Nanofiller–Hydrogel Composites-Based Planar Sensors

For the past few decades, flexible electronics research has been heavily centered on thermoplastics and elastomers such as PDMS, TPU, etc., which can be attributed to their ease of processability and inexpensive nature. Typically, these materials in bulk form exhibit relatively high elastic modulus (typically in the range of 500 kPa–1 GPa) in comparison to human skin (Young's modulus in the range of 4.5–8 kPa)^[134] and soft tissues (modulus up to ≈ 1 MPa).^[135] This apparent mechanical mismatch can cause poor conformability, tissue trauma, and foreign body reaction in addition to the obvious problems of bio-incompatibility.^[136] To combat the bottlenecks associated with common engineering polymeric materials, biodegradable hydrogels are fast emerging as promising alternatives owing to their bioinspired 3D structure, moisturizing ability, high surface area, and tunable conductivity (in the case of ionic hydrogels).^[136]

Though at first glance, hydrogel might almost seem like a wonder polymer existing to solve most of the problems faced in the flexible electronics community, there are critical issues such as low sensitivity, poor adhesion, fragile nature, prone to dehydration and subsequent mechanical degradation which prohibit their use for mainstream wearable electronics. Furthermore, such hydrogel matrices must have stable electroconductive networks to be useful for piezoresistive sensing in human motion

monitoring applications. Fortunately, most of the existing issues related to poor electrical and mechanical performance can be addressed by the incorporation of functional nanomaterial fillers in hydrogel matrices. As seen previously, the issue of poor electrical conductivity can possibly be mitigated by the addition of conductive nanofillers. However, poor dispersion characteristics of the common metallic nanoparticles and carbon-based nanomaterials in the aqueous suspension of the hydrogels and subsequent agglomeration adversely affect the formation of the gel network.^[137] The issue of poor dispersion has been tackled by employing nanocellulose as a scaffold to disperse the nanomaterial fillers in the hydrogel network effectively thereby achieving homogeneity and mechanical reinforcement.^[141,142] Bio-based nanostructured additives have gained prominence in the research field pertaining to hydrogel formulations targeted for food packaging, biomedical, and human motion monitoring applications.^[137,143,144]

In a recent work, Fraser et al. reported a polypyrrole/bacterial nanocellulose composite and sodium alginate incorporated PVA-based biocomposite hydrogels-based piezoresistive strain sensors for human motion monitoring applications.^[137] The work reported the synthesis of freeze/thaw method-based PVA hydrogels loaded with varying concentrations of sodium alginate (0, 0.2, and 1.0% w/v) and nanocellulose (0, 0.1, and 1.0% w/v). **Figure 11a** schematically represents the process steps involved in the synthesis of the PVA biocomposite hydrogels via the freeze/thaw method. A series of mechanical characterization experiments were conducted to determine the optimal number of freeze/thaw cycles, sodium alginate, and nanocellulose concentrations leading to an optimized hydrogel with an elastic modulus of 2.4 MPa, stretchability of 384%, and a high yield strength of 6 MPa. In order to improve the electroconductivity of the optimized hydrogel, polypyrrole/bacterial nanocellulose composite (prepared by in situ oxidative polymerization) was incorporated in the hydrogel matrix by blending with the PVA sodium alginate polymer melt before gelation. The synthesized conductive hydrogel demonstrated excellent toughness with remarkable resistance to fracture (under compression, stretching, and knotting) as shown by the photographs in **Figure 11b**. The authors also assumed the mechanical reinforcement contribution of polypyrrole–bacterial nanocellulose composite toward the hydrogel thereby rendering it with additional toughness. The conductive hydrogel was assessed for strain versus relative resistance change response at a uniaxial strain rate of 2.5 mm s⁻¹ (in the strain range ≈0–200%). The plot in **Figure 11c** (left) shows the relative resistance change versus strain behavior of the sensor. The authors invoked the conductive domain discontinuity mechanism in the polypyrrole–bacterial nanocellulose composite network, geometrical resistance change, and the intrinsic piezoresistivity of the polypyrrole to explain the observed piezoresistive behavior. The plot in **Figure 11c** (right) shows the gauge factor of the hydrogel as a function of strain. The hydrogel demonstrated a modest maximum gauge factor of 0.96 at 23% strain. A simple sensor was fabricated by attaching a pair of copper electrodes on the extreme longitudinal ends of the conductive hydrogel and subsequent encapsulation by sandwiching between two layers of commercial elastomeric tapes. To demonstrate its applicability in sensing human motion parameters, a series of experiments involving finger, wrist, and elbow proprioception and insole gait monitoring were conducted. The results from the tests underscored the usability

of the sensors in wearable electronics applications and also established the feasibility and relevance of “green” synthesis protocols toward developing cost-effective and environmentally sustainable wearable sensing solutions.^[137]

Ionic conductive hydrogels (ICH) with their internal ion transport channels have emerged to be excellent candidates for skin-inspired wearable sensors owing to their ability to combine softness of human tissues with the conductivity of common electronic conductors. Recently, Yao et al. reported phenylboronic acid-ionic liquid (PBA-IL) monomer and its subsequent application in preparing ionic conductive hydrogels.^[145] The work proposed a simple one-step approach wherein cellulose nanofibrils are introduced into a PBA-IL/acrylamide (AM) cross-linked network to synthesize a polyacrylamide/PBA-IL/CNF semi-interpenetrating polymer network with superior mechanical properties and self-healability.^[145] The piezoresistive sensing performance of the ICH was assessed by subjecting it to tensile strain versus relative resistance change response assessments. The strain versus relative resistance change response of the ICH demonstrated two linear regimes with gauge factors of 3.41 in the strain range 0–300% and 8.36 in the strain range (300–1000%). The ICH-based sensor was subjected to a series of human motion monitoring experiments involving finger and wrist bending, elbow and knee flexion, phonation detection, and pulse detection to underscore its suitability for wearable electronics.

Recently, MXene, which is a class of 2D transition metal carbides/nitrides/carbonitrides, has gained popularity for its large specific surface area, and superior electrical and mechanical performances. The interest in MXene–hydrogel composites has grown exponentially since its discovery in 2011. MXene–hydrogel-based self-healable sensors with super stretchability, high resilience, and biodegradability have been demonstrated.^[138,139] In the last five years, considerable progress has been achieved in the research and development of MXene–hydrogel composites-based piezoresistive and capacitive wearable sensors for human physiological parameters monitoring.^[138–140,146,147]

In an interesting article, Alireza et al. reported a facile fabrication of fluorescent carbon dots (in honey)/delaminated fluorescent titanium carbide nanosheets and 3D cross-linked polymeric chitosan network-based composite for biomedical applications. The authors argued that the combination of honey in the matrix would potentially lead to accelerated wound healing, and antibacterial and anti-inflammatory properties for potential applications in injectable regenerative medicine.^[148]

As discussed previously, capacitive/piezocapacitive sensors are preferred for applications in skin-inspired wearables because of their linearity, fast response, low hysteresis, and ultralow power budget. Electrode materials can be considered as a limiting component toward achieving a true skin-inspired stretchable capacitive sensor as most of the capacitive sensors in literature are limited by their nonstretchable metallic/semiconducting electrode material for application in wearables. Recently, a myriad of innovative materials such as conductive textiles, nanomaterial–polymer composites, and metamaterial electrodes have been proposed to solve the limited stretchability commonly encountered with traditional metallic electrodes. However, most of these textile or nanomaterial/polymer composites-based electrodes suffer from a lack of self-healing ability and limited stretchability. To

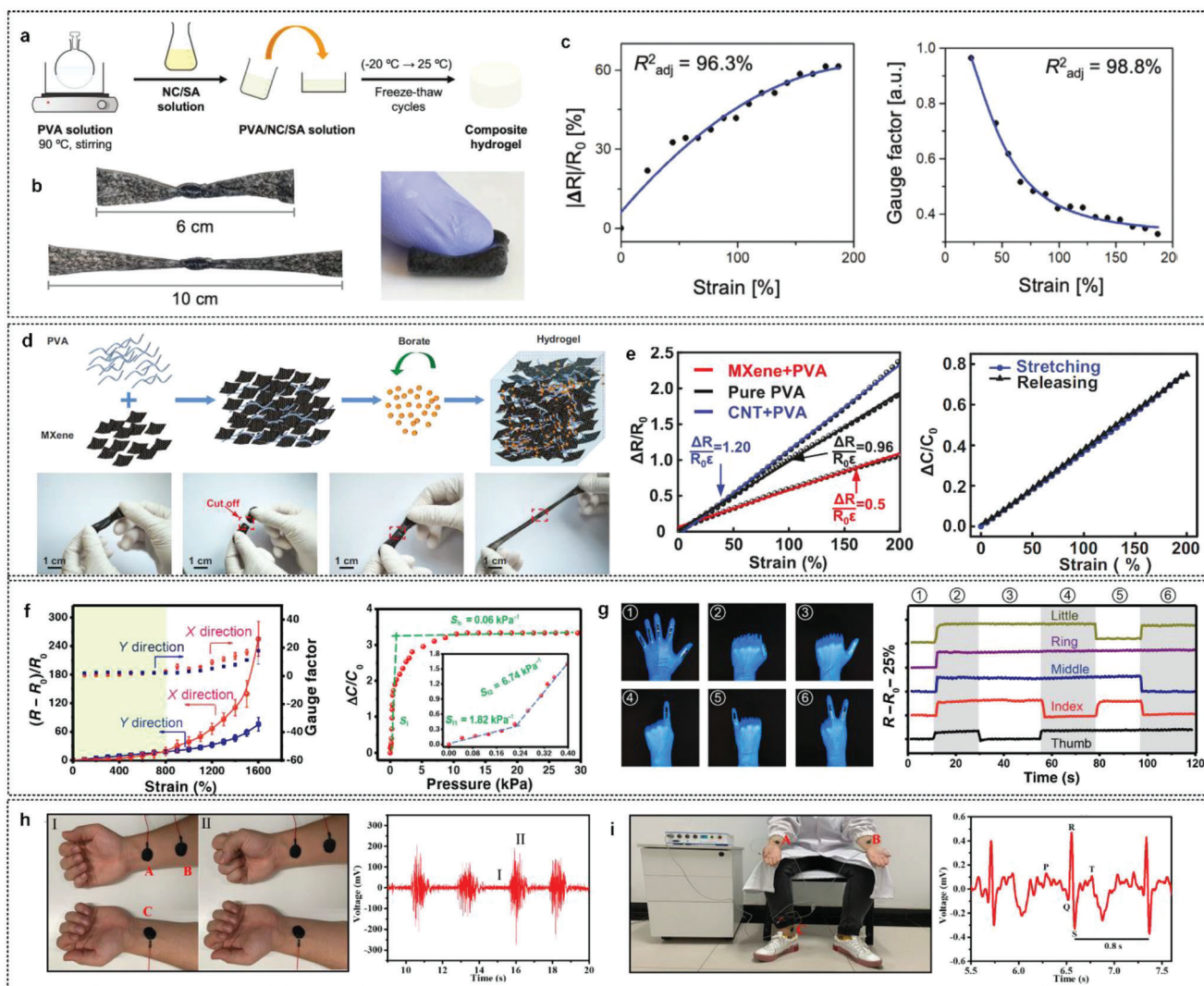


Figure 11. Hydrogel-based wearable sensors for human physiological parameters monitoring. a) Schematic representation of the process flow involved in the synthesis of PVA/NC/SA composite hydrogel. b) Photographs demonstrating the toughness of the polypyrrole/bacterial nanocellulose composite incorporated conductive hydrogel. c) Plot (left) showing the strain versus relative resistance change response of the hydrogel. Plot (right) showing the gauge factor as a function of the applied strain.^[137] Reproduced with permission.^[137] Copyright 2022, Wiley-VCH GmbH & Co. d) Schematic representation of the process steps for synthesis of MXene–PVA hydrogel. Optical images of the hydrogel showing self-healability and stretchability. e) Plot comparing strain versus relative resistance change response of the MXene–PVA hydrogel with pristine and CNT–PVA hydrogels. Plot showing the strain versus relative capacitance change response of the MXene-hydrogel capacitive sensor for one cycle of stretch–release.^[138] Reproduced with permission.^[138] Copyright 2019, Wiley-VCH GmbH & Co. f) Plot comparing strain versus relative resistance change response of the MXene–PpyNW–VSNP–PAM hydrogel-based resistive sensor in x- and y-directions. Plot showing the pressure versus relative capacitance change response of the MXene–PpyNW–VSNP–PAM hydrogel-based capacitive sensor. g) Photographs showing the MXene–PpyNW–VSNP–PAM hydrogel-based resistive sensor on a glove for finger movements detection. Plots showing the sensor responses acquired while finger movements.^[139] Reproduced with permission.^[139] Copyright 2020, American Association for the Advancement of Science. h) Electrodes configuration on the wrist for EMG detection. Plot showing EMG signals while wrist clenching. i) Electrodes configuration on wrist and ankle for ECG detection. Plot showing the acquired ECG signals.^[140] Reproduced with permission.^[140] Copyright 2014, American Chemical Society.

fulfill the critical needs of conformality, compatibility, and skin-like self-healing ability, novel hydrogel-based electrodes are emerging as attractive alternatives owing to their high stretchability, biocompatibility, and self-healing ability. Xuan and colleagues in their innovative work addressed the problems associated with traditional electrodes by developing a MXene/PVA hydrogel-based highly stretchable electrode for wearable capacitive electronic skin.^[138] A mixture of PVA and MXene solution

was prepared by stirring followed by the addition of sodium tetraborate and subsequent gelatinization to obtain the hydrogel. The schematic in Figure 11d (top) shows the steps involved in the synthesis of MXene/PVA hydrogel. The hydrogel demonstrates a high stretchability up to 1200% strain and fast self-healability (Figure 11d (bottom)). The combination of MXene and PVA facilitates the ultrafast self-healability in the electrodes due to the abundance of hydrophilic –OH group in MXene.^[138] An

optimal MXene concentration of 5.0 mg mL⁻¹ was chosen as the electrode material and further electromechanical characterization tests were conducted to determine the stability of the electrodes under high strains. The plot in Figure 11e (left) compares the strain versus relative resistance change response of the MXene/PVA hydrogel electrode with pristine PVA and CNT/PVA electrodes. The MXene/PVA hydrogel electrode shows a strain-induced normalized resistance change of 1.0 at a strain of 200%, which is significantly lower than its pristine PVA and CNT/PVA hydrogel counterparts. The strain insensitivity affirms the usability of the MXene/PVA hydrogel for use as electrodes in flexible capacitive sensing. The capacitive sensor reported here features a VHB (4905, 3 M) tape as a dielectric layer sandwiched between two layers of MXene/PVA hydrogel electrodes. The plot in Figure 11e (right) shows the strain versus relative capacitance change up to 200% strain for one loading–unloading cycle. The devices demonstrated a negligible hysteresis behavior with a gauge factor of ≈ 0.4 . The potential application of the sensor in human physiological parameter monitoring was demonstrated by a series of preliminary tests involving epidermal movement during drinking, water droplet loading, and finger proprioception.

Cai et al. demonstrated an ultrastretchable and self-healable MXene hydrogel heterostructures based piezoresistive and capacitive sensors for human physiological parameters monitoring.^[139] One of the main foci of the work was the synthesis of vinyl silica nanoparticle–polyacrylamide (VSNP–PAM) hydrogel as the robust substrate material. The substrate material was optimized for toughness and hysteresis behavior by varying the content of VSNP. A variation of VSNP in the range of 0–0.2 wt% was found to have a positive impact on breaking and tensile strength with a maximum tensile strength of 52.5 kPa achieved at 0.1 wt% (of VSNP) and a maximum breaking strain of 2800% obtained at 0.05 wt% (of VSNP). For the active sensing element, an innovative orthogonally buckled sensing array entailing layers 1D polypyrrole nanowires (PpyNWs) and MXene nanosheets were spray coated in a layer-by-layer fashion. The substrate was prestretched (1000%) in the y -direction and subsequently spray-coated with a continuous layer of PpyNWs followed by prestretching and spray-coating of the MXene layer in the x -direction. A combination of spring-like PpyNWs morphology and crumpled MXene patterns were achieved by conditioning the device through a series of prestretching–release cycles, which enables a completely reversible stretching behavior (up to 30 times the original size) in x - and y -directions. The plot in Figure 11f (left) shows the strain versus relative resistance change behavior of the sensor in the x - and y -directions. The sensor demonstrates a linear behavior up to 800% strain with maximum gauge factors of 16.9 and 11.2 in the x - and y -directions, respectively. A capacitive sensor featuring the MXene–PpyNW–VSNP–PAM and VHB tape dielectric was demonstrated for tactile pressure and proximity sensing. The plot in Figure 11f (right) the normal pressure versus relative capacitance changes response of the sensor. The sensor demonstrated pressure sensitivity values of 1.82 kPa⁻¹ (<0.2 kPa) and 6.74 kPa⁻¹ (0.2–0.4 kPa). The applicability of the sensor for e-skin applications was demonstrated with a series of tests involving joint kinesthetics, pulse wave detection, and a smart glove. The smart glove comprised of five identical piezoresistive

sensors and was shown to identify all the finger movements accurately.

Though most of the wearable e-skin sensors focus on mechanical sensing to detect vital human physiological parameters, electrophysiological signals such as electromyogram (EMG) and electrocardiogram (ECG) relevant for monitoring nerve, muscle, and cardiac health must also be acquired for achieving well-rounded physiological wellness monitoring. Thus, conductive hydrogel-based sensors are not only relevant for mechanical physiological parameter monitoring but also for electrophysiological monitoring. Li et al. reported a facile epidermal sensor featuring conductive hydrogel composed of MXene, poly(acrylic acid) (PAA), and amorphous calcium carbonate (ACC).^[140] The composite is self-healable and can be decomposed in a phosphate-buffered saline solution thus reducing its overall environmental impact. Mechanical characterization revealed an elastic modulus of 300 kPa with a maximum elongation of 450%, which makes it more stretchable than the skin. A series of human motion monitoring experiments entailing finger and arm bending, phonation, and pulse rate detection were conducted to underscore the capability of the sensor for resistive mechanical sensing. The capability of the MXene/PAA/ACC hydrogel as epidermal electrodes for EMG and ECG signal detection were demonstrated. As shown in Figure 11h (left) two electrodes were configured on the right hand to measure EMG during wrist flexor contraction and one electrode was affixed on the left arm to serve as the ground electrode. The plot in Figure 11h (right) shows EMG signals acquired while fist clenching in a periodic fashion. The electrodes demonstrated a superior signal-to-noise ratio of 19.96 dB, which can be attributed to excellent contact between the skin and electrodes as compared to Ag/AgCl electrodes.^[140] The electrodes were also attached to the left and right forearms for the acquisition of ECG signals. In this case, a third electrode was affixed to the ankle to serve as the ground electrode as shown in Figure 11i (left). The plot in Figure 11i (right) shows the ECG signals acquired employing the setup where the P, Q, R, S, and T peaks could be clearly discerned.

4.3. 3D Porous Structures

Though nanomaterial–polymer composite-based planar sensors have gained mainstream popularity, applications requiring extremely high compressive strains remain elusive for most 1D/2D nanomaterial-based planar sensors. 3D structures in the form of foams, aerogels, and sponges have been widely used in the engineering community for sensing, packaging, electromagnetic interference shielding, superadsorbents, and biological scaffolds owing to their large specific surface area, ultralightweight nature, low Young's modulus, and low density.^[149–151] From the perspective of human physiological parameters monitoring, sensors targeted for plantar pressure detection for gait monitoring applications should be capable of bearing large compressive strain and planar sensors might not be ideal for such applications. Carbonaceous and metallic nanomaterials are usually synthesized in the form of 1D nanowires/nanotubes or 2D nanosheets such as graphene/MXene and transformation into a 3D porous form without any additive is difficult and rare. In the last few decades, the sensor community has witnessed a

significant amount of research pertaining to nanomaterials-based 3D networks such as aerogels, sponges, and foams tailored for highly squeezable and compressible sensing applications. The porous structures of such 3D nanomaterial composites not only make them suitable for applications involving large structural deformation/compressive strain but also help reduce their stiffness and density thereby facilitating their applications in ultralightweight and robust wearables.

Yao et al. proposed an innovative graphene-coated PU sponge piezoresistive sensor based on a fractured microstructure design.^[152] The spongy pressure sensor works on the principle of conductive domain disconnection (discussed previously) between the rGO-coated cracked PU fibers (as shown schematically in Figure 12a). To underscore the importance of fractured microstructure design on pressure sensitivity, the fractured microstructure rGO-PU sponge was compared with a sponge without fractures. The plot in Figure 12b compares the pressure versus relative resistance change characteristics of the fractured microstructure-based spongy sensor to that of its nonfractured counterpart. In comparison to the nonfractured rGO-PU sponge, the fractured counterpart demonstrated two orders of magnitude sensitivity enhancement in the pressure regime 0–2 kPa and one order of magnitude enhancement in the 2–10 kPa regime. The process scalability was demonstrated by fabricating a 13×11 -pixel array with a temporal resolution of $4 \text{ mm}^2 \times 4 \text{ mm}^2$ for potential applications in artificial skin.^[152]

Combining the effects of conductive contact separation and variation of microcrack junction (inspired from spider's sensor slit organ) can potentially lead to a wide pressure and strain sensing range.^[153] Wu et al. reported a novel method of fabricating carbon black-coated PU piezoresistive sponges employing polymer-mediated water-based layer-by-layer assembly as shown schematically in Figure 12c.^[153] Electromechanical assessments were conducted on the CB-PU spongy sensor to determine its sensitivity. The plot in Figure 12d shows the pressure versus relative resistance change behavior of the sensor. The authors argued that for region A ($< 2.3 \text{ kPa}$) microcrack-induced resistance change mechanism dominates thereby leading to a positive slope with a pressure sensitivity of 0.068 kPa^{-1} . Whereas, for regions B and C ($> 2.3 \text{ kPa}$), contact separation-induced resistance change dominates thereby leading to negative slopes and sensitivities of 0.023 and 0.036 kPa^{-1} , respectively.^[153] Accelerated lifetime performance assessments spanning over 50 000 cycles of loading revealed the robustness of the sensors. A variety of human motion monitoring experiments involving phonation, pulse, respiration, and kinesthetics were conducted to assess the suitability of the sensors for real-life applications.

Pang et al. for the first time demonstrated a graphene porous network (GPN) PDMS composite-based piezoresistive sensor capable of both pressure and strain sensing. A nickel foam template-based scaffolding was employed for the fabrication of the GPN-PDMS foam sensor.^[26] The sensor demonstrated a pressure sensitivity of 0.09 kPa^{-1} ($< 1 \text{ MPa}$) and tensile gauge factors of 2.6 and 8.5 in the strain ranges 0–18% and 22–40%, respectively.

Freestanding graphene-based aerogels are fragile and not suitable for applications in wearables that demand structural robustness, large strain-bearing capability, and high sensitivity. Qin et al. proposed an ultralightweight piezoresistive foam sensor

by introducing water-soluble polyimide precursors into graphene oxide sheets.^[154] GO dispersion was mixed with poly(amic acid) (PAA, PI precursor) and subsequently freeze-dried. Finally, thermal annealing at $300 \text{ }^\circ\text{C}$ in argon ambient was conducted to form rGO/PI nanocomposite. The process steps involved in the synthesis of the rGO-PI foam are schematically represented in Figure 12e. The resulting rGO-PI foam was ultralightweight as demonstrated by the photograph in Figure 12e where the foam rests on bristlegrass. The rGO-PI foam was subjected to electromechanical assessments to determine its pressure sensitivity. The sensor demonstrated two linear regions with pressure sensitivities of 0.18 kPa^{-1} in the pressure regime 0–1.5 kPa and 0.023 kPa^{-1} in the 3.5–6.5 kPa regime as shown by the pressure versus relative resistance change plot in Figure 12f.

Liu et al. proposed a facile method of fabrication of graphene-TPU foam employing the thermally induced phase separation technique.^[150] The resulting composite foam demonstrated a density of 0.11 g cm^{-3} and a high porosity of 90%. The photograph in Figure 12g shows the graphene-TPU foam resting on a leaf emphasizing its ultralightweight nature. The SEM image in Figure 12g shows the magnified view of the graphene-TPU cell strut. The magnified image inset shows the dispersion state of graphene with a wrinkled structure. The TPU foams with 0.1 wt% graphene were chosen for their stable conductivity for sensitivity assessments. Interestingly, as opposed to many other spongy sensors reported in the literature, the graphene-TPU foam demonstrated a reverse piezoresistive behavior under compressive strain where the relative resistance changes increased (instead of decreasing). The authors attributed this peculiar behavior to the fracture of TPU cell walls thereby leading to contact separation among graphene nanoflakes upon compression.^[150] The plot in Figure 12h shows the compressive strain versus relative resistance change response of the sensor for strains up to 90%. The sensor demonstrated two linear regimes with gauge factors of 2.45 ($\epsilon < 60\%$) and 12.24 ($\epsilon > 60\%$).

Zhang et al. proposed a 3D porous structure-based piezoresistive spongy sensor based on a cracked cellulose nanofibril/silver nanowire layer-coated PU sponge.^[10] The conductive sponge was prepared by a simple dip-coating method followed by a precompression treatment (80% strain at 5 mm min^{-1} strain rate) to induce a cracked structure in the PU sponge backbone. The plots in Figure 12i show the strain versus relative resistance change response of the sensor. The sensor demonstrates three distinct sensing regimes as observed from the plot in Figure 12i (left). Similar to the case of the CB-PU-based sensor discussed earlier,^[153] the distinct regimes of operation could be explained by invoking the microcrack-induced resistance change mechanism which dominates region I (demarcated by green in Figure 12i (right)). For region II, ($0.6\% < \epsilon < 70\%$) contact separation-induced resistance change dominates which results in a rapid decrease of resistance initially followed by a slower rate of resistance change. A similar argument can be made for region III ($70\% < \epsilon < 80\%$) where contact between adjacent cracked PU fibers dominates. The maximum gauge factor was determined to be 26.07 for region I. The sensors of applied for a series of experiments involving phonation, gait monitoring, and joint movement detection. Finally, an electronic skin composed of 5×5 sensor arrays was demonstrated. The color maps in Figure 12j show the response of the artificial skin to a 100 g weight and a small globe.

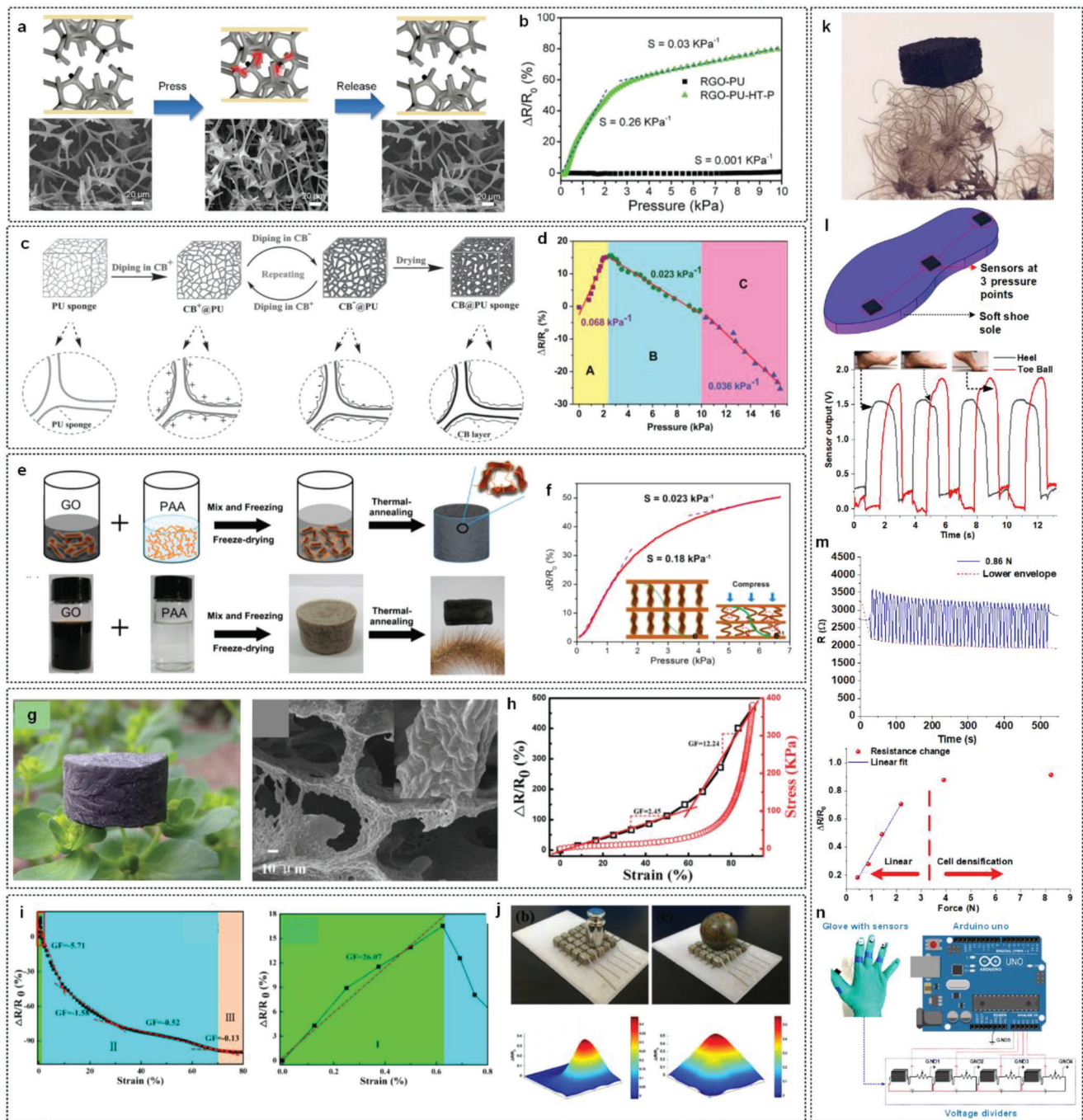


Figure 12. Nanomaterial–polymer composites-based 3D porous structures for piezoresistive sensing. a) Schematic and images modeling the working mechanism of rGO-PU piezoresistive sponge. b) Plot Showing the pressure characteristics curves of rGO-PU sponges with fractured and nonfractured structures.^[152] Reproduced with permission.^[152] Copyright 2013, Wiley-VCH GmbH & Co. c) Schematic representation of the steps involved in the fabrication of the CB-PU sponge.^[153] Reproduced with permission.^[153] Copyright 2016, Wiley-VCH GmbH & Co. d) Plot showing pressure versus relative resistance change response of the CB-PU sponge comprising of three distinct sensitivity regions.^[153] Reproduced with permission.^[153] Copyright 2016, Wiley-VCH GmbH & Co. e) Schematic representation of the process steps in the synthesis of rGO-PI composite. f) Plot showing pressure versus relative resistance change response of the rGO-PI sponge.^[154] Reproduced with permission.^[154] Copyright 2020, American Chemical Society. g) Photograph of the graphene–TPU foam resting on a leaf. SEM image showing the magnified view of the cell strut of graphene–TPU foam. h) Plot showing strain versus relative resistance change response of the graphene–TPU foam.^[150] Reproduced under the terms of the Creative Commons CC BY 3.0 license.^[150] Copyright 2016, the Authors, published by RSC. i) Plot (left) showing strain versus relative resistance change response of the cracked cellulose nanofibril/silver nanowire layer-coated PU sponge. Plot (right) showing a magnified view of the boxed (red) region. j) Demonstration of the 5 × 5 pixels artificial skin. Color map showing the pressure mapping on the placement of various objects.^[10] Reproduced with permission.^[10] Copyright 2019, American Chemical Society. k) Photograph of graphene–PDMS sponge resting on a dry flower. l) Schematic representation of graphene–PDMS-based sensorized insole. Responses from toe ball and heel region of a person while walking.^[40]

Sengupta et al. proposed a facile method entailing dip coating of sugar-scaffolded porous PDMS sponges in multilayer graphene nanoflake dispersion in *N,N*-dimethylformamide (concentration $\approx 2 \text{ mg mL}^{-1}$) to fabricate graphene–PDMS piezoresistive sponges tailored for human gait monitoring applications.^[40] The photograph in Figure 12k shows the graphene–PDMS sponge resting on a dried flower thus emphasizing its ultralight weight nature. The spongy piezoresistive sensors demonstrated average gauge factors in the range of ≈ 2.87 – 8.77 in the strain range of ≈ 0 – 50% . The sensor demonstrated a linear response for quasi-static compressive strains up to 9.5% with an average gauge factor of 8.77 . The sensors demonstrated robust and repeatable relative resistance change behavior over $\approx 36\,000$ cycles of compressive cyclic loading. Three identical sensors were affixed on the toe ball, middle arch, and heel regions of a soft insole (schematically represented in Figure 12l) placed inside a sports shoe. A series of gait and qualitative plantar pressure monitoring experiments were conducted to assess the suitability of the graphene–PDMS sensors for gait and human motion monitoring applications. The plot in Figure 12l shows the sensor responses from the toe ball and heel regions of the insole while a person walked slowly. The phase lag between the heel lift and toe ball touch can be discerned clearly from the sensor responses. Also, the sensorized shoe insole was applied to monitor the running gait and leaning movement of a person. Furthermore, the sensor responses from the smart insole with three sensors attached were demonstrated to be applicable in differentiating between low arch (flat) foot and medium arch foot thus underscoring the system's capabilities in potential use cases in qualitative detection of foot anomalies.

Previously, Kamat et al. observed an anomalous overshooting behavior in the resistance change response of graphene-coated microlattice-based 3d printed piezoresistive sensors when subjected to a series of cyclic uniaxial compressive loading.^[155] The authors attributed the resistance overshooting behavior to the “spring back” effect caused by the top electrode of the sensor losing contact with the compression test setup. However, anomalous overshooting behavior can possibly be attributed to several underlying mechanisms. The phenomenon could be further explained by observing the unprocessed resistance change signal in response to 0.86 N uniaxial compressive loading of an improved graphene–PDMS piezoresistive sensors reported by Sengupta et al. (shown by the plot in Figure 12m).^[36] As observed from the plot in Figure 12m, the sensor demonstrated an initial sharp increase in resistance followed by a steady decrease in resistance in response to uniaxial compressive loading, which is manifested as overshooting behavior of the resistance change response. Similar behaviors have been observed previously by several researchers.^[10,153,155] As observed from the work of Wu et al.^[153] and Zhang et al.,^[10] the initial increase in resistance can be explained by invoking a microcrack-induced resistance change mechanism, which leads to an initial increase in resistance with

compressive stress. For larger compressive stress regimes, the conductive domain disconnection mechanism becomes the dominant resistance change mechanism, which leads to a drop in resistance with large compressive stresses.

The improved graphene–PDMS spongy piezoresistive sensor reported by Sengupta et al. featured graphene-infused PDMS sponges with a density of 250 mg cm^{-3} and a porosity of $\approx 74\%$.^[36] Furthermore, the average compressive modulus of the sponges was found to be $\approx 56.7 \text{ kPa}$. The sensors demonstrated force sensitivity of 0.3068 , 0.2389 , and 0.2451 N^{-1} at 0.1 , 0.2 , and 0.3 Hz , respectively, with a linear force versus relative resistance response in the load range ≈ 0.42 – 2.18 N . The plot in Figure 12m (bottom) shows the force versus relative resistance change response of the sensor with a linear regression fit in the force range 0.42 – 2.18 N . The authors attribute the superior linearity in comparison to their previous work^[40] to lesser graphene loading and drying step at an elevated temperature of $120 \text{ }^\circ\text{C}$, which potentially helps in binding the graphene nanoflakes to the inner pore wall of the spongy PDMS base. The deviation from linear behavior post $\approx 2.18 \text{ N}$ load regime was attributed to cell densification occurring for higher compressive stress. The robustness and reliability of the sensor were demonstrated by conducting an accelerated lifetime assessment entailing 1500 cycles of uniaxial compressive loading at 3.90 N . The sensor demonstrated a stable response with baseline response changing from 2.2115 V (at the 400th cycle) to 2.3796 V (at the 1500th cycle). To demonstrate the usability of the sensors for practical applications in human physiological parameters monitoring, a smart haptic pressure sensing smart glove comprising of a nitrile glove with four identical sensors affixed on the fingertip region of the Thumb, index middle, and ring fingers was developed. The system was interfaced with an open-source microcontroller board (Arduino Uno) with voltage divider circuits for real-time data acquisition. Several activities demonstrating the capability of the system in real-time haptic pressure detection were demonstrated. Finally, three identical sensors were affixed behind the three blades of a Philips 7000 series electric shaver for real-time pressure monitoring while shaving.

4.4. Triboelectric Self-Powered Sensors

Since its initial conceptualization and introduction by Wang's group in 2012,^[50,51,156,157] the field of TENGs has seen an unprecedented growth in the last decade owing to the surge in demand for ultralow/self-powered wearables. From being considered as a negative effect/wasted energy in the past to being a mainstream research area in the field of energy harvesting and self-powered sensing, the triboelectric effect has come a long way. In general, TENGs can be categorized into four subclasses based on their modes of operation—vertical contact separation, single-electrode mode, in-plane sliding mode, and freestanding triboelectric layer

Reproduced with permission.^[40] Copyright 2019, the Authors, published by ACS. m) Plot (top) showing the resistance change responses of the improved graphene–PDMS sensor for 50 cycles of uniaxial compressive load at 0.86 N . Plot (bottom) showing the applied uniaxial force versus relative resistance change response of the sensor. n) Schematic representation of the IoT implementation of the graphene–PDMS sensors-based haptic pressure sensing smart glove with Arduino Uno platform.^[36] Reproduced under the terms of the Creative Commons CC BY 4.0 license.^[36] Copyright 2022, the Authors, published by IOP.

mode.^[158] In its core, a TENG entails two polymer materials stacked on top of each other (with or without a spacer) and sandwiched between two electrodes. The basic working mechanism of a TENG comprises three important steps, namely, charge generation, charge separation, and charge flow.^[51] When subjected to a mechanical deformation/physical stimulus, the structural arrangement leads to contact between the two polymer layers thereby generating electrostatic charges with opposite polarities on the two contacting layers.^[159] Upon release, as the two materials get separated, the transient polarization is broken and a potential difference is created between the two sandwiching electrodes which can drive a current through an externally connected load until the system reaches an equilibrium.^[160] The schematic diagram in **Figure 13a** represents the basic working principle of a TENG. When two materials with different surface potential properties come in contact with each other, contact electrification occurs leading to the formation of an interface dipole layer also referred to as the triboelectric potential layer.^[50] The triboelectric potential layer causes a net polarization between the two planar electrodes (connected to the two layers), which leads to the flow of electrostatically induced free charges through an external load connected across the two electrodes. The output performance of a TENG depends on the amount of contact electrification occurring between two materials which in turn is a function of the relative unique surface properties of the two materials constituting a TENG.^[160] The schematic in **Figure 13b** shows the triboelectric series, which can aid in choosing a pair of materials for designing a high-output TENG.

In one of the pioneering works that contributed to the foundation of TENGs, Fan et al. from Wang's group presented a flexible triboelectric generator comprising of two stacked layers of Kapton (125 μm thick) and PET (220 μm thick) films sandwiched between two thin layers of gold electrodes (100 nm thick).^[50] The schematics in **Figure 13c** show the structure and working principle of the device. The work involved extensive characterization experiments to establish the mechanism and working principle of TENGs. The plots in **Figure 13d** show the open-circuit voltage and short-circuit current signals from the triboelectric generator reported in the work. The device proposed in the work demonstrated an open-circuit characteristic during the I - V characterization experiments with a peak output voltage of 3.3 V and a peak current of 0.6 μA with a peak power density of 10.4 mW cm^{-3} .^[50] The significance of the work lies in its ability to harness a negative phenomenon and transform it into a unique technique capable of establishing a class of energy harvesters and self-powered sensors.

Fan et al. built up on their previous work^[50] with the goal of developing a micropatterned PDMS-based fully transparent TENG with higher area power density.^[51] In order to achieve complete light transparency, the gold electrodes were replaced with transparent ITO electrodes. Additionally, to enhance the charge generation due to friction and subsequently achieve superior power density, the PDMS layer was micropatterned to create various surface features (such as micropyramids, cubes, and lines) employing soft lithography as shown by the schematic diagram in **Figure 13e**. The scanning electron image and the corresponding inset in **Figure 13f** shows the pyramidal surface patterns on the PDMS layer reported in the work. The combination of the micropatterned PDMS layer with PET as the second

layer leads to superior charge generation and power density.^[51] A series of characterization experiments were conducted to assess the effectiveness of the various micropatterns in enhancing the triboelectric effect and subsequent power output. The plots in **Figure 13g** show the open-circuit voltage and short-circuit current output of the TENGs with different PDMS micropatterns with micropyramid-featured PDMS-based TENG showing the highest open-circuit voltage and short-circuit current outputs. The pyramid-featured device demonstrated a maximum output of 18 V and 0.7 μA with a reported power density of 0.13 $\mu\text{A cm}^{-2}$ when subjected to periodic bending at 0.33 Hz (0.13% strain). The authors attributed the superior performance of the micropatterned PDMS-based devices in comparison to the unstructured ones to three factors entailing:^[51] 1) superior friction and subsequent triboelectric effect in the devices with complex/sophisticated surface patterns; 2) the patterned surfaces lead to greater capacitance change between the electrodes while a device undergoes deformation by the virtue of piezocapacitive effect;^[78] and 3) the micropatterned surface-based devices achieve better charge separation thereby leading to large dipole moment being formed between the two electrodes of the TENG. The transparencies of the fabricated devices were characterized by employing UV-vis spectroscopy and the unstructured film-based devices showed a high transmittance of $\approx 75\%$. In comparison, the featured devices showed lower transmittance of $\approx 50\%$, which can be attributed to light scattering by the microstructures on the PDMS films. Finally, the applications of the TENG as a self-powered pressure sensor are demonstrated by conducting a series of pressure sensing experiments involving water droplet loading, feather dropping, and quasi-static force loading at three different frequencies (1, 5, and 10 Hz) using a linear motor. Finally, the lower detection threshold of the TENG-based sensor was determined as 13 mPa by calculating the response of the sensor to the loading/impact of a feather.

Though after its initial introduction by Wang's group in 2012 TENGs gained the attention of the research fraternity in a short span of time, its use was mostly limited to energy harvesting and flexible/wearable nanogenerators. Moreover, most of the initial work on flexible and inelastic/unstretchable TENGs overlooked the benefits associated with stretchable triboelectric layers, which are crucial to personal wearables and devices for human motion monitoring applications. In another pioneering work in 2015, Yi et al. from Wang's group introduced a novel stretchable rubber-based single-electrode TENG and explored its applications in human motion monitoring thereby establishing TENGs as stretchable self-powered sensors in addition to being effective power sources.^[161] The device featured a 200 μm thick stretchable rubber top layer and a 50 μm thick surface-treated (etched by anodization) aluminum layer serving a dual purpose of the electrode and the second triboelectric surface (schematically shown in **Figure 13h**). The scanning electron image in **Figure 13i** shows the nanoporous surface features on the aluminum electrode. The readers are directed to the original article for the detailed operating principle and accompanying COMSOL-based Multiphysics simulation explaining the underlying triboelectric generation mechanism.^[161] In brief, stretching the rubber enables in-plane charge separation between its surface and the aluminum layer, which results in different electrical potentials between the aluminum electrode and the ground and causes charges to flow

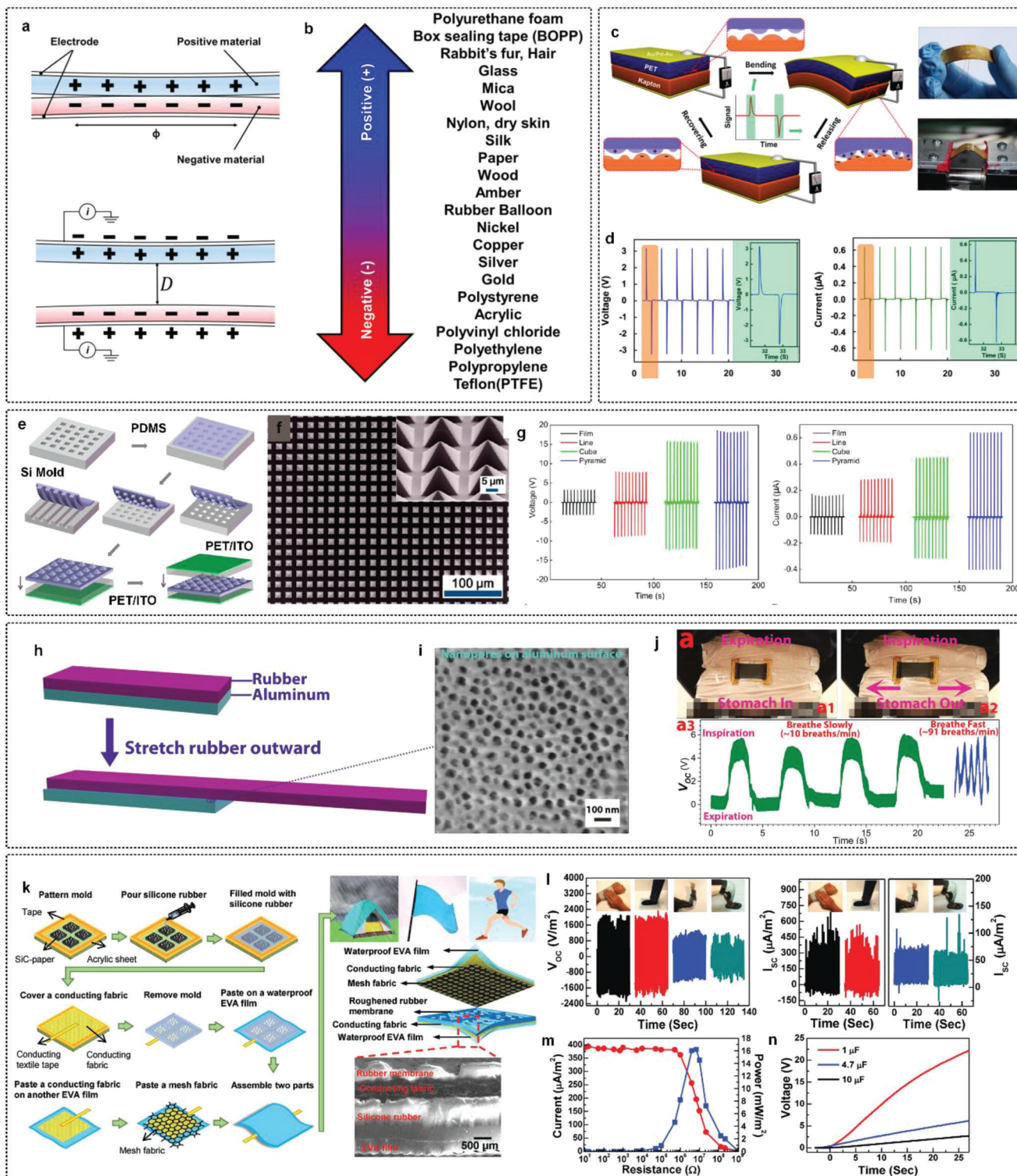


Figure 13. TENG-based self-powered sensors for human physiological parameters monitoring. a) Schematic representation of the contact electrification phenomenon between two different triboelectric materials. b) Schematic showing different triboelectric materials in series arranged as per their relative affinity to positive/negative charges.^[160] Reproduced with permission.^[160] Copyright 2018, Elsevier B.V. c) Schematic representation of the PET-Kapton-based flexible triboelectric generator proposed by Wang's group for the first time. d) Plots showing the open-circuit voltage and the short-circuit current, respectively, of the PET-Kapton-based flexible triboelectric generator under periodic flexion.^[50] Reproduced with permission.^[50] Copyright 2012, Elsevier B.V. e) Schematic representation of the process steps involved in the fabrication of surface microstructured PDMS film based transparent TENG. f) Scanning electron image showing the surface of the micropyramidal featured PDMS film. g) Plots comparing the open-circuit voltage (left plot) and

between the two. The work also assessed the effects of electrode width and the length of the rubber layer on the TENGs performance. It was reported that the increase in aluminum electrode width relative to the rubber layer increased the open-circuit voltage and charge density as long as the width of the electrode was lesser than the rubber layer. By contrast, the increase in the length of the rubber layer relative to the aluminum electrode negatively affects the open-circuit voltage and charge density of the TENG owing to the reduction in charge separation between the two layers. Furthermore, a series of characterization tests were conducted to assess the performance of the device to stretching strain. Both the open-circuit voltage and current density demonstrated nearly linear behaviors with respect to increasing stretching strains. Finally, a series of experiments involving movement direction detection, respiratory pattern detection, and joint movement monitoring were conducted to underscore the applicability of the proposed TENG-based sensors to real-life human motion monitoring. The application of the SR-based TENG as a self-powered breathing sensor is illustrated in Figure 13j. A 50 μm thick polytetrafluoroethylene film was used for isolating the aluminum electrode from the human body and the sensor assembly is secured on the diaphragm region of the abdomen employing a string. Slow and fast diaphragmatic breathing motions were monitored in real-time as shown by the plots in Figure 13j. This work was one of the earliest to report the use of TENGs as self-powered sensors for human physiological parameters monitoring and subsequently paved the way for a new class of TENG-based self-powered sensors.

One of the key advantages of TENGs is their flexibility/apparel conformability, which facilitates their applications in personal wearables. Recently, several fibrous and fabric-based TENGs (f-TENG) have been reported in the literature.^[53,162,163] Fabric-based TENGs offer the advantages of apparel integrability and high deformability enabling them to be highly suitable for wearables for human physiological parameters monitoring. Though f-TENGs are particularly attractive for applications in wearables, many of the reported devices are not built to last in humid environments, which can severely restrict their use in real-life wearables demanding high resistance to sweat and water splashes. Lai et al. reported a waterproof fabric-based TENG capable of harvesting energy from various unconventional sources including impacts from rain droplets, human motion, and subtle wind motion.^[53] The water-resistant multifunctional TENG featured two layers of laminated fabric with the bottom layer comprising of a roughened rubber membrane stacked on top of a conducting fabric placed on an ethylene-vinyl acetate (EVA) bottom lining for water resistance. Similarly, the top fabric featured a mesh fabric stacked

on top of a conducting fabric placed on a water-resistant EVA film. The sensor was assembled by gluing the top and bottom layers at the border while the outside EVA film tendered the assembly with the desirable water resistance property. Figure 13k schematically represents the process steps involved in the fabrication of the water-resistant f-TENG. A series of experiments were conducted to show the capability of the device to harvest energy from rainfall and airflow. To demonstrate its applicability in wearables for human motion monitoring and apparel-based energy harvesting, the f-TENG (dimensions $\approx 8 \times 11.6 \text{ in.}^2$) was worn and applied to a series of human motion monitoring tasks involving tapping, stepping, elbow, and knee flexion. The plots in Figure 13l show the open-circuit voltage and short-circuit current outputs of the f-TENG in response to tapping, stepping, elbow and knee flexion. The plot in Figure 13m shows the power generation capability of the sensor to tapping motion with a maximum power output of $\approx 16 \text{ mW m}^{-2}$ (at a load of 6.8 M Ω). The energy generated from the tapping motions was stored in three different capacitors as shown by the plot in Figure 13n. To further demonstrate the integrability of the f-TENGs in wearables for rainfall harvesting, the TENGs were integrated into various rain gears including a raincoat and an umbrella and subsequently shown to power LEDs in response to rainfall impact. Additionally, the f-TENGs were integrated into the shoe insole and sleeve of a coat for the purpose of extracting energy from general human motion. Finally, the application of the f-TENG in a self-powered human-machine interface was demonstrated by fabricating a wearable on-sleeve fabric-based keypad for remote music control. In contrast to many previously reported TENGs which were sensitive to water-related damage, the f-TENG reported in this work offers multipurpose energy harvesting capability and a waterproof design making it usable in a variety of harsh environments encountered in real-life human motion monitoring applications.

Recently, coaxial fibers featuring internal conductive networks^[164,165] have gained popularity in the fabrication of wearable sensors owing to their remarkable resilience under various mechanical deformations, including bending and tension, rendering them highly suitable for the development of triboelectric tactile sensors with multimodal sensing abilities.^[166] In a recent work, Yan et al. reported a multimodal piezoresistive and triboelectric-based pressure and strain sensor tailored for human motion monitoring and gesture recognition.^[166] The sensor featured silver nanowire-coated nylon thread as the flexible conductive core electrode and a CNTs/parafilm layer as the piezoresistive shell sensing element. The sensing capability of the device in triboelectric sensing mode was demonstrated by conducting a series of human motion experiments involving

short-circuit current (right plot) of the unstructured PDMS film-based TENG with the surface patterned counterparts.^[51] Reproduced with permission.^[51] Copyright 2012, American Chemical Society. h) Schematic representation of the device structure of the stretchable rubber based TENG. i) SEM image showing the nanoporous surface of the surface-treated aluminum film-based electrode. j) Photographs of the stretchable rubber-based TENG secured on the abdomen of a human subject for diaphragmatic breathing monitoring. Plots showing the response of the TENG-based sensor to fast and slow diaphragmatic breathing.^[161] Reproduced with permission.^[161] Copyright 2015, Wiley-VCH GmbH & Co. k) Schematic representation of the process steps involved in the fabrication of the water-resistant fabric-based TENG. Schematic representation of the cross-sectional blown-up view of the fabric-based TENG. SEM image showing the cross-sectional view of the bottom half of the TENG. l) Plots showing the open-circuit voltage (left) and short-circuit current (right) outputs of the fabric-based TENG in response to various human body movements including tapping, stepping, and joint flexions. m) Plots showing the output current and power density of the TENG at different external loads in response to hand tapping. n) Plot showing the charging response of three different capacitors (1, 4.7, and 10 μF) connected to the TENG in response to hand tapping.^[53] Reproduced under the terms of the Creative Commons CC BY 4.0 license.^[53] Copyright 2019, the Authors, published by Wiley VCH.

finger proprioception, elbow flexion, gait monitoring, and finger gesture recognition. Further experimental demonstrations were reported to apply the textile in piezoresistive mode. An array of tactile sensors was fabricated by placing the conductive threads perpendicular to each other and forming a grid-sensing array. The assembly was capable of mapping pressure in 2D space. The uniqueness of the work lies in its ability to couple piezoresistive and triboelectric effects and apply them to multimodal sensing tailored to human motion monitoring.

In addition to the works discussed here, several interesting recent works have focused on the application of TENG-based self-powered sensors to human motion monitoring and biomechanical sensing.^[167,168] Furthermore, research efforts have been channeled toward coupling environmentally sustainable and eco-friendly TENGs with custom-developed machine learning models for human motion prediction with a high degree of accuracy.^[52] In addition to the applications of TENGs toward human motion monitoring, several research groups have focused on the structure and surface morphologies of triboelectric devices with the goal of optimizing their performance. In particular, in the past several biomimetic strategies have also been adopted to improve the performance of TENGs. A comprehensive review of biomimetic TENGs and their applications is conducted by Li et al. in their topical review article.^[169]

5. Conclusion and Outlook

This article presented a comprehensive review of the recent advances in skin-inspired mechanical sensors for human physiological parameters monitoring. A brief discussion on the underlying mechanoreceptors of human skin was presented and an argument was put forward to justify the importance of human skin inspiration for the development of next-generation wearables. To acquaint the readers with the fundamentals of sensing principles that form the backbone of mechanical sensing, the historical background of piezoresistive, capacitive, and piezocapacitive sensing was presented. Armed with the knowledge of sensing fundamentals, this article explored the recent advances in nanoengineered materials encompassing fibrous structure, 2D nanomaterial fillers, and 3D porous structures and their applications in skin-inspired mechanical sensing. It was identified that for most nanomaterial–polymer composites-based piezoresistive sensors, microcrack-induced resistance change, and contact separation/conductive domain disconnection-induced resistance mechanism dominate. It was also stressed that modern piezocapacitive sensing could pose as an attractive alternative because of its low power budget, low hysteresis, and ultrafast response. While sensing materials have been approached with great rigor in the literature, more work is required on developing stretchable highly conducting electrodes. From the review, it was identified that one of the key bottlenecks hindering progress toward the development of skin-mountable ergonomic sensors is the electrical contact for reliable data acquisition. Traditional metallic conductor-based low-resistance contacts typically cause stress concentration centers in flexible devices thereby leading to premature failure. On the other end of the spectrum, conductive polymer-based flexible electrical contacts suffer from low conductivity and degradation over time. Research efforts are required toward developing polymer-based flexible electrodes, which do not

compromise conductivity. It was also identified that in addition to being wearable and cost-effective, the new generation of wearable sensors must be power efficient and robust, which would enable long-term usage without the need of frequent battery replacement/recharge. As such, there has been a recent upsurge in the research effort toward developing highly resilient and robust self-powered sensors based on the triboelectric effect. Toward the end, a dedicated section summarizing the recent progress in the field of TENG-based flexible, stretchable, and wearable self-powered sensors is included. Furthermore, wearable sensors in real applications suffer from problems related to integration, wiring, and data processing. More emphasis would be required in the future in developing problem-centric wearable solutions that take a comprehensive system-level approach toward showing human movement monitoring demonstrations. The literature also lacks comprehensive tests with a focus on human physiological parameter monitoring over extended periods of time. Most of the existing literature presented a handful of devices tested at labs. Tests involving multiple subjects and results with statistical significance are still missing and hence the field leaves a lot to be desired.

During the course of the review, it was apparent that the flexible sensor community is moving toward hydrogel-based substrates for their morphological and mechanical resemblance to natural skin. Still, several challenges pertaining to robustness, scalability, and cost-effectiveness need to be addressed for the successful transformation of research outputs into consumer-grade mass-market devices. Finally, multidisciplinary approaches toward wearable sensor development are required, which combines knowledge of electronic sensing materials with the know-how of IoT-backed wireless wearable data acquisition systems, big data processing, and visualization techniques to attain system-level solutions that could be practical in offering solutions to real-life problems.

Acknowledgements

This research was supported by the University of Groningen's start-up grant awarded to A.G.P.K.

Conflict of Interest

The authors declare no conflict of interest.

Author Contributions

Writing—original draft preparation, D.S.; writing—review and editing, A.G.P.K.; supervision, A.G.P.K.

Keywords

conductive hydrogels, graphene, piezocapacitive, piezoresistive, sensors, TENG, wearables

Received: June 28, 2023

Revised: September 11, 2023

Published online: October 24, 2023

- [1] J. Park, M. Kim, Y. Lee, H. S. Lee, H. Ko, *Sci. Adv.* **2015**, *1*, 1500661.
- [2] D. Wang, Y. Lin, D. Hu, P. Jiang, X. Huang, *Composites, Part A* **2020**, *130*, 105754.
- [3] T. Wang, S. Li, X. Tao, Q. Yan, X. Wang, Y. Chen, F. Huang, H. Li, X. Chen, Z. Bian, *Nano Energy* **2022**, *93*, 106787.
- [4] B. Bhushan, *J. Adhes. Sci. Technol.* **2012**, *21*, 1213.
- [5] D. Yao, H. Cui, R. Hensleigh, P. Smith, S. Alford, D. Bernero, S. Bush, K. Mann, H. F. Wu, M. Chin-Nieh, G. Youmans, X. Zheng, *Adv. Funct. Mater.* **2019**, *29*, 1903866.
- [6] A. G. P. Kottapalli, M. Bora, M. Asadnia, J. Miao, S. S. Venkatraman, M. Triantafyllou, *Sci. Rep.* **2016**, *6*, 19336.
- [7] X. Zheng, A. M. Kamat, M. Cao, A. G. P. Kottapalli, *Adv. Sci.* **2023**, *10*, 2203062.
- [8] D. B. Leitch, K. C. Catania, *J. Exp. Biol.* **2012**, *215*, 4217.
- [9] D. Kang, P. V. Pikhitsa, Y. W. Choi, C. Lee, S. S. Shin, L. Piao, B. Park, K. Y. Suh, T. Il Kim, M. Choi, *Nature* **2014**, *516*, 222.
- [10] S. Zhang, H. Liu, S. Yang, X. Shi, D. Zhang, C. Shan, L. Mi, C. Liu, C. Shen, Z. Guo, *ACS Appl. Mater. Interfaces* **2019**, *11*, 10922.
- [11] M. T. Northen, C. Greiner, E. Arzt, K. L. Turner, *Adv. Mater.* **2008**, *20*, 3905.
- [12] E. A. Lumpkin, M. J. Caterina, *Nature* **2007**, *445*, 858.
- [13] V. E. Abraira, D. D. Ginty, *Neuron* **2013**, *79*, 618.
- [14] R. S. Johansson, J. R. Flanagan, *Nat. Rev. Neurosci.* **2009**, *10*, 345.
- [15] G. Li, S. Liu, L. Wang, R. Zhu, *Sci. Rob.* **2020**, *5*, eabc8134.
- [16] Y. Zhao, Z. Li, S. Song, K. Yang, H. Liu, Z. Yang, J. Wang, B. Yang, Q. Lin, *Adv. Funct. Mater.* **2019**, *29*, 1901474.
- [17] H. Kong, Z. Song, W. Li, Y. Bao, D. Qu, Y. Ma, Z. Liu, W. Wang, Z. Wang, D. Han, L. Niu, *ACS Nano* **2021**, *15*, 16218.
- [18] M. Amjadi, A. Pichitpajongkit, S. Lee, S. Ryu, I. Park, *ACS Nano* **2014**, *8*, 5154.
- [19] S. Sharma, A. Chhetry, M. Sharifuzzaman, H. Yoon, J. Y. Park, *ACS Appl. Mater. Interfaces* **2020**, *12*, 22212.
- [20] H. Liu, Q. Li, S. Zhang, R. Yin, X. Liu, Y. He, K. Dai, C. Shan, J. Guo, C. Liu, C. Shen, X. Wang, N. Wang, Z. Wang, R. Wei, Z. Guo, *J. Mater. Chem. C* **2018**, *6*, 12121.
- [21] R. Mikkonen, A. Koivikko, T. Vuorinen, V. Sariola, M. Mantysalo, *IEEE Sens. J.* **2021**, *21*, 26286.
- [22] E. Papi, Y. N. Bo, A. H. Mcgregor, *Gait Posture* **2018**, *62*, 480.
- [23] C. Lou, S. Wang, T. Liang, C. Pang, L. Huang, M. Run, X. Liu, *Materials* **2017**, *10*, 1068.
- [24] L. Wang, D. Wang, K. Wang, K. Jiang, G. Shen, *ACS Mater. Lett.* **2021**, *3*, 921.
- [25] M. Amjadi, Y. J. Yoon, I. Park, *Nanotechnology* **2015**, *26*, 375501.
- [26] Y. Pang, H. Tian, L. Tao, Y. Li, X. Wang, N. Deng, Y. Yang, T.-L. Ren, *ACS Appl. Mater. Interfaces* **2016**, *8*, 26458.
- [27] T. Sharma, S.-S. Je, B. Gill, J. X. J. Zhang, *Sens. Actuators, A* **2012**, *177*, 87.
- [28] C. Chang, V. H. Tran, J. Wang, Y.-K. Fuh, L. Lin, *Nano Lett.* **2010**, *10*, 726.
- [29] B. J. Hansen, Y. Liu, R. Yang, Z. L. Wang, *ACS Nano* **2010**, *4*, 3647.
- [30] L. Persano, C. Dagdeviren, Y. Su, Y. Zhang, S. Girardo, D. Pisignano, Y. Huang, J. A. Rogers, *Nat. Commun.* **2013**, *4*, 1.
- [31] D. Sengupta, A. G. P. Kottapalli, S. H. Chen, J. M. Miao, C. Y. Kwok, M. S. Triantafyllou, M. E. Warkiani, M. Asadnia, *AIP Adv.* **2017**, *7*, 105205.
- [32] J. Yang, S. Luo, X. Zhou, J. Li, J. Fu, W. Yang, D. Wei, *ACS Appl. Mater. Interfaces* **2019**, *11*, 14997.
- [33] X. Yang, Y. Wang, X. Qing, *Sensors* **2018**, *18*, 2395.
- [34] Z. He, W. Chen, B. Liang, C. Liu, L. Yang, D. Lu, Z. Mo, H. Zhu, Z. Tang, X. Gui, *ACS Appl. Mater. Interfaces* **2018**, *10*, 12816.
- [35] H. K. Kim, S. Lee, K. S. Yun, *Sens. Actuators, A* **2011**, *165*, 2.
- [36] D. Sengupta, A. M. Kamat, Q. Smit, B. Jayawardhana, A. G. P. Kottapalli, *Flexible Printed Electron.* **2022**, *7*, 015004.
- [37] D. Sengupta, J. Romano, A. G. P. Kottapalli, *npj Flexible Electron.* **2021**, *5*, 1.
- [38] M. Amjadi, A. Pichitpajongkit, S. Lee, S. Ryu, I. Park, *ACS Nano* **2014**, *8*, 5154.
- [39] D. Sengupta, S.-H. Chen, A. Michael, C. Y. Kwok, S. Lim, Y. Pei, A. G. P. Kottapalli, *npj Flexible Electron* **2020**, *4*, 9.
- [40] D. Sengupta, Y. Pei, A. G. P. Kottapalli, *ACS Appl. Mater. Interfaces* **2019**, *11*, 35201.
- [41] Z. Ren, J. Nie, J. Shao, Q. Lai, L. Wang, J. Chen, X. Chen, Z. L. Wang, *Adv. Funct. Mater.* **2018**.
- [42] J. Tao, R. Bao, X. Wang, Y. Peng, J. Li, S. Fu, C. Pan, Z. L. Wang, *Adv. Funct. Mater.* **2019**, *29*, 1806379.
- [43] X. Wang, B. Li, O. L. Russo, H. T. Roman, K. K. Chin, K. R. Farmer, *Microelectron. J.* **2006**, *37*, 50.
- [44] J. A. Dziuban, A. Gorecka-Drzazga, U. Lipowicz, *Sens. Actuators, A* **1992**, *32*, 628.
- [45] S. H. Shin, S. Ji, S. Choi, K. H. Pyo, B. Wan An, J. Park, J. Kim, J. Y. Kim, K. S. Lee, S. Y. Kwon, J. Heo, B. G. Park, J. U. Park, *Nat. Commun.* **2017**, *8*, 1.
- [46] S. Jang, E. Jee, D. Choi, W. Kim, J. S. Kim, V. Amoli, T. Sung, D. Choi, D. H. Kim, J.-Y. Kwon, *ACS Appl. Mater. Interfaces* **2018**, *10*, 31472.
- [47] M. Kaltenbrunner, T. Sekitani, J. Reeder, T. Yokota, K. Kuribara, T. Tokuhara, M. Drack, R. Schwödiauer, I. Graz, S. Bauer-Gogonea, S. Bauer, T. Someya, *Nature* **2013**, *499*, 458.
- [48] M. Amjadi, K. Kyung, I. Park, M. Sitti, *Adv. Funct. Mater.* **2016**, *26*, 1678.
- [49] W. Li, D. Sengupta, Y. Pei, A. G. P. Kottapalli, FLEPS 2021 – IEEE Int. Conf. on Flexible Printable Sensors and Systems, IEEE, Piscataway, NJ **2021**.
- [50] F.-R. Fan, Z.-Q. Tian, Z. Lin Wang, *Nano Energy* **2012**, *1*, 328.
- [51] F.-R. Fan, L. Lin, G. Zhu, W. Wu, R. Zhang, Z. L. Wang, *Nano Lett.* **2012**, *12*, 3109.
- [52] Y. Liu, Y. Shen, W. Ding, X. Zhang, W. Tian, S. Yang, B. Hui, K. Zhang, *npj Flexible Electron.* **2023**, *7*, 21.
- [53] Y.-C. Lai, Y.-C. Hsiao, H.-M. Wu, Z. L. Wang, *Adv. Sci.* **2019**, *6*, 1801883.
- [54] D.-Y. Wang, L.-Q. Tao, Y. Liu, T.-Y. Zhang, Y. Pang, Q. Wang, S. Jiang, Y. Yang, T.-L. Ren, *Nanoscale* **2016**, *8*, 20090.
- [55] M. Hempel, D. Nezych, J. Kong, M. Hofmann, *Nano Lett.* **2012**, *12*, 5714.
- [56] S. Zhang, H. Zhang, G. Yao, F. Liao, M. Gao, Z. Huang, K. Li, Y. Lin, *J. Alloys Compd.* **2015**, *652*, 48.
- [57] J. G. Simmons, *J. Appl. Phys.* **1963**, *34*, 1793.
- [58] Z. Ounaies, *Compos. Sci. Technol.* **2003**, *63*, 1637.
- [59] G. R. Higson, *J. Sci. Instrum.* **1964**, *41*, 405.
- [60] C. S. Smith, *Phys. Rev.* **1954**, *94*, 42.
- [61] C. Herring, *Bell Syst. Tech. J.* **1955**, *34*, 237.
- [62] F. T. Geyling, J. J. Forst, *Bell Syst. Tech. J.* **1960**, *39*, 705.
- [63] C. Stampfer, A. Jungen, R. Linderman, D. Obergfell, S. Roth, C. Hierold, E. Zurich, M. Planck, **2006**, *6*, 1449.
- [64] M. Wautelet, *Eur J Phys* **2001**, *22*, 601.
- [65] S. Iijima, *Nature* **1991**, *354*, 56.
- [66] K. S. Novoselov, A. K. Geim, S. V. Morozov, D. Jiang, Y. Zhang, S. V. Dubonos, I. V. Grigorieva, A. A. Firsov, *Science* **2004**, *306*, 666.
- [67] T. W. Tomblor, C. Zhou, L. Alexseyev, J. Kong, H. Dai, L. Liu, C. S. Jayanthi, M. Tang, S. Y. Wu, *Nature* **2000**, *405*, 769.
- [68] A. D. Smith, F. Niklaus, A. Paussa, S. Vaziri, A. C. Fischer, M. Sterner, F. Forsberg, A. Delin, D. Esseni, P. Palestri, M. Östling, M. C. Lemme, *Nano Lett.* **2013**, *13*, 3237.
- [69] A. D. Smith, F. Niklaus, A. Paussa, S. Schröder, A. C. Fischer, M. Sterner, S. Wagner, S. Vaziri, F. Forsberg, D. Esseni, M. Östling, M. C. Lemme, *ACS Nano* **2016**, *10*, 9879.
- [70] C. Lee, X. Wei, J. W. Kysar, J. Hone, *Science* **2008**, *321*, 385.
- [71] V. M. Pereira, A. H. Castro Neto, N. M. R. Peres, *Phys. Rev. B* **2009**, *80*, 045401.

- [72] A. K. Geim, K. S. Novoselov, *Nat. Mater.* **2007**, *6*, 183.
- [73] X. Wang, D. D. L. Chung, *Smart Mater. Struct.* **1995**, *4*, 363.
- [74] X. Shui, D. D. L. Chung, *Smart Mater. Struct.* **1996**, *5*, 243.
- [75] M. Taya, W. J. Kim, K. Ono, *Mech. Mater.* **1998**, *28*, 53.
- [76] G. M. Marx, R. L. Bell, *SAE Tech. Pap.* **1978**.
- [77] C. S. Sander, J. W. Knutti, J. D. Meindl, *IEEE Trans. Electron Devices* **1980**, *27*, 927.
- [78] S. C. B. Mannsfeld, B. C.-K. Tee, R. M. Stoltenberg, C. V. H.-H. Chen, S. Barman, B. V. O. Muir, A. N. Sokolov, C. Reese, Z. Bao, *Nat. Mater.* **2010**, *9*, 859.
- [79] C. Pang, J. H. Koo, A. Nguyen, J. M. Caves, M.-G. Kim, A. Chortos, K. Kim, P. J. Wang, J. B.-H. Tok, Z. Bao, *Adv. Mater.* **2015**, *27*, 634.
- [80] C. Metzger, E. Fleisch, J. Meyer, M. Dansachmüller, I. Graz, M. Kaltenbrunner, C. Keplinger, R. Schwödiauer, S. Bauer, *Appl. Phys. Lett.* **2008**, *92*, 013506.
- [81] Y. Kim, S. Jang, B. J. Kang, J. H. Oh, *Appl. Phys. Lett.* **2017**, *111*, 073502.
- [82] J. Cai, S. Chawla, M. Naraghi, *Carbon* **2014**, *77*, 738.
- [83] N. Bhardwaj, S. C. Kundu, *Biotechnol. Adv.* **2010**, *28*, 325.
- [84] Z. Wang, T. Wu, Z. Wang, T. Zhang, M. Chen, J. Zhang, L. Liu, M. Qi, Q. Zhang, J. Yang, W. Liu, H. Chen, Y. Luo, L. Wei, *Nat. Commun.* **2020**, *11*, 1.
- [85] S. Khansari, S. Sinha-Ray, A. L. Yarin, B. Pourdeyhimi, *Ind. Eng. Chem. Res.* **2013**, *52*, 15104.
- [86] J. D. Hartgerink, E. Beniash, S. I. Stupp, *Science* **2001**, *294*, 1684.
- [87] T. D. Brown, P. D. Dalton, D. W. Huttmacher, *Adv. Mater.* **2011**, *23*, 5651.
- [88] Z.-M. Huang, Y.-Z. Zhang, M. Kotaki, S. Ramakrishna, *Compos. Sci. Technol.* **2003**, *63*, 2223.
- [89] W. E. Teo, S. Ramakrishna, *Nanotechnology* **2006**, *17*, R89.
- [90] X. Xiao, L. Yuan, J. Zhong, T. Ding, Y. Liu, Z. Cai, Y. Rong, H. Han, J. Zhou, Z. L. Wang, *Adv. Mater.* **2011**, *23*, 5440.
- [91] Y. Ding, J. Yang, C. R. Tolle, Z. Zhu, *RSC Adv.* **2016**, *6*, 79114.
- [92] J. Huang, D. Li, M. Zhao, A. Mensah, P. Lv, X. Tian, F. Huang, H. Ke, Q. Wei, *Adv. Electron. Mater.* **2019**, *5*, 1900241.
- [93] Y. Wang, S. Lee, T. Yokota, H. Wang, Z. Jjiang, J. Wang, M. Koizumi, T. Someya, *Sci. Adv.* **2020**, *6*, 7043.
- [94] D. Sengupta, M. Mastella, E. Chicca, A. G. P. Kottapalli, *ACS Appl. Electron. Mater.* **2022**, *4*, 308.
- [95] X. Wang, H. Sun, X. Yue, Y. Yu, G. Zheng, K. Dai, C. Liu, C. Shen, *Compos. Sci. Technol.* **2018**, *168*, 126.
- [96] Y. Li, B. Zhou, G. Zheng, X. Liu, T. Li, C. Yan, C. Cheng, K. Dai, C. Liu, C. Shen, Z. Guo, *J. Mater. Chem. C* **2018**, *6*, 2258.
- [97] Y. Wang, J. Hao, Z. Huang, G. Zheng, K. Dai, C. Liu, C. Shen, *Carbon* **2018**, *126*, 360.
- [98] D. Sengupta, D. Trap, A. G. P. Kottapalli, *Nanomaterials* **2020**, *10*, 211.
- [99] W. Yang, N.-W. Li, S. Zhao, Z. Yuan, J. Wang, X. Du, B. Wang, R. Cao, X. Li, W. Xu, Z. L. Wang, C. Li, *Adv. Mater. Technol.* **2018**, *3*, 1700241.
- [100] Y. Zhu, Y. Wu, G. Wang, Z. Wang, Q. Tan, L. Zhao, D. Wu, *Org. Electron.* **2020**, *84*, 105759.
- [101] P. Yu, X. Li, H. Li, Y. Fan, J. Cao, H. Wang, Z. Guo, X. Zhao, Z. Wang, G. Zhu, *ACS Appl. Mater. Interfaces* **2021**, *13*, 24062.
- [102] D. Sengupta, L. Lu, D. R. Gomes, B. Jayawardhana, Y. Pei, A. G. P. Kottapalli, *ACS Appl. Mater. Interfaces* **2023**, *15*, 22351.
- [103] A. Miyamoto, S. Lee, N. F. Cooray, S. Lee, M. Mori, N. Matsuhisa, H. Jin, L. Yoda, T. Yokota, A. Itoh, M. Sekino, H. Kawasaki, T. Ebihara, M. Amagai, T. Someya, *Nat. Nanotechnol.* **2017**, *12*, 907.
- [104] C. W. Nan, Y. Shen, J. Ma, *Annu. Rev. Mater. Res.* **2010**, *40*, 131.
- [105] D. Wilkinson, J. S. Langer, P. N. Sen, *Phys. Rev. B* **1983**, *28*, 1081.
- [106] N. Yousefi, X. Sun, X. Lin, X. Shen, J. Jia, B. Zhang, B. Tang, M. Chan, J.-K. Kim, *Adv. Mater.* **2014**, *26*, 5480.
- [107] L. Zhang, X. Shan, P. Bass, Y. Tong, T. D. Rolin, C. W. Hill, J. C. Brewer, D. S. Tucker, Z. Y. Cheng, *Sci. Reports* **2016**, *6*, 1.
- [108] D. J. Bergman, Y. Imry, *Phys. Rev. Lett.* **1977**, *39*, 1222.
- [109] S. Bauer, S. Bauer-Gogonea, I. Graz, M. Kaltenbrunner, C. Keplinger, R. Schwödiauer, *Adv. Mater.* **2014**, *26*, 149.
- [110] S. Tu, Q. Jiang, X. Zhang, H. N. Alshareef, *ACS Nano* **2018**, *12*, 3369.
- [111] X. Yang, Y. Wang, X. Qing, *Sens. Actuators, A* **2019**, *299*, 111579.
- [112] C. Pecharrormán, J. S. Moya, *Adv. Mater.* **2000**, *12*, 294.
- [113] D. Sengupta, L. Lu, Y. Pei, A. G. P. Kottapalli, *Proc. - IEEE Annu. Int. Conf. Micro Electro Mech. Syst., 16th* **2022**, 341.
- [114] Q. Li, H. Liu, S. Zhang, D. Zhang, X. Liu, Y. He, L. Mi, J. Zhang, C. Liu, C. Shen, Z. Guo, *ACS Appl. Mater. Interfaces* **2019**, *11*, 21904.
- [115] M. K. Filippidou, E. Tegou, V. Tsouti, S. Chatzandroulis, *Microelectron. Eng.* **2015**, *142*, 7.
- [116] Y. Ma, N. Liu, L. Li, X. Hu, Z. Zou, J. Wang, S. Luo, Y. Gao, *Nat. Commun.* **2017**, *8*, 1207.
- [117] P. Sobolciak, A. Tanvir, K. K. Sadasivuni, I. Krupa, *Sensors* **2019**, *19*, 4589.
- [118] S. Li, Y. Zhang, Y. Wang, K. Xia, Z. Yin, H. Wang, M. Zhang, X. Liang, H. Lu, M. Zhu, H. Wang, X. Shen, Y. Zhang, *InfoMat* **2020**, *2*, 184.
- [119] M. H. G. Wichmann, S. T. Buschhorn, J. Gehrmann, K. Schulte, *Phys. Rev. B: Condens. Matter Mater. Phys.* **2009**, *80*, 245437.
- [120] J. Park, Y. Lee, J. Hong, Y. Lee, M. Ha, Y. Jung, H. Lim, S. Y. Kim, H. Ko, *ACS Nano* **2014**, *8*, 12020.
- [121] M. Ha, S. Lim, J. Park, D.-S. Um, Y. Lee, H. Ko, *Adv. Funct. Mater.* **2015**, *25*, 2841.
- [122] L. J. Lanticse, Y. Tanabe, K. Matsui, Y. Kaburagi, K. Suda, M. Hoteida, M. Endo, E. Yasuda, *Carbon* **2006**, *44*, 3078.
- [123] A. I. Oliva-Avilés, F. Avilés, V. Sosa, *Carbon* **2011**, *49*, 2989.
- [124] T. C. Theodosiou, D. A. Saravanos, *Compos. Sci. Technol.* **2010**, *70*, 1312.
- [125] R. Rizvi, B. Cochrane, E. Biddiss, H. Naguib, *Smart Mater. Struct.* **2011**, *20*, 094003.
- [126] C. Yan, J. Wang, W. Kang, M. Cui, X. Wang, C. Y. Foo, K. J. Chee, P. S. Lee, *Adv. Mater.* **2014**, *26*, 2022.
- [127] C. S. Boland, U. Khan, C. Backes, A. O'Neill, J. Mccauley, S. Duane, R. Shanker, Y. Liu, I. Jurewicz, A. B. Dalton, J. N. Coleman, *ACS Nano* **2014**, *8*, 8819.
- [128] Y. Wang, L. Wang, T. Yang, X. Li, X. Zang, M. Zhu, K. Wang, D. Wu, H. Zhu, *Adv. Funct. Mater.* **2014**, *24*, 4666.
- [129] D. Niu, W. Jiang, G. Ye, K. Wang, L. Yin, Y. Shi, B. Chen, F. Luo, H. Liu, *Mater. Res. Bull.* **2018**, *102*, 92.
- [130] P. Costa, S. Gonçalves, H. Mora, S. A. C. Carabineiro, J. C. Viana, S. Lanceros-Mendez, *ACS Appl. Mater. Interfaces* **2019**, *11*, 46286.
- [131] D. Sengupta, V. Muthuram, A. G. Prakash Kottapalli, in *2020 IEEE Sensors, IEEE, Piscataway, NJ* **2020**, pp. 1–4.
- [132] C.-W. Nan, Y. Shen, J. Ma, *Annu. Rev. Mater. Res.* **2010**, *40*, 131.
- [133] B. F. Gonçalves, P. Costa, J. Oliveira, S. Ribeiro, V. Correia, G. Botelho, S. Lanceros-Mendez, *J. Polym. Sci., Part B: Polym. Phys.* **2016**, *54*, 2092.
- [134] C. Pailler-Mattei, S. Bec, H. Zahouani, *Med. Eng. Phys.* **2008**, *30*, 599.
- [135] R. Akhtar, M. J. Sherratt, J. K. Cruickshank, B. Derby, *Mater. Today* **2011**, *14*, 96.
- [136] Y. Zhang, M. Gong, P. Wan, *Matter* **2021**, *4*, 2655.
- [137] S. A. Fraser, W. E. Van Zyl, *Macromol. Mater. Eng.* **2022**, *307*, 2100973.
- [138] J. Zhang, L. Wan, Y. Gao, X. Fang, T. Lu, L. Pan, F. Xuan, *Adv. Electron. Mater.* **2019**, *5*, 1900285.
- [139] Y. Cai, J. Shen, C.-W. Yang, Y. Wan, H.-L. Tang, A. A. Aljarb, C. Chen, J.-H. Fu, X. Wei, K.-W. Huang, Y. Han, S. J. Jonas, X. Dong, V. Tung, *Sci. Adv.* **2020**, *6*, 5367.
- [140] X. Li, L. He, Y. Li, M. Chao, M. Li, P. Wan, L. Zhang, *ACS Nano* **2021**, *15*, 7765.
- [141] C. Zheng, Y. Yue, L. Gan, X. Xu, C. Mei, J. Han, *Nanomaterials* **2019**, *9*, 937.

- [142] M. Song, H. Yu, J. Zhu, Z. Ouyang, S. Y. H. Abdalkarim, K. C. Tam, Y. Li, *Chem. Eng. J.* **2020**, 398, 125547.
- [143] L. S. Liu, J. Kost, F. Yan, R. C. Spiro, *Polymers* **2012**, 4, 997.
- [144] S. Butylina, S. Geng, K. Laatikainen, K. Oksman, *Front. Chem.* **2020**, 8, 523441.
- [145] X. Yao, S. Zhang, L. Qian, N. Wei, V. Nica, S. Coseri, F. Han, *Adv. Funct. Mater.* **2022**, 32, 2204565.
- [146] S. Chen, Y. Dong, S. Ma, J. Ren, X. Yang, Y. Wang, S. Lü, *ACS Appl. Mater. Interfaces* **2021**, 13, 13629.
- [147] K. H. Lee, Y.-Z. Zhang, H. Kim, Y. Lei, S. Hong, S. Wustoni, A. Hama, S. Inal, H. N. Alshareef, *Small Methods* **2021**, 5, 2100819.
- [148] A. Rafeeerad, G. L. Sequiera, W. Yan, P. Kaur, A. Amiri, S. Dhingra, *J. Mech. Behav. Biomed. Mater.* **2020**, 101, 103440.
- [149] D. N. H. Tran, S. Kabiri, T. R. Sim, D. Losic, *Environ. Sci.* **2015**, 1, 298.
- [150] H. Liu, M. Dong, W. Huang, J. Gao, K. Dai, J. Guo, G. Zheng, C. Liu, C. Shen, Z. Guo, *J. Mater. Chem. C* **2017**, 5, 73.
- [151] Y. Ma, Y. Yue, H. Zhang, F. Cheng, W. Zhao, J. Rao, S. Luo, J. Wang, X. Jiang, Z. Liu, N. Liu, Y. Gao, *ACS Nano* **2018**, 12, 3209.
- [152] H. Yao, J. Ge, C. Wang, X. Wang, W. Hu, Z. Zheng, *Adv. Mater.* **2013**, 25, 6692.
- [153] X. Wu, Y. Han, X. Zhang, Z. Zhou, C. Lu, *Adv. Funct. Mater.* **2016**, 26, 6246.
- [154] Y. Qin, Q. Peng, Y. Ding, Z. Lin, C. Wang, Y. Li, F. Xu, J. Li, Y. Yuan, X. He, Y. Li, *ACS Nano* **2015**, 9, 8933.
- [155] A. M. Kamat, A. G. P. Kottapalli, in *2021 21st Int. Conf. on Solid-State Sensors, Actuators and Microsystems (Transducers)*, IEEE, Piscataway, NJ **2021**, pp. 888–891.
- [156] S. Wang, L. Lin, Z. L. Wang, *Nano Lett.* **2012**, 12, 6339.
- [157] Y. Yang, L. Lin, Y. Zhang, Q. Jing, T.-C. Hou, Z. L. Wang, *ACS Nano* **2012**, 6, 10378.
- [158] M. Ma, Z. Kang, Q. Liao, Q. Zhang, F. Gao, X. Zhao, Z. Zhang, Y. Zhang, *Nano Res.* **2018**, 11, 2951.
- [159] J. Luo, W. Gao, Z. L. Wang, *Adv. Mater.* **2021**, 33, 2004178.
- [160] H.-J. Yoon, H. Ryu, S.-W. Kim, *Nano Energy* **2018**, 51, 270.
- [161] F. Yi, L. Lin, S. Niu, P. K. Yang, Z. Wang, J. Chen, Y. Zhou, Y. Zi, J. Wang, Q. Liao, Y. Zhang, Z. L. Wang, *Adv. Funct. Mater.* **2015**, 25, 3688.
- [162] Z. Zhao, X. Pu, C. Du, L. Li, C. Jiang, W. Hu, Z. L. Wang, *ACS Nano* **2016**, 10, 1780.
- [163] J. Xiong, H. Luo, D. Gao, X. Zhou, P. Cui, G. Thangavel, K. Parida, P. S. Lee, *Nano Energy* **2019**, 61, 584.
- [164] Y. Yang, B. Xu, Y. Gao, M. Li, *ACS Appl. Mater. Interfaces* **2021**, 13, 49927.
- [165] S. Choi, K. Yoon, S. Lee, H. J. Lee, J. Lee, D. W. Kim, M.-S. Kim, T. Lee, C. Pang, *Adv. Funct. Mater.* **2019**, 29, 1905808.
- [166] L. Yan, Y. Mi, Y. Lu, Q. Qin, X. Wang, J. Meng, F. Liu, N. Wang, X. Cao, *Nano Energy* **2022**, 96, 107135.
- [167] R. Xu, F. Luo, Z. Zhu, M. Li, B. Chen, *ACS Appl. Electron. Mater.* **2022**, 4, 4051.
- [168] Y. Yang, L. Chen, J. He, X. Hou, X. Qiao, J. Xiong, X. Chou, *Adv. Mater. Technol.* **2022**, 7, 1.
- [169] W. Li, Y. Pei, C. Zhang, A. G. P. Kottapalli, *Nano Energy* **2021**, 84, 105865.



Debarun Sengupta is working as a postdoctoral researcher with the University of Groningen where he is involved with a Dutch Research Council (NWO) funded project titled “(SMART-AGENTS)” (<https://www.nwo.nl/en/projects/18024>). He also teaches an undergraduate course titled Nanoscience and Nanotechnology and a postgraduate course titled MEMS, NEMS, and Nanofabrication. He holds a Ph.D. in NEMS from the University of Groningen and an MEngSc in Electrical Engineering from UNSW, Sydney. Dr. Sengupta combines biomimetics engineering with state-of-the-art micro/nanofabrication techniques to create sophisticated sensors targeted for human physiological monitoring and flow sensing applications.



Ajay Giri Prakash Kottapalli is currently an Associate Professor and Chair of the Department of Bioinspired MEMS and Biomedical Devices (BMBD) at the Engineering and Technology Institute Groningen (ENTEG) at the University of Groningen (UOG). Since 2018, he is also a Research Affiliate with MIT Sea Grant at Massachusetts Institute of Technology. His core research focus is on Biomimetic materials, bioinspired MEMS/NEMS sensors, wearable electronics and biomedical devices. One of the key pursuits of his research is to optimally translate the biological sensory functions found in nature into biomimetic electronic sensors for healthcare applications.